Constraints on Dark Matter Annihilation from H.E.S.S. Observations of the Galactic Centre Region

Master's Thesis in Physics

submitted by
Katrin Streil
October 20, 2020

Erlangen Centre for Astroparticle Physics
Physikalisches Institut II
Friedrich-Alexander-Universität Erlangen-Nürnberg

Supervisor: Prof. Dr. Christopher van Eldik
Second referee: Prof. Dr. Stefan Funk

Abstract

Dark matter is expected to self-annihilate into standard model particle pairs. The γ-rays emitted during this process can be detected with ground-based γ-ray telescopes like H.E.S.S. allowing an indirect dark matter search. The exact dark matter density distribution is unknown but suggested to peak at the Galactic Centre making this region in particular interesting for the search of the faint dark matter γ-ray flux. However, there are many γ-ray emitting sources in the Galactic Centre region like the central HESS J1745-290 and the diffuse emission. To avoid any misinterpretation of an excess as a dark matter signal, the region along the Galactic Plane typically is excluded from the region of interest leading to a reduced expected dark matter γ-ray flux. With the three-dimensional analysis method used in this work, the exclusion is avoided by accounting for the excess of the γ-ray emitting sources in the dark matter search. Hence, a good understanding and model of the Galactic Centre region is crucial for this approach. The upper limits on the self-annihilation cross-section presented in this work are unexpectedly low compared to results from other H.E.S.S. publications. Insufficient descriptions of the Galactic Centre region and not yet understood systematics are possible reasons for the deviations. The sensitivity study of the H.E.S.S. observations of the Galactic Centre region in three dimensions was successful and in good agreement with H.E.S.S. publications since it is free from the systematics affecting the dark matter constraints.

Zusammenfassung

Zwei dunkle Materie Teilchen können in ein Teilchen-paar aus dem Standard Modell annihilieren. Durch die dabei emittierte Gammastrahlung lässt sich die dunkle Materie indirekt mit erdgebundenen Gammastrahlungsteleskopen wie H.E.S.S. nachweisen. Obwohl die exakte Dichteverteilung dunkler Materie nicht bekannt ist, wird in den gängigen Theorien davon ausgegangen, dass sie im Galaktischen Zentrum am größten ist. Das macht das galaktische Zentrum zu einer geeigneten Region für die indirekte Suche nach dunkler Materie. Allerdings befinden sich im Galaktischen Zentrum zahlreiche stark emittierende Gammastrahlungsquellen, wie die diffuse Emissionen oder die zentral gelegene Quelle HESS J1745-290. Damit keiner dieser Emissionen als dunkle Materie interpretiert wird, schneidet man typischerweise die gesamte Region entlang der Galaktischen Ebene aus der zu analysierenden Region heraus. Das hat einen reduzierten Gammastrahlungsfluß aufgrund von dunkler Materie-Annihilation zur Folge. In der dreidimensionalen Analyse-Methode, die in der vorliegenden Master-Arbeit angewandt wird, ist keine Exklusion nötig, da die Emissionen der Gammastrahlungsquellen berücksichtigt werden. Das setzt allerdings ein gutes Verständnis und ein sehr akkurates Modell der Region voraus. Die berechneten oberen Limits für den Wirkungsquerschnitt der Annihilation sind deutlich niedriger als vergleichbare Werte aus anderen H.E.S.S.-Publikationen. Grund dafür ist eine unzureichend genaue Beschreibung der Region des Galaktischen Zentrums und nicht verstandene Systematiken. Die hier in drei Dimensionen berechnete Sensitivität bezüglich dunkler Materie von H.E.S.S. liegt in der erwarteten Größenordnung, da diese nicht von den Systematiken verfälscht wird.

Contents

Chapter 1

Introduction

The history, size and composition of the universe have been studied by astronomers, cosmologists, and physicists for centuries. Within the last decades a standard model of the big bang cosmology emerged, the Λ-CDM model (Lambda cold dark matter). It is the simplest model in good agreement with the observed properties of the cosmos like the existence of the cosmic microwave background, the abundance of certain elements, the large-scale structures and the accelerating expansion of the universe. In the model, the universe consists in addition to normal matter of dark energy associated with Λ, the cosmological constant, and the postulated cold (non-relativistic) dark matter (DM). Dark energy is responsible for the observed acceleration in the Hubble expansion against the attractive effects of gravity. Cold dark matter is used to explain the observed gravity ordinary matter can not account for on its own. Since it is expected to annihilate into standard model particle pairs it can be detected indirectly through γ-rays emitted during the decay. A common region of interest for these studies is the Galactic Centre region where the faint signal is expected to be relatively high. Usually, the regions with strong γ-ray emitting sources along the Galactic Plane are excluded from the field of view (FoV) such that no signal gets mistakenly interpreted as DM. However, in this work, a different approach to the indirect DM search was chosen for the first time. The γ-ray emitting sources were kept in the FoV and their excess were accounted for in the fit by modelling both their morphology and spectrum. Thereby, a significant part of the expected γ-rays due to DM annihilation is taken into account resulting in stronger constraints on the cross-section.

Dark matter is discussed in more detail in the first part of this thesis. The focus is on the evidence and candidates for DM, followed by the current state of the search for one group of DM candidates, in particular, the weakly interacting massive particles (WIMPs). The γ-ray data used in this work was taken by H.E.S.S., a system of ground-based γ-ray telescopes. Its working principle, technicalities and data taking will be discussed in Chapter 3. Afterwards, the data analysis methods are explained. This includes the three-dimensional maximum likelihood fitting and the likelihood ratio test used to compute upper limits on the DM annihilation cross-section. Crucial for this analysis is a good model of the Galactic Centre region to allow the search for DM without excluding any regions from the FoV. In Chapter 5, the different components of this model are briefly discussed followed by a fit to the H.E.S.S. data and an evaluation of the quality of the fit. After a sufficient description of

the Galactic Centre is ensured the DM analysis is performed. In Chapter 6, the DM model component is explained. Afterwards, both the computed sensitivity and the DM constraints are discussed and compared to published H.E.S.S. results. The DM constraints computed in this work show strong deviations from both the sensitivity and the H.E.S.S. results. Therefore, Chapter 7 focuses on the systematic uncertainties possibly causing them. This includes an 'injection and recovery' test, the exclusion of the regions with strong γ-ray emitting sources and an analysis with additional data. In Chapter 8, the sensitivity and DM constraints for different annihilation channels are presented followed by a conclusion and an outlook.

Chapter 2

Dark Matter

In the first part of the following chapter, the observations that are considered evidence for DM are briefly discussed. Afterwards, three candidates for DM are introduced. In this work, DM is considered to be one of these candidates, a weakly interacting massive particle (WIMP). Hence, the search for WIMP-like DM particles is discussed in detail including the current status of detection, their annihilation spectrum, the flux of the photons they emit and the spatial distribution.

2.1 Evidence for Dark Matter

Dark Matter got first mentioned in a paper by Fritz Zwicky published in 1933 [1]. He analyzed the movement of eight galaxies of the Coma Cluster along their gravitational orbits using the Viral theorem and redshift. Normal matter could not account for the measured velocities, resulting in him proposing the existence of a non-shining, DM.
This section gives an overview of three evidences for DM on different scales, but all based on the same argument Zwicky used: One needs DM to explain the observed gravitation. The chapter is based on [2].

2.1.1 Rotation Curves of Galaxies

On a galactic scale, rotation curves are considered direct evidence for DM. Rotation curves are the measurement of the circular velocities of stars and gas as a function of their radial distance to the Galactic Centre. For smaller distances, this is done with optical surface photometry, while for larger distances one observes the 21 cm hydrogen line. In Newtonian dynamics the velocity is expected to be $v(r) \propto 1/\sqrt{r}$. However, at larger distances from the Galactic Centre the rotation curve was found to be flat (Figure 2.1). This implies that the mass within a certain radius r is proportional to this radius $M(r) \propto r$ and therefore $\rho \propto 1/r^2$. This condition is not fulfilled by visible matter but can be explained by the existence of DM.
By observing rotation curves one can determine the density of DM at the sun's distance, the local density $\rho_\odot$. For the calculation, the density distribution of the galactic bulge and disk is needed, since rotation curves only measure the total mass within a certain orbit. The local density has a rather large uncertainty and different groups found different values in the range of about $0.2 - 0.8\,\mathrm{GeV/cm^3}$ [2]. The DM distribution will be discussed more in detail in Section 2.3.4.

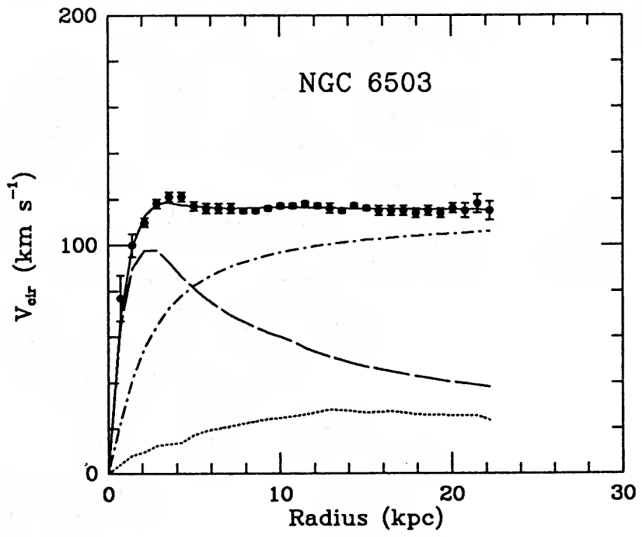

Figure 2.1: Rotation curve fit (solid line) of the dwarf spiral galaxy NGC 6503. Also shown are the individual components: the dashed curve is for the visible component, the dotted curves for the gas and the dash-dot curves for the dark halo. Figure taken from [3].

2.1.2 Gravitational Lensing

On an even larger scale, evidence for DM can be found via gravitational lensing. Hereby, the appearance of an object like a star or a galaxy gets deformed by another massive object within the line of sight to the observer. As predicted by Einstein's general theory of relativity, the light gets bent by the gravity of the object in the foreground. This results in a distorted image. If the two objects align and the mass of the closer object is large enough, one observes a so-called Einstein Ring (Figure 2.2).
Weak gravitational lensing was used to prove the existence of DM in the bullet cluster 1E 0657-558, a collision of two galaxies [5]. In this cluster, the stellar components and the plasma are spatially separated, since only the latter was affected by the collision. They found by creating gravitational lensing maps, that the gravitational potential approximately traces the distribution of the galaxies and not the plasma distribution containing the dominant baryonic mass (Figure 2.3). The gravitational force can not be explained by the plasma distribution alone but only by the existence of an unseen matter in the system. Since this matter was not affected by the collision it is expected to only interact weakly (apart from gravitation).

2.1.3 Cosmological Evidence

The total amount of DM in the universe can only be estimated on a cosmological scale by an analysis of the cosmic microwave background (CMB). It is relic radiation from the early universe when photons were no longer scattered at a plasma of protons and electrons but were able to propagate freely. This is known as decoupling. The CMB is isotropic at the 10^{-5} level and has a thermal black body spectrum at temperature $T = 2.726\,\mathrm{K}$. The small anisotropies in the temperature correspond to fluctuations of the matter density in the early Universe. By analyzing the power

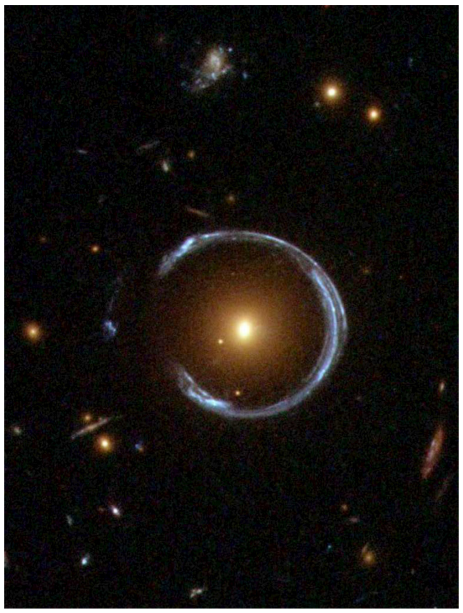

Figure 2.2: Image of LRG 3-757 taken by the Hubble Space Telescope. The blue galaxy gets gravitationally lensed by the yellow one and appears as an almost closed Einstein Ring. Image Credit: ESA/Hubble & NASA [4]

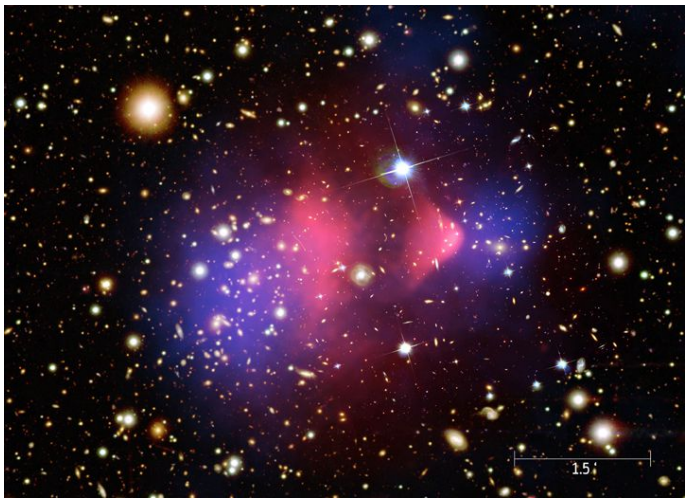

Figure 2.3: Chandra image of the bullet cluster. In pink the X-ray emitting plasma taken by the Chandra X-ray Observatory, in blue the gravitational potential calculated from lensing and the optical components taken by the Magellan telescope and the Hubble space telescope. Image Credit: X-ray: NASA/CXC/CfA/M.Markevitch et al.; Optical: NASA/STScI; Magellan/U.Arizona/D.Clowe et al.; Lensing Map: NASA/STScI; ESO WFI; Magellan/U.Arizona/D.Clowe et al.

spectrum of the anisotropy of the CMB, cosmological models can be tested. The standard cosmological model is the Lambda Cold DM (ΛCDM) model, which describes the evolution of the universe since the big bang with a few parameters. From these independent cosmological parameters, the DM density parameter $\Omega_{DM} = 0.25$ can be calculated. A quarter of the total energy density is therefore non-baryonic, cold (non-relativistic) DM.

2.2 Dark Matter Candidates

The following section is based on [6].
Generally one expects the DM particle to have three characteristics:

- non-baryonic:
  interactions with the W and Z gauge bosons, but not with gluons or photons and thus not carrying electric or colour charges.

- stable:
  or at least extremely long-lived, that means having a lifetime substantially greater than the age of the Universe.

- non-relativistic (and therefore massive):
  relativistic (massless) particles could not produce the gravitational potential that is necessary for the observed structure formation. This rules out neutrinos the only standard model particle candidate to have the other two characteristics.

In the following, three possible candidates for DM are introduced. The first one, the Modified Newtonian Dynamics, is not a candidate per se but instead explains the observed rotation curves. The other two, axions and WIMPs, are well motivated by particle physics problems and considered as possible DM candidates.

2.2.1 Modified Newtonian Dynamics

Instead of explaining discrepancies in the observed rotation curves with additional DM, a modification of Newtonian dynamics (MOND) has been proposed in the last decades. The known Newtonian Law does no longer apply for accelerations below a certain threshold, the acceleration constant $a_0 \approx 10^{-10}\mathrm{m/s^2}$, which is the typical centripetal acceleration of a star in a galaxy. The transition from Newtonian Dynamics to MOND is not detectable within the solar system since even the acceleration of Mercury on Pluto is above a_0 [7]. But MOND provides good fits to the asymptotic flatness of the rotation curves of galaxies (Figure 2.1). MOND has problems describing the dynamic of Galaxy clusters and the structure of the CMB [8].

2.2.2 Axions

Axions are hypothetical particles motivated by a problem called the CP-violation. It is the breaking of the symmetry with respect to the combined charge conjugation and parity. In the electroweak theory, the CP-violation was experimentally observed,

however not for strong interactions. To explain the experimental results a term in the Lagrangian of the quantum chromodynamics has to take a value which deviates from the theoretical assumptions by a few orders of magnitudes. Since the standard model can explain the strong CP-violation but only for a seemingly unnatural choice of a parameter it is called a fine-tuning problem.
In the case of a spontaneous symmetry breaking, this problematic parameter would vanish. The consequence of this new symmetry is the axion. The light, electric neutral, and weakly interacting particle is considered as a candidate for DM.
Currently, multiple experiments aiming to set limits on the parameter space of axions, or more generic axion-like particles, are emerging. In the case of existence, a positive detection is expected in the near future due to sufficient sensitivity of the future detection methods [9].

2.2.3 WIMPs

A broad class of particles considered theoretical candidates for DM are the weakly interacting massive particles (WIMPs). Their mass is in the range between a few GeV and some 100 TeV.

Thermal Freeze-Out

WIMPs are thought to be produced through the thermal freeze-out: In the early, hot, and dense Universe all particles are in thermal equilibrium. But DM particles with the mass m_x get Boltzmann-suppressed if the cooling Universe reaches a Temperature $T < m_x$. The number of DM particles drops exponentially as $e^{-m_x/T}$ and eventually reaches zero. However, the Universe is expanding which decreases the probability of two DM particles to annihilate. Instead of dropping, their number asymptotically approaches a constant, the relic abundance. This is called the chemical 'freeze-out'. Note that interactions mediating energy exchanges between the DM particles and other particles still occur but the decrease in the number of DM particles is negligible. For the WIMPs to approach the relic abundance a certain self-annihilation cross-section is required, the thermal relic cross-section $\langle \sigma v \rangle_{\text{thermal relic}} = 3 \cdot 10^{-26} \text{cm}^3/\text{s}$.

Candidates

Several theories provide possible WIMP candidates. The most discussed ones are the theory of supersymmetry (predicting the neutralino) and the Kaluza-Klein (KK) theory of an extra dimension (predicting axions). The two theories are shortly explained in the following.

Supersymmetry was introduced to solve the gauge hierarchy problem. It is the question of why the electroweak force is 10^{24} times stronger than gravity. Since the Higgs mechanism describes how the exchange particles obtain their masses through interactions with the Higgs field the gauge hierarchy problem breaks down to the question: Why is the physical Higgs boson mass $m_b \approx 125\,\text{GeV}$ so much smaller than the Planck mass $M_{Pl} = 1.2 \cdot 10^{19}$ GeV?

Usually, all masses are affected by quantum radiative corrections. Symmetries protect both fermions and gauge bosons from these corrections but not the Higgs boson. This is due to the Higgs field being scalar (spin = 0). The corrections come from self-interactions, gauge boson loops, and fermion loops. The latter two have contributions to the Higgs mass with opposite signs. Due to this fact, supersymmetry can solve the gauge hierarchy problem. If the number of fermionic and bosonic degrees of freedom were to be the same the contributions to the Higgs mass would be cancelled. In supersymmetry that is the case since every particle in one group has an associated partner in the other group. The spin of two superpartners differs by a half-integer. Electrically neutral particles predicted by supersymmetry can be considered as DM candidates. These are the Gravitino $\tilde{G}$, the Sneutrinos, $\tilde{\mu_e}$, $\tilde{\mu_\mu}$ and $\tilde{\mu_\tau}$, and four neutralinos, χ_1, χ_2, χ_3 and χ_4. The latter are eigenstates mixed by four neutral spin $1/2$ fermions. The lightest of these, χ_1, is a WIMP DM candidate since it is stable. The neutralino does not carry a colour charge and its predicted cross-section is in the right order of magnitude. That solving the gauge hierarchy problem with supersymmetry results in a WIMP DM candidate is called the 'WIMP miracle'.

Another extension of the standard model (SM) predicting a WIMP is the Kaluza-Klein (KK) theory. It proposes an additional space-like dimension to the four known dimensions of space-time. This fifth dimension is curled up and could take the form of a very small circle with radius R. Each SM particle has a partner particle at every one of the infinite KK levels. The mass of a partner particle at level n is $\propto nR^{-1}$. The lightest KK particle is the B^1, the partner of the hypercharge gauge boson at the first level, which is stable due to the conservation of the KK-parity. For the B^1 to have the correct thermal relic density, its mass must be approximately 1 TeV making it a WIMP DM candidate.

This short introduction on WIMPs as a DM candidate is followed by a more detailed discussion about the search for WIMP-like particles in the following section.

2.3 The Search for WIMP-like Dark Matter Particles

The first part of this section is about the current status of the search for WIMPs with three different detection methods. Since the DM flux has to be estimated for the detection the two necessary components for this calculation, the spatial distribution and the spectrum, will be discussed in the following part.

2.3.1 Current Status of the Detection

The annihilation of two WIMPs $\chi\,\chi$ into two other particles introduces three strategies for their detection. Here it is assumed, that the produced particles are known standard model particles.

- Particle colliders:
  If DM were to be produced through $\mathrm{SM\,SM} \rightarrow \chi\,\chi$ they would not be detectable. But signatures of DM could be detected through related production mechanisms, such as $\mathrm{SM\,SM} \rightarrow \chi\,\chi + \{\mathrm{SM}\}$.

- Direct detection:
  The transferred energy of scattering between a normal particle off a DM particle through $\chi\,\mathrm{SM} \rightarrow \chi\,\mathrm{SM}$ could be observed in sensitive detectors.

- Indirect detection:
  If two DM particles annihilate today through $\chi\,\chi \rightarrow \mathrm{SM\,SM}$ the products could be detected. The annihilation spectrum of WIMPs is discussed in detail in Section 2.3.2.

The current status of these three detection methods of WIMPs will be discussed briefly in the following.

Production of WIMPs with Particle Colliders

At the Large Hadron Collider (LHC), WIMPs can be produced indirectly and escape the detector. The existence of undetectable particles takes place through the signature of missing energy and momentum. But even though the missing particles are consistent with DM it is not compelling evidence. A particle leaving the detector implies a lifetime $\tau > 10^{-7}\,\mathrm{s}$, which is not even close to the required $\tau > 10^{17}\,\mathrm{s}$ for DM [6]. Since colliders can determine the thermal relic density of the missing particle due to strong constraints on its properties consistency with the cosmologically observed density would be strong evidence for the particle to be DM.

Direct Detection

Direct detection experiments aim to detect the nuclear recoil in the scattering of a nuclear DM particle off target nuclei. The recoil energy is converted into thermal motion (phonons), ionization, or scintillation photons depending on the detector material. The scattering rate depends on astrophysical inputs (local density and velocity distribution of WIMPs), the WIMP mass, and the interaction cross-section of the target nuclei which is predicted to be in the order of $10^{-24}\,\mathrm{cm}^2$ [10]. The resulting extremely low signal rate requires an extraordinarily low background environment. This is obtained by passive shielding, active veto, high-purity detector components, and a location deep underground. However, the irreducible background coming from solar and atmospheric neutrinos limits the sensitivity of direct detection experiments. It is usually assumed that the scattering is coherent and elastic and that the interaction does not depend on the nuclear spin to allow comparison of the results from different experiments. The current constraints on the interaction cross-section for different WIMP masses are shown in Figure 2.4.

Indirect Detection

Even though DM pair annihilation becomes suppressed after the chemical freeze-out it still occurs and may be detectable indirectly via their annihilation products. Neutrinos being one of these annihilation products makes neutrino observatories like IceCube or ANTARES indirect DM detectors. Since the annihilation rate is very small one focuses on regions where a higher DM density is expected. In the case of neutrinos, this is, for instance,g the Earth's centre where they are captured due to scattering. Note that the indirect detection via neutrinos sets limits on the scattering cross-section and not the annihilation cross-section since only the capture rate

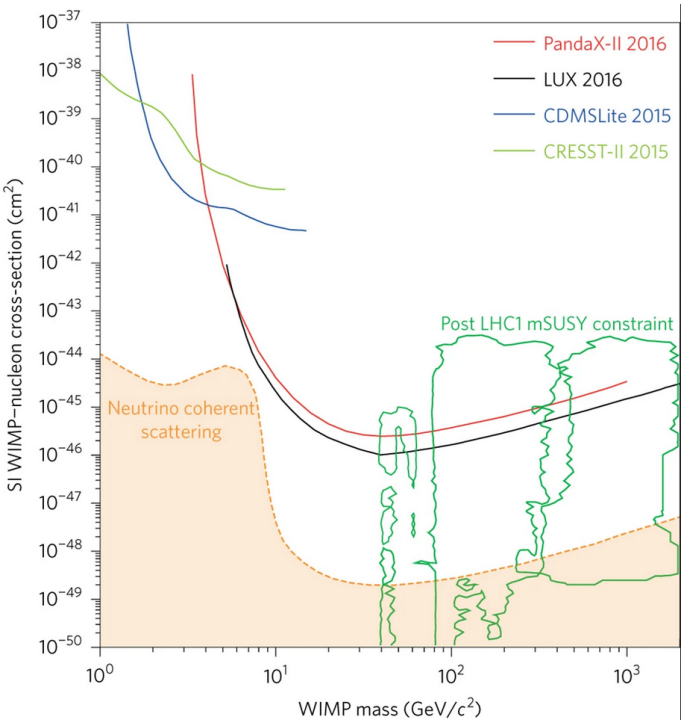

Figure 2.4: Upper limits on the WIMP-nucleon scattering cross-section (spin-independent) set by current leading experiments and the neutrino scattering background curve [10].

determines the neutrino signal rate. This makes a comparison with the results of the direct detection methods possible.

Another way of detecting the annihilation products is with the use of γ-ray satellites or ground-based γ-ray Cherenkov telescopes. One distinguishes between 'prompt' γ-ray emission due to an annihilation of the DM into two photons (or γZ_0) and secondary γ-ray emission where the γ-rays are the decay product of charged particles created by the annihilation. The first results in a line-like signal in the energy spectrum while the latter has a broad spectrum with a cutoff at the DM particle mass m_{DM}. One also preeminently searches in regions where the DM density is expected to be higher. This is the case for cores of dwarf galaxies, galaxy clusters, and the Galactic Centre and Halo. Since the flux decreases proportionally to the squared increasing distance it is beneficial to concentrate on close-by objects. A strong astrophysical γ-ray background complicates the DM search which therefore either has to be understood very well or cut out off the region of interest.
Note that it is in principle also possible to detect the products of DM particle decays but the decay rate is linear to the DM density instead of proportional to the square of the DM density like it is the case for the annihilation rate.

Figure 2.5 shows the upper limit on the annihilation cross-section of DM in the case of prompt γ-ray emission from H.E.S.S. and Fermi-Lat. The region of interest was the Galactic Centre.
The constraints on the cross-section of the annihilation of DM particles into W^+W^- from different telescopes and regions of interests (Galactic Centre and dwarf galaxies) are plotted in Figure 2.6. The constraints obtained by ground-based telescopes are

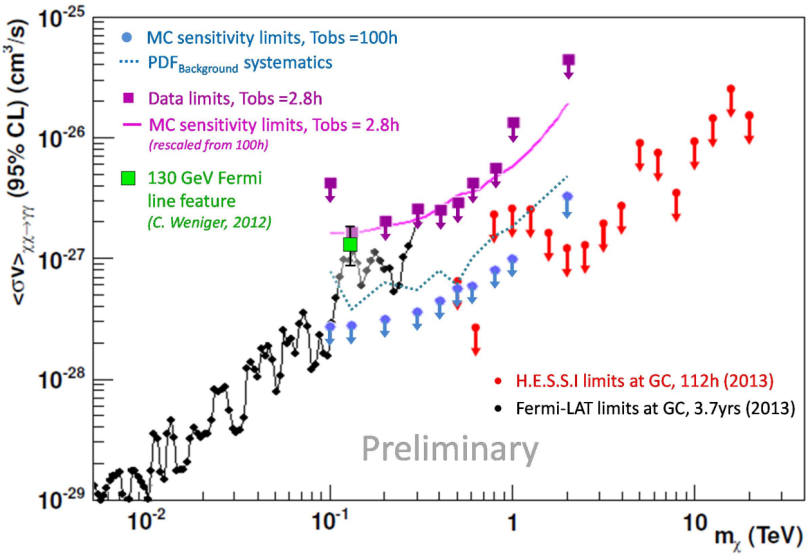

Figure 2.5: Upper limits on the annihilation cross-section of DM into $\gamma\gamma$ (prompt emission), from Fermi (black points) and HESS (red and purple points) [11].

stronger if the Galactic Halo is analysed compared to dwarf galaxies. The best limits are provided by the Fermi satellite for $m_{\mathrm{DM}} < 0.5\,\mathrm{TeV}$.

2.3.2 Annihilation Spectrum of WIMPs

The energy spectrum of the γ-rays depends on the channel in which the DM particles annihilate. Several channels are possible: leptons, either left or right-handed (i.e. e_L^+ e_L^-), a light or a heavy quark (i.e. $\bar{b}b$), standard model Higgs boson, neutrinos, photons, gluons, Z and W bosons, or an annihilation into a new boson V which later decays into a pair of leptons.
The fluxes of these particles at the production point ('primary fluxes') can be obtained with Monte Carlo simulation programs. In this analysis, the primary fluxes from [13] were used. Figure 2.7 shows the primary spectrum for $m_{\mathrm{DM}} = 10$ TeV and for all the available channels with the x-axis normalised to m_{DM}. The prompt annihilation into two γ-ray pairs has the mentioned peak at m_{DM} while the spectra of the other channels have a cutoff at m_{DM} since there can not be an annihilation product with a higher energy than the original particle. The primary fluxes are electroweak corrected and DM model-independent, meaning that channels suppressed in many models (i.e. $\gamma\gamma$) are still included.

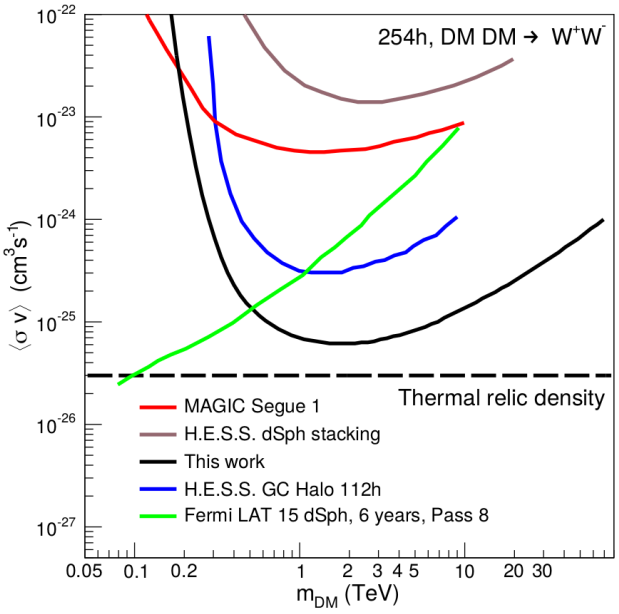

Figure 2.6: Comparison of constraints on the annihilation cross-sections in the W^+W^- channel from 112 and 254 hours of HESS data on the Galactic Halo (blue and black line, respectively), limits from observations of 15 dwarf galaxy satellites by the Fermi-LAT satellite (green line), limits form 157 hours of observation of the dwarf galaxy Segue 1 by MAGIC (red line) and combined analysis of observations of 4 dwarf galaxies by H.E.S.S. (brown line) [12].

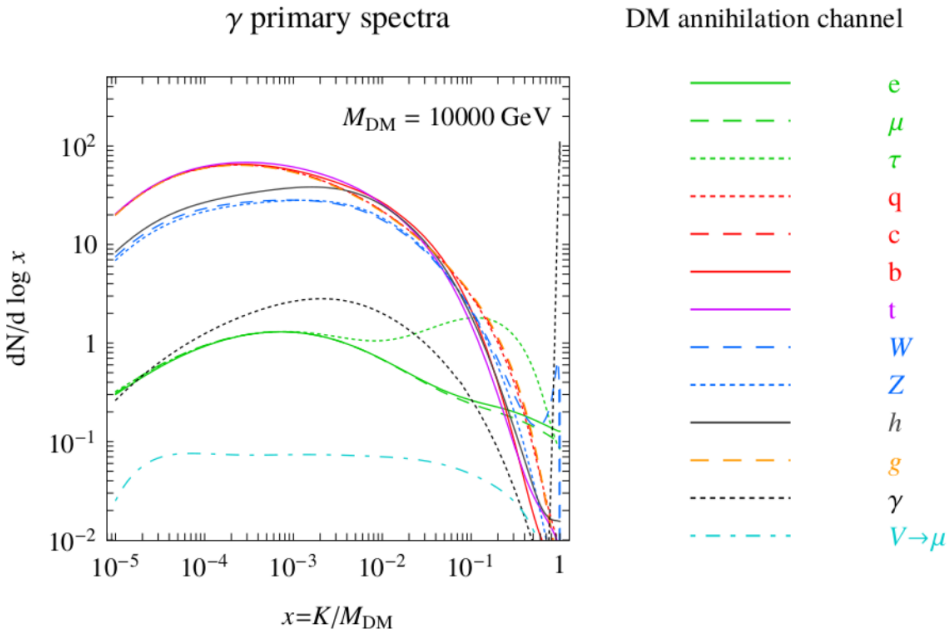

Figure 2.7: γ-ray spectrum from the pair annihilation of a DM particle with $m_{\mathrm{DM}} = 10\,\mathrm{TeV}$ in different channels [13]. The results are expressed in terms of the energy fraction $x = K/m_{\mathrm{DM}}$, where K is the kinetic energy of the final-state stable particle.

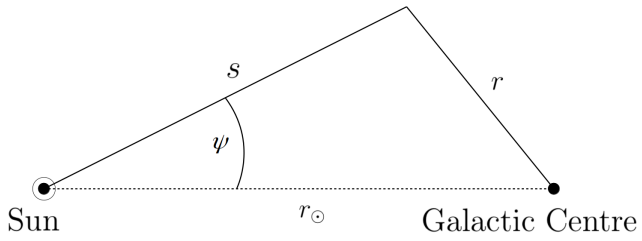

Figure 2.8: Representation of the coordinates s, r and ψ

2.3.3 Differential Flux of Emitted Photons

In order to detect DM indirectly with γ-ray telescopes the differential flux of the photons has to be calculated. For photons produced by DM annihilation this flux from a given angular direction $d\Omega$ is given by:

$$\frac{d\Phi_\gamma}{d\Omega dE} = \underbrace{\frac{1}{4\pi k m_{\mathrm{DM}}^2} \sum_f < \sigma v >_f \frac{dN_\gamma^f}{dE}}_{\text{particle physics}} \cdot \underbrace{\frac{dJ}{d\Omega}}_{\text{astrophysics}}, \tag{2.3.1}$$

where $\frac{dN_\gamma^f}{dE}$ is the energy spectrum of photons produced per one annihilation in the channel with the final state f (section 2.3.2). The value of k depends on the type of DM particle. For a Majorana particle it is $k = 2$ and for a Dirac particle $k = 4$. The astrophysical differential J-Factor $\frac{dJ}{d\Omega}$ is the integral along the line of sight of the squared DM density:

$$\frac{dJ}{d\Omega} = \int_{LOS} \rho^2(r(s,\psi))ds, \tag{2.3.2}$$

where ψ is the angle between the line of sight and the direction of the observation (Figure 2.8). The DM density ρ is discussed in Section 2.3.4. The integrated J-Factor is defined as:

$$J(\Delta\Omega) = \int_{\Delta\Omega} \frac{dJ}{d\Omega} d\Omega, \tag{2.3.3}$$

The parameter r can be expressed in terms of ψ, the line of sight s, and the distance between the sun and the Galactic Centre $r_\odot$:

$$r = \sqrt{r_\odot^2 + s^2 - 2 r_\odot s \cos(\psi)} \tag{2.3.4}$$

2.3.4 Dark Matter Distribution

To calculate the J-Factor, the DM distribution of a galaxy needs to be known. However, this distribution cannot be observed directly but is simulated leading to multiple possibilities. The models have the common assumption of a radial symmetric distribution. One of this models was introduced by Navarro, Frenk and White (NFW) which is based on cosmological N-body simulations [14]. It describes the distribution as a power law with an index of -1 at the Galactic Centre. Also motivated by more recent N-body simulations but not converging to a power law at

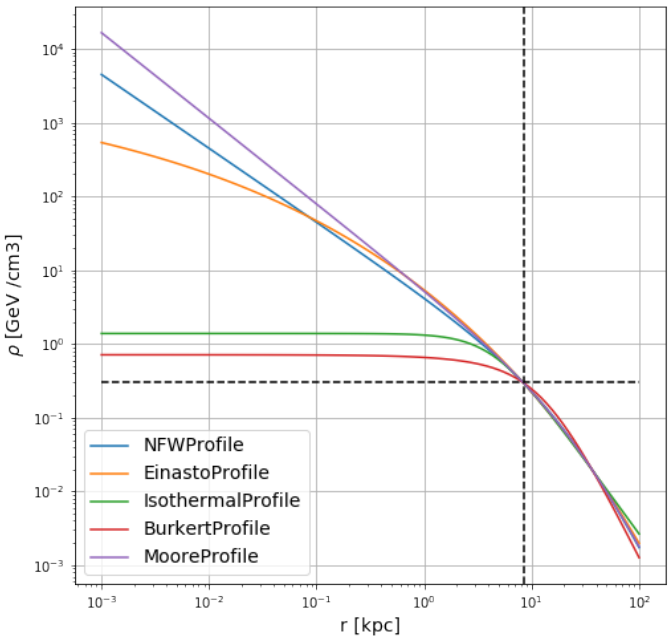

Figure 2.9: DM profiles scaled to the local DM density.

the Galactic Centre is the Einasto profile [15, 16]. Moore and collaborators have found a profile even steeper than the NFW profile [17]. All three of the profiles are referred to as Cusped profiles due to them predicting a rather high density at the centre. Including baryonic matter into the simulation results in so called Cored profiles which are defined by a constant density within the inner part. Commonly used are the isothermal profile [18] or the Burkert profile [19]. The profiles read as:

$$\begin{aligned}
\text{NFW}: \quad & \rho_{\text{NFW}}(r) &&= \rho_s \frac{r_s}{r}\left(1+\frac{r}{r_s}\right)^{-2} \\
\text{Einasto}: \quad & \rho_{\text{Ein}}(r) &&= \rho_s \exp\left\{-\frac{2}{\alpha}\left[\left(\frac{r}{r_s}\right)^{\alpha}-1\right]\right\} \\
\text{Moore}: \quad & \rho_{\text{Moo}}(r) &&= \rho_s \left(\frac{r_s}{r}\right)^{1.16}\left(1+\frac{r}{r_s}\right)^{-1.84} \\
\text{Isothermal}: \quad & \rho_{\text{Iso}}(r) &&= \frac{\rho_s}{1+(r/r_s)^2} \\
\text{Burkert}: \quad & \rho_{\text{Bur}}(r) &&= \frac{\rho_s}{(1+r/r_s)(1+(r/r_s)^2)}
\end{aligned} \tag{2.3.5}$$

The profiles are parameterised in terms of the typical scale radius r_s and the typical scale density ρ_s. The latter is chosen such that at the location of sun $r_\odot = 8.5\,\text{kpc}$ the DM density is $\rho_\odot = 0.39\,\text{GeV/cm}^3$. The typical scale radius for the NFW (Einasto) profile was set to 20.0 kpc (21.0 kpc). The shape parameter α of the Einasto profile is 0.17. All of these values are adapted from earlier H.E.S.S. publications to allow an easier comparison [12]. The five profiles are plotted in Figure 2.9 as a function of the distance to the Galactic Centre. In this plot r_s and ρ_s for the Isothermal, the Burkert and the Moore profile are adapted from [13].

Chapter 3

Ground-based γ-ray Telescopes and H.E.S.S.

γ-rays can be detected on the ground (ground-based telescopes) or out of the atmosphere (satellites like the Fermi-Lat). The latter is only possible for γ-ray energies up to 300 GeV since the small detector area can not compensate for the lower γ-ray flux at higher energies. Ground-based telescopes, on the other hand, are not as limited in their detection area and therefore can detect photons with energies up to approximately 100 TeV. Their detection method is indirect and is called Imaging Atmospheric Cherenkov Technique, which is discussed in the following section after a short introduction of air-shower development and Cherenkov light. Since this work's data is taken with H.E.S.S., it will be the focus of the second part of this chapter.

3.1 Air-shower Development

Earth's atmosphere is not transparent for cosmic rays. They interact with nuclei and induce air-showers, cascades of secondary particles. One differentiates between electromagnetic (induced by a lepton or a photon) and hadronic (induced by a hadron) air-showers. They can be distinguished due to different longitudinal and latitudinal depth, as well as the kind and amount of secondary particles since the two types of showers are based on different interactions.

Electromagnetic Air-showers

High energy electrons e^-, positrons e^+, and photons γ interact with the atmosphere via Bremsstrahlung or pair annihilation. The annihilation of two photons into a e^-e^+ pair can only occur in the presence of atmospheric nuclei so that energy and momentum are conserved. A Bremsstrahlung photon gets emitted due to the deceleration of a $e^\pm$ in the Coulomb field of an atomic nucleus. Both these processes alternate until the energy of the interacting particle falls below a certain threshold energy. For the Earth's atmosphere, this critical energy is approximately $E_c \approx 80\,\text{MeV}$. Once reached the dominant process is no longer Bremsstrahlung or pair annihilation but an energy loss due to ionization and the shower development ends. The process is sketched in Figure 3.1.
A commonly used model to describe electromagnetic air-showers is based on Heitler

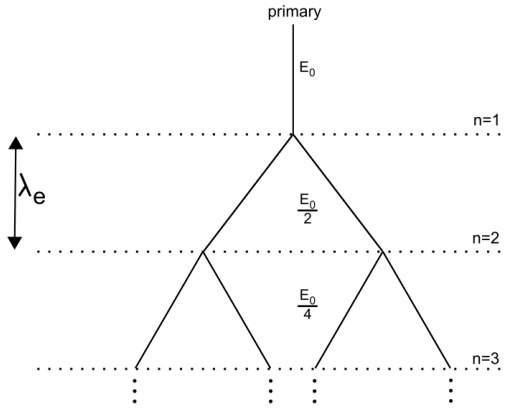

Figure 3.1: Basic scheme of an electromagnetic air shower. Figure taken from [21].

which describes the most important characteristics very well even though it is based on two simple assumptions [20]. Firstly, both photons and $e^{\pm}$ interact after travelling a distance λ and secondly, the interacting particles energy E_0 gets transferred to the two produced particles equally. After n interactions, the air-shower therefore consists of 2^n secondary particles and has a longitudinal length of

$$X = n\lambda \log(2) \tag{3.1.1}$$

The maximal amount of secondary particles is

$$N_{\max} = E_0/E_c, \tag{3.1.2}$$

which gets reached after $n_{\max} = \log(N_{\max})/\log(2)$ interactions. This results in a maximal longitudinal depth of

$$X_{\max} = \lambda \log(E_0/E_c) \tag{3.1.3}$$

Even though the model is rather simplistic two conclusions of Heitler were confirmed by simulations and observations: the maximal amount of secondary particles $N_{\max}$ is proportional to E_0 and the maximal longitudinal depth $X_{\max}$ is proportional to the logarithm of E_0 [21].

Hadronic Air-showers

In the case of a hadronic primary particle the dominant interaction is strong. Due to the inelastic scattering mostly pions (π^0, $\pi^{\pm}$) are produced (figure 3.2). Neutral pions π^0 decay into two photons resulting in an electromagnetic sub-shower, while charged pions continue to interact with the atmosphere. Thereby, a new generation of pions gets produced until the energy of the single pions falls below the critical energy E_c^{π}. In this case, a decay into myons and neutrinos is more likely:

$$\pi^+ \rightarrow \mu^+ + \nu_\mu \tag{3.1.4}$$

$$\pi^- \rightarrow \mu^- + \overline{\nu}_\mu.$$

Hadronic air-showers can be divided into three components: soft, electromagnetic component ($e^{\pm}$, γ), hadronic component (π^0, $\pi^{\pm}$), and a muonic component (myons are unlikely to interact with matter).

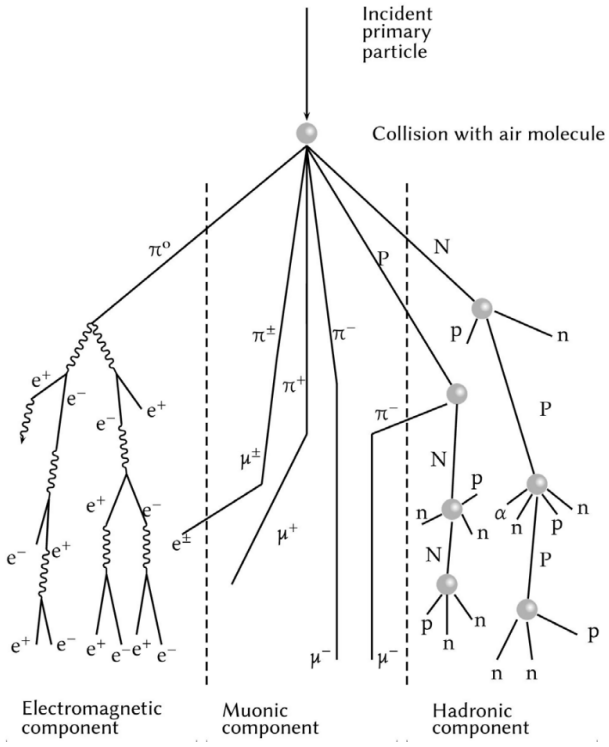

Figure 3.2: Basic scheme of an air shower with its three components. The grey dots denote an radioactive decay and n,p denote neutrons and protons. Capital letters are used in the case of high-energy particles. Figure taken from [22].

3.2 Emission of Cherenkov Light

The direction and the energy of the incoming γ can be reproduced through the observation of the Cherenkov radiation the electromagnetic shower emits. If particles travel through a medium with a velocity greater than the speed of light in that medium the radial symmetry of the matters dipoles get broken. The dipole moments interfere constructively and emit Cherenkov light. The photons are emitted in a cone with an opening angle of:

$$\theta = \arccos(1/\beta n_m), \tag{3.2.1}$$

where β is the particle's velocity divided by the speed of light and n_m is the refraction index of the medium.

3.3 Imaging Atmospheric Cherenkov Technique

Ground-based γ-ray telescopes are based on the Imaging Atmospheric Cherenkov Technique (IACT). Currently, there are three large telescope systems in operation: MAGIC and VERITAS in the northern hemisphere and H.E.S.S. in the southern. These telescopes use focusing mirrors to image Cherenkov light emitted by air-showers onto a photon detection system (Figure 3.3). For primary particles in the TeV range, the maximum of the shower development is at approximately 10 km above sea level and the opening angle of the Cherenkov cone is $\leq 0.7°$ [23]. Depending on

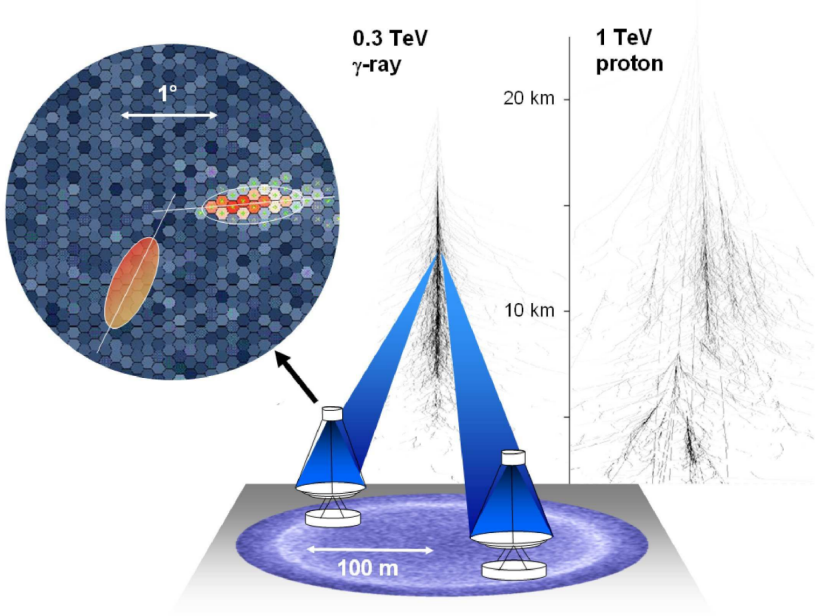

Figure 3.3: Sketch of the Imaging Atmospheric Cherenkov Technique. The cascades induced by a 0.3 TeV γ-ray and a 1 TeV proton are shown. They differ both in lateral and longitudinal depth. Two telescopes are within the Cherenkov light cone emitted by the electromagnetic air-shower. The pixelated image of the shower obtained from the two telescopes is shown. Figure taken from [23].

the height above sea level of the telescope the diameter of the cone at the ground is approximately 250 m.
Multiple telescopes are placed within a region of that size to enable stereoscopic measurements. This allows imaging the air-shower from different viewing angles improving direction reconstruction and rejection of background. In addition, coincidence requirements are enabled. Only about 100 Cherenkov photons emitted by one TeV γ-ray per m^2 are seen on the ground. For the detection of this very faint and short-lived (few ns) Cherenkov light, a short read-out window is necessary.

In the following, the H.E.S.S. will be the focus of discussion since all data used in this work was obtained by this telescope system which is based on IACT.

3.4 The High Energy Stereoscopic System

The High Energy Stereoscopic System (H.E.S.S.) is a γ-ray detection experiment named after Victor Hess, Nobel prize winner for the discovery of cosmic rays. It is located in Namibia at a height of 1800 m a.s.l. and shown in Figure 3.4. In 2002 and 2003 the first four 12 m telescopes (CT1 to CT4) were built (first phase in the following called HESS I). They are arranged in a square with a side length of 120 m such that the base length is large enough but also allowing a stereoscopic measurement. These four telescopes mirrors, segmented into 382 round mirror facets, have a focal length of 15 m. Each telescope has a total mirror area of 108 m^2. The camera of the HESS I telescopes has a 5° field of view and consists of 960 photomultipliers (PMTs). The energy range covers 100 GeV up to approximately 100 TeV [24].

Figure 3.4: View of the H.E.S.S. array with the four HESS I telescopes and the larger HESS II telescope. Image credit: H.E.S.S. Collaboration, Clementina Medina [24].

Since 2012 the larger fifth telescope CT5 of the second phase (HESS II) is in operation. It is in the centre of the existing array and improves the sensitivity and coverage towards lower energies (40 GeV in hybrid mode). Consisting of 875 hexagonal facets the mirror has a focal length of 36 m and a total area of 614 m^2. 2048 PMTs make up the HESS II camera resulting in a field of view of 3.2°.
The camera of the original HESS I array was replaced in 2016 to improve overall performance. The phase with the upgraded telescopes is called HESS IU.

3.4.1 Observations

Observations are taken using the wobble mode. In this method, the source is not in the centre of the FoV but is offset by a small distance of ±0.5°. The offset is alternated in Right Ascension and Declination between 28 minutes observations (runs). In wobble mode, the side of the field of view without the source is used as a control region for background estimations.

H.E.S.S. has several level trigger systems. First, there is the single-pixel threshold of 4 photo-electrons at the PMT within 1.5 ns. Second, the camera is triggered, if within a sector (square group of 64 pixels) 3 pixels are coincidentally triggered. If the triggered camera is the CT5 camera and H.E.S.S. is run in 'mono mode' (CT5 only), the signal is read out. However in 'stereo mode', it is required that at least two cameras of CT1- CT5 are triggered within 80 ns [25]. Observations with all five telescopes are called 'hybrid mode'.

Air-shower information is affected by systematic uncertainties. These are mainly due to variations of the camera response, degrades of the optical response (including the mirrors), and interactions of particles and light in the atmosphere. To minimize the effects of systematic uncertainties on the flux and energy spectrum certain data quality criteria are applied. One of them is the requirement of a stable trigger rate

close to the predicted level. If the rate is less than 70 % of the predicted one, for example, due to clouds passing the FoV, the run is rejected. Also runs where the tracking system malfunctioned do not pass the quality checks. Bright light sources, such as lightning, airplanes, or satellites trigger over-current protection.
Calibrations are necessary before the data can be analysed. This involves the identification of bad pixels, the photon electrons to pixel amplitude calibration, and the correction of the optical efficiency.

3.4.2 Analysis

The sensitivity of an IACT depends on its ability to reduce background. Hence, the γ-ray events have to get separated from the hadronic background events. Therefore, the image has to be cleaned to assure only Cherenkov light is contained in the pixels and reject those containing night sky background. The requirement is that pixels above the lower threshold of 5 photoelectrons have a neighbour above 10 photoelectrons, and vice versa, such that only spatially correlated features are selected [25].
The γ-hardon separation is performed based on the geometric form of the events. While hadronic background events are wide and uneven, γ-ray events have the form of a narrow ellipse. Hillas introduced parameters to quantify the width and length of the photoelectron distribution and distance of the image centre to the camera centre (Figure 3.5). The classical background reduction selects the γ-ray events based on cuts on the Hillas parameters determined by MC-simulations. Depending on the source condition, different cut configurations are used: 'standard', 'hard' and 'loose'. In the standard Hillas analysis this includes [26]:

- Local distance (between camera centre and centre of gravity) cut to avoid truncated images.
- Minimal size cut to avoid inaccurate reconstructions due to faint images. Note that the higher the size cut value, the higher the energy threshold.
- 'Mean reduced scaled width' (MRSW) and the 'mean reduced scaled length' (MRSL) cut computed from the measured width (length) and expected width (length) from MC simulations used for hadronic background separation.

An improved background reduction can be obtained via a multivariate, tree classification method [27]. An event is either signal-like or background-like based on passed or failed criteria. These criteria are applied on one of the parameters of the parameter set $M_i = (m_{i,1}, ..., m_{i,6})$ describing the event at each node of a decision tree sketched in Figure 3.6. The appropriate splitting criteria are obtained by training the decision tree with multiple events of known types. The output of a decision tree is a variable ζ describing the signal- or background-likeliness of the event. The γ-hardon selection of the data used in this work was performed by this decision tree-based method.

For the energy reconstruction of the primary particle the sum over all photoelectrons, the amplitude, is calculated.

The major axis of the image corresponds to the projected direction of the shower. By intersecting the major axes of multiple cameras of stereo observations, the arrival

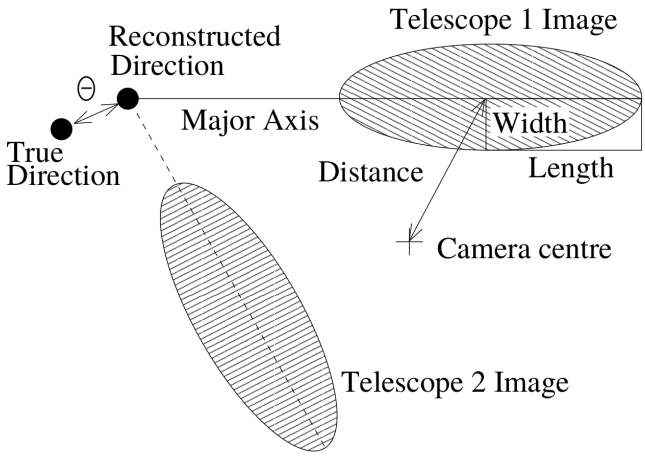

Figure 3.5: Definition of the Hillas parameters width, length and distance for a γ-ray image. By intersecting the major axes of the images of telescope 2 and 1 the direction can be reconstructed. Figure taken from [25].

.

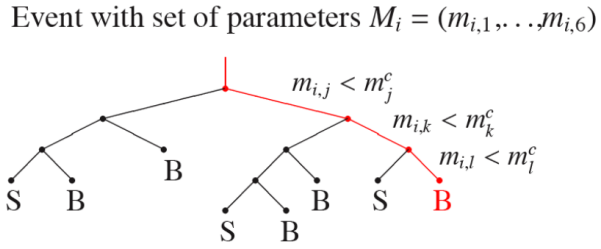

Figure 3.6: Sketch of a decision tree with a binary split criterion at each note. The event described by M_i ends up as either a signal (S) or a background (B). Figure taken from [27].

.

direction of each event is reconstructed.

In Figure 3.5 the parameter θ as the angular offset between the reconstructed and the true direction is shown. The distribution of θ^2 defines the accuracy in the reconstructed direction of γ-rays originating from a point source. It is described by the point spread function (PSF), approximately the sum of two one-dimensional Gaussian functions. The specified point spread function of HESS I is 0.03° on-axis and 0.06° for γ-rays 2° off-axis.

3.4.3 Background Estimation

The images still contain a background signal after the γ-hadron separation. This is due to showers induced by electrons having a similar shape as the γ-ray showers and electromagnetic sub-showers from early interactions of hadronic showers. There are several background estimation and subtraction methods all based on the same principle. An On and Off region is defined, where the On region contains the source and the Off region is chosen such that it does not contain γ-ray sources but is

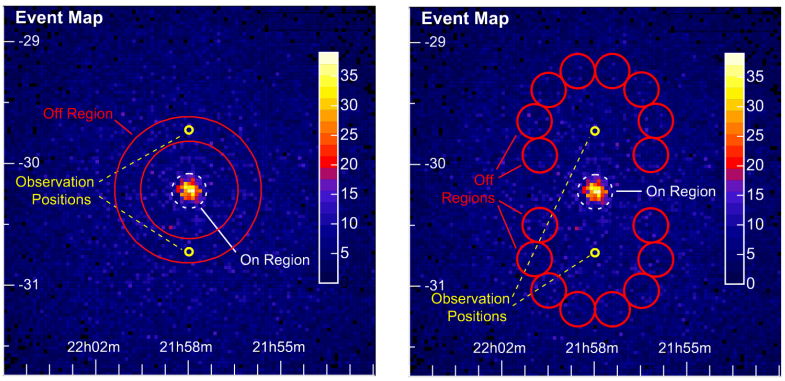

Figure 3.7: Illustration of the ring (left) and reflected (right) background models. Figure taken from [28].

background only. The number of excess events in γ-rays can then be estimated by

$$N_{\text{excess}} = N_{\text{On}} - \alpha N_{\text{Off}}, \tag{3.4.1}$$

where α is the normalisation factor and $N_{\text{On/Off}}$ the number of events in the corresponding region. The significance of the source can be calculated from N_{excess} using the likelihood ratio method (section 4.3). Common methods to estimate the background are the reflected background model and the ring background model. They will be briefly discussed in the following.

Reflected Background Model

The easiest way to estimate the background is to define the Off region in the opposite direction of the On region relative to the centre of the FoV. However, by using only a single reflected background, local inhomogeneities can not be taken into account causing systematic effects. Instead, the Off region consists of numerous background regions, all at the same distance to the observation position as the On region (Figure 3.7). The number of background regions depends on the offset of the On region with respect to the centre to avoid overlapping. The ratio of the solid angles of the On and Off regions determines the normalization α. The reflected background method is suitable for data taken in wobble mode, but can not account for non-radial variations in the acceptance.

Ring Background Model

In the ring background model, the Off region is defined as a ring around the position of the source (Figure 3.7). The inner and outer radius of the Off region is chosen such that the ratio of the On and Off region is approximately 7. The value is a compromise between the distance to the source and the area within the Off region. The radial background acceptance is taken into account for by the normalization α by modifying the ratio of the On and Off region with a weight factor. However, the calculation of the energy-dependent acceptance is averaged over multiple observation resulting in possible systematics. This makes the ring background model not suitable for spectral analysis.

For both the reflected and the ring background model it is crucial to have a large region within the FoV with no γ-ray emitting sources to use as the Off region. Due to the large diffuse emission and multiple γ-ray emitting sources this is not the case for the Galactic Centre region. Therefore, another background model was developed which does not make use of Off regions. This so-called three-dimensional background model will be discussed in Chapter 5.1.

Chapter 4

Data Analysis

In Section 3.4.3 two standard background estimation models both relying on an Off region within the FoV were discussed. However, for regions with a dense γ-ray source population or large-scale γ-ray diffuse emission, the methods are not suitable. The Galactic Centre region analysed in this work falls into this category. Therefore, an other analysis technique is used, the three-dimensional (3D), energy-resolved likelihood analysis. The field of view is described by a combination of three-dimensional models which are fitted to the observed data via a likelihood formalism. In the first part of this chapter, the used data is discussed followed by an introduction of the 3D fitting method. Afterwards, it is described how one obtains upper limits on a fitting parameter via the likelihood ratio test and a short introduction of Asimov data sets is given. The methods are applied in the DM analysis (Chapter 6).

4.1 Data Sets

For the analysis, data sets from different H.E.S.S. phases are used. The HESS I data set consists of 424 runs (197 hours of live-time in total) taken between 2004 and 2013. In the HESS II phase, 96 hours of data were taken in 215 runs. The HESS IU data set obtained after the update consists of 114 runs (51 hours of live-time in total). To each of the data sets the HAP standard zeta cuts were applied and they are FITS-HD production 05. This means that only 4 telescope observations are included which does not result in a better performance at lower energies.
The distribution of the zenith angles of the runs of the different telescope phases is plotted in Figure 4.1. The mean zenith angles and the standard deviations are listed in Table 4.1 together with the mentioned information about the live-time, the mean energy threshold, amount of runs, and amount of counts of the data sets. The zenith angle determines the energy sensitivity of the observation. Since the HESS II data set has the lowest mean zenith angle of $19.68° \pm 12.50°$ it is expected to have a good sensitivity towards lower energies compared to the other two data sets. However, since currently only 4 telescope observations are included in the data sets, the HESS II does not result in a better performance at low energies. The exposure of the telescope in the three different phases are shown in Figure A.1 (a) and (b), and A.2 to visualise where the pointing of the telescope within the region of interest was.
In this work, the HESS I data set is analysed individually as well as a combined

Data set	**HESS I**	**HESS IU**	**HESS II**	**HESS I+IU+II**
Mean zenith angle [°]	22.52 ±13.66	27.29 ±16.16	19.68 ±12.50	21.86 ±13.97
Live-time [h]	197	51	96	344
Runs	424	114	215	753
Counts [10^5]	6.33	1.98	1.87	10.18
Mean energy threshold [TeV]	0.41 ±0.23	0.45 ±0.33	0.44 ±0.24	0.42 ±0.25

Table 4.1: Mean zenith angle, livetime, runs, total amount of counts, and mean energy threshold for each of the used data sets HESS I, HESS IU, HESS II and the combined one HESS I+IU+II

analysis of the HESS I+II and HESS I+IU+II. The region of interest was analysed within a box of size $[4.3°, 4.3°]$ with the Galactic Centre in the centre.

4.2 Three Dimensional Maximum Likelihood Fit with Gammapy

The analysis is performed with the open-source tool Gammapy version 0.14 [29] which has been validated in [30]. Two fitting methods are available: a 'joint' and a 'stacked' fit. In the former, the final likelihood value is a product of the likelihood values obtained by fitting each run individually. A 'stacked' likelihood fit is performed on the sum of all runs resulting in only one likelihood value. Since also the instrument response functions (IRFs) are averaged a 'stacked' fit results in a less accurate description of the data. However, for larger data sets, it is not as computationally expensive as a joint fit since less fit parameters are necessary. In this work, stacked likelihood fits are performed.
The data can be visualized in the form of sky-maps. They consist of 64 bins in the two spatial dimensions each and 130 bins in the third dimension, the energy. The energy bins reach from approximately 0.2 TeV to 84 TeV and are logarithmically spaced. In each of the bins a Poisson log-likelihood function, the cash statistic, is calculated. It is derived from the likelihood $\mathcal{L}$, the product of individual Poisson probabilities (counts are sampled from the Poisson distribution) calculated in each bin i:

$$\mathcal{L} = \prod_i \frac{M_i^{D_i}}{D_i!} \exp\left(-M_i\right), \tag{4.2.1}$$

where $M_i = S_i + B_i$ is the sum of the expected counts of the source and background model and D_i is the number of observed counts in bin i.
By taking the logarithm of equation 4.2.1, one gets:

$$\log \mathcal{L} = \sum_i \left[-D_i \log\left(\frac{M_i}{D_i!}\right) + M_i \right] \tag{4.2.2}$$

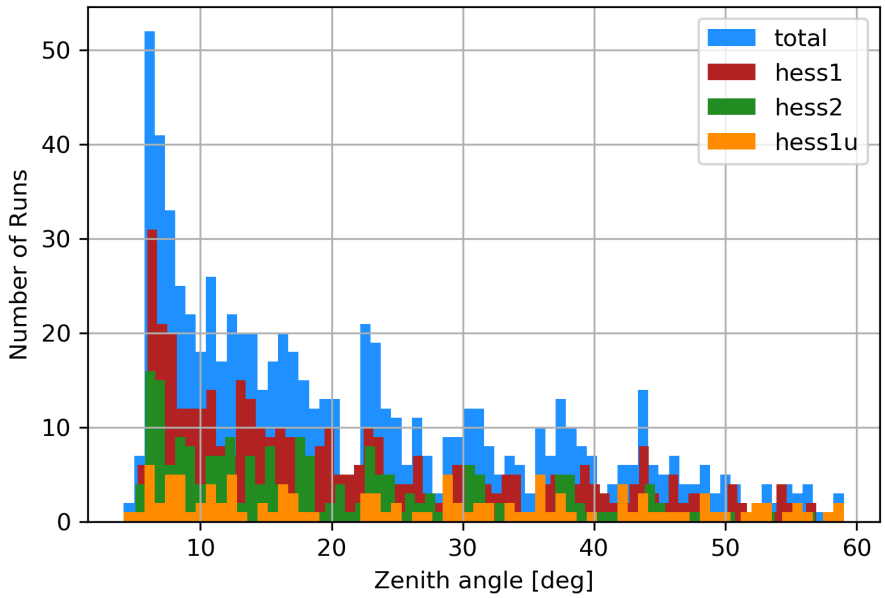

Figure 4.1: Distribution of the zenith angles for the different data sets

Since $\log(1/D_i!)$ does not depend on the models evaluated but remains constant it can be dropped.
One obtains the Cash statistic C_i in bin i by changing the sign and a multiplication by two:

$$-2\log\mathcal{L} = \sum_i 2\left[M_i - D_i\log(M_i)\right] = \sum_i C_i, \tag{4.2.3}$$

The factor of two exists so that the change in Cash statistics can be approximated by the Chi-square distribution with one degree of freedom. If $M_i \leq 0$ the Cash statistic is set to zero.
Since the models and therefore $\mathcal{L}$ are depending on the N nuisance parameters $\vec{\theta} = (\theta_1, .., \theta_N)$ the likelihood is a N-dimensional function. The best values of the parameters $\hat{\vec{\theta}}$ are obtained by maximising $\mathcal{L}$ which is equivalent to minimising $-2\log\mathcal{L}$. Note that one cannot assign a goodness-of-fit measure to a given $\mathcal{L}$ value since it depends on the number of bins and the values of the data.

The likelihood profile is defined as a 'slice' or a 'scan' of the N-dimensional $\mathcal{L}$. It displays the $-2\log\mathcal{L}$ as a function of only one of the parameters $\vec{\theta}$. One can either freeze all the other parameters to their best-fit value or re-optimise them when computing the profile. The likelihood profile is used to calculate both the errors and the upper limits on the fit parameters. The method is discussed in the following.

4.3 Likelihood Ratio Test

The following is based on [31]. When setting limits on a new discovery one defines two hypotheses and tests them against each other. The first one is the null hypotheses H_0, which describes the signal and the background. H_1 is the background only hypotheses. One defines the p-value which is the value of the probability under

the assumption H to find data predicted by H more or equally incompatible with H. Here the p-value for the background only hypotheses H_1 is calculated. If p_{H_1} is below a certain threshold value p, H_1 is excluded. It is possible to convert the p-value into a significance Z which is more commonly used in particle physics:

$$Z = \phi^{-1}(1-p), \tag{4.3.1}$$

where ϕ^{-1} is the inverse of the cumulative distribution of the standard Gaussian. The p-value is equal to the upper tail probability of a variable found Z standard deviations above its mean (Figure 4.2 (a)). A signal with a Significance of at least 5 ($p = 2.87 \cdot 10^{-7}$) is considered a discovery. The threshold of the p-value for excluding a hypothesis, in this case H_1, is usually set to 0.05 ($Z = 1.64$). This corresponds to a 95 % confidence level. One way of calculating the incompatibility is to measure the likelihood ratio between the signal and the background as a test statistic. The background model is depending on nuisance parameters $\vec{\theta} = \theta$, which are fitted from the data. The signal is described by a parameter μ. The fitting of the nuisance parameters increases systematic uncertainties and therefore a loss of information. This results in a broadening of the profile likelihood as a function of μ. The profile likelihood ratio is

$$\lambda(\mu) = \frac{\mathcal{L}(\mu = 0, \hat{\hat{\theta}})}{\mathcal{L}(\hat{\mu}, \hat{\theta})}. \tag{4.3.2}$$

$\hat{\theta}$ is the maximum likelihood estimator of θ and therefore depending on μ. $\hat{\hat{\theta}}$ maximizes the likelihood in the case of $\mu = 0$. As the bias of the statistical test one uses

$$t_\mu = -2 \log \lambda(\mu). \tag{4.3.3}$$

An increasing incompatibility between the $\mu = 0$ and the $\hat{\mu}$ case results in a large t_μ. This incompatibility can be quantified by calculating the p-value for the observed test statistic $t_{\mu,\text{obs}}$

$$p_\mu = \int_{t_{\mu,\text{obs}}}^{\infty} f(t_\mu|\mu)\, dt_\mu, \tag{4.3.4}$$

where $f(t_\mu|\mu)$ is the probability density function of t_μ under the assumption of a signal with the strength μ. It is a chi-square distribution for one degree of freedom (Wilk's theorem):

$$f(t_\mu|\mu) = \frac{1}{\sqrt{2\pi}} \frac{1}{\sqrt{t_\mu}} \exp(-t_\mu/2) \tag{4.3.5}$$

The relation is illustrated in Figure 4.2 (b).
The cumulative distribution function of t_μ is therefore

$$F(t_\mu|\mu) = \phi\left(\sqrt{t_\mu}\right). \tag{4.3.6}$$

When observing t_μ, one gets the p-value:

$$p_\mu = 1 - F(t_\mu|\mu) = 1 - \phi\left(\sqrt{t_\mu}\right) \tag{4.3.7}$$

and a significance of

$$Z_\mu = \phi^{-1}(1-p_\mu) = \sqrt{t_\mu} \tag{4.3.8}$$

A signal μ is considered as a discovery if its test statistic is greater or equal to 25 ($Z \geq 5$). The 95 % upper limit on the parameter is such that its test statistic has a

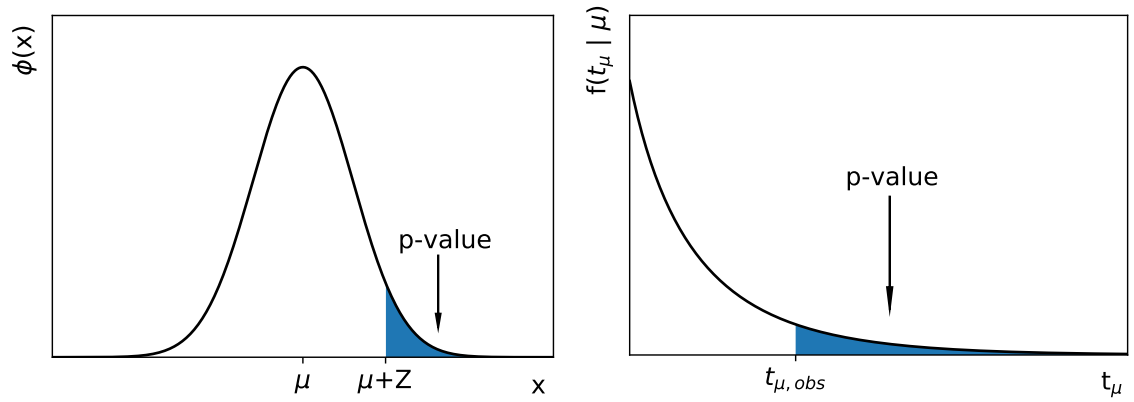

(a) (b)

Figure 4.2: Illustrations of the relation between the p-value (blue area) and (a) the significance Z and (b) the observed test statistics $t_{\mu,\text{obs}}$.

value of 2.71 which is equivalent to a significance of 1.64. A test statistic value of 1 corresponds to the 1σ error.
In Figure 4.3, two likelihood profiles as functions of the parameter μ are shown. They can be approximated by a parabola with the minimum being the best-fit value $\hat{\mu}$:

$$-2\log\lambda(\mu) = \frac{(\mu-\hat{\mu})^2}{\sigma^2} + \mathcal{O}(1/\sqrt{N}), \tag{4.3.9}$$

where N represents the data sampling size.

The test statistics can be calculated from a given likelihood profile. Rewriting equation 4.3.3 allows an easy visual interpretation of the connection between t_μ and the profile:

$$t_\mu = -2\log\lambda(\mu) = -2\log\frac{\mathcal{L}(\mu=0,\hat{\hat{\theta}})}{\mathcal{L}(\hat{\mu},\hat{\theta})} = 2\log\mathcal{L}(\hat{\mu},\hat{\theta}) - 2\log\mathcal{L}(\mu=0,\hat{\hat{\theta}}) \tag{4.3.10}$$

Figure 4.3 (a) shows a likelihood profile with a corresponding test statistic $t_\mu > 5$ so the signal μ would be considered a discovery. The 1σ error on the best-fit parameter $\hat{\mu}$ is such that:

$$-2\log\mathcal{L}(\hat{\mu}+1\sigma) = -2\log\mathcal{L}(\hat{\mu}) + 1 \tag{4.3.11}$$

The likelihood profile in Figure 4.3 (b) does not result in a discovery since $t_\mu < 5$. However, the 95 % upper limit $\mu_{UL} = \hat{\mu} + 1.64\sigma$ can be derived from the likelihood profile by looking for the value of μ_{UL} where:

$$-2\log\mathcal{L}(\mu_{UL}) = -2\log\mathcal{L}(\hat{\mu}) + 2.71 \tag{4.3.12}$$

4.4 Asimov Data Sets

Obtaining the expected experimental sensitivity of a search or an experiment usually requires Monte Carlo (MC) simulations. To obtain a representative result, a

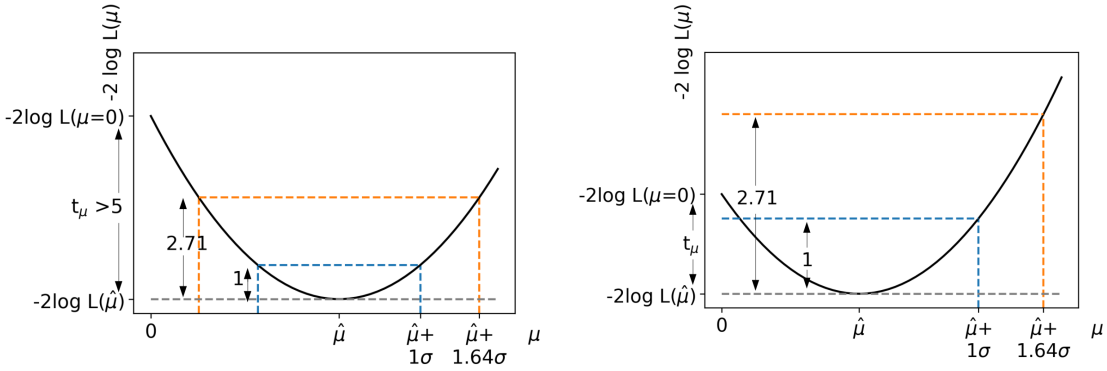

Figure 4.3: Illustrations of two likelihood profiles as a function of μ with a minimum at $\hat{\mu}$. The test statistics t_μ is the difference between the value of the function at $\mu = 0$ and $\hat{\mu}$. Both the 1σ error and the 95% UL of the parameter μ are shown. Since in (a) $t_\mu > 5$ the signal is a discovery which is not the case in (b).

sufficient number of MC simulations is necessary, which is very computationally expensive. A simpler and faster method is provided by the use of a representative data set, called the 'Asimov' data set [32]. It is defined such that the best-fit parameters of the Asimov data set are the true parameter values. They are the same values that would be obtained by a very large sample of MC simulations. In this work, Asimov data sets are created by fitting the model to a sky map filled with the counts predicted by the model. One can check whether the obtained values are the median of the results obtained by MC simulations. The simulated maps are Poisson draws from the Asimov data set sky maps.
The method is used in Chapter 6 to perform an 'Injection and Recovery' test. Thereby an artificial DM signal gets injected to the data to see whether the fitting process can recover the signal. Analysing the Asimov data set with no DM signal induced allows an estimation of the systematic effects of the fitting process on the obtained upper limits on the DM cross-section.

Chapter 5

Three Dimensional Analysis of the Galactic Centre Region

For the computation of the DM upper limits within the Galactic Centre region, it is crucial to describe all the other γ-ray sources in that area as good as possible. Otherwise, a possible photon produced by DM annihilation is not interpreted as a DM signal. In this chapter, the region of interest is analysed without a DM component to assure that the region is described properly with a model containing only the established γ-ray sources. The model is grouped into three components: the background due to cosmic rays, the large-scale diffuse emission along the Galactic Plane, and three astrophysical γ-ray emitting objects. In the first part of this chapter, these components and how they are modelled is discussed in detail. Later the focus is on the fit results and the quality of the fit estimated by looking at the significance distribution of the residuals.

5.1 Model Components

In the following, the three γ-ray emitting components starting with the important description of the background, the diffuse emission, and the astrophysical sources are discussed. The astrophysical sources are the two point sources HESS J1745-290 and G09+0.1, and the extended source HESS J1745-303. Afterwards, the combination of the components is illustrated.

5.1.1 Background Model

The following is based on [30].
In the case of the Galactic Centre, a background estimation like the reflected background or the ring background model is not suitable due to multiple γ-ray emitting sources and a large-scale γ-ray diffuse emission both described more in detail in section 5.1.3. Instead, the three-dimensional description of the cosmic ray background flux is constructed from archival H.E.S.S. observations which do not contain known γ-ray diffuse emission like the Galactic Plane. Since the background rate depends strongly on the pointing direction of the telescopes the observations were grouped in bins of the zenith angle (ϑ) and the azimuth angle (ϕ). There were two bins used for the azimuth angle ($-90° < \phi < 90°$ and $90° < \phi < 270°$) and eight for the zenith angle (reaching from 0° to 60°). The logarithmically spaced energy axis reaches from

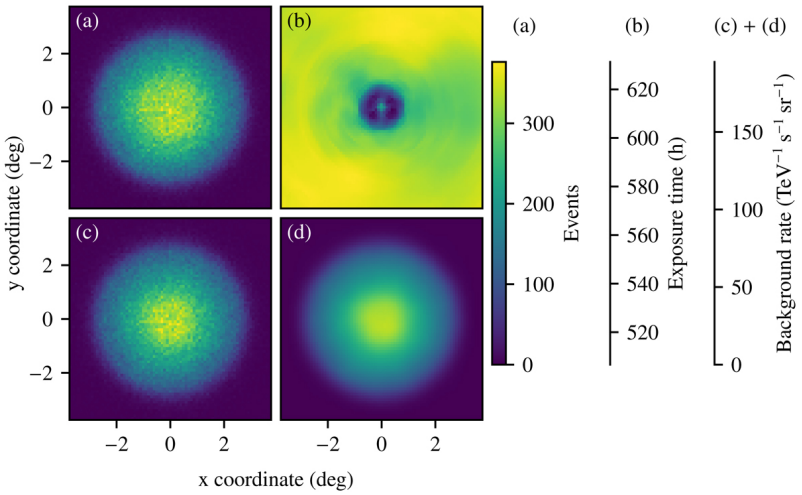

Figure 5.1: Illustration of the background model construction in the bin with $90° < \phi < 270°$, $20° < \vartheta < 30°$ and $0.8\text{TeV} < E < 1.1\text{TeV}$. (a) Sum of all the counts of all the observations. Events close to γ-ray sources are excluded. (b) Summed up exposure time of all observations with corrections for the excluded events. (c) Averaged background rate, the number of events divided by the corrected exposure time and the bin size (energy interval multiplied by solid angle). (d) Smoothed average background rate after the application of a spline-based smoothing algorithm. Figure taken from [30].

100 GeV to 100 TeV. In every bin, the averaged background rate is computed while events coming from the direction of known γ-ray sources are not taken into account. The exposure is corrected accordingly. The steps of the background template construction are illustrated in Figure 5.1.

The initial background model template is fitted to the data of each observation in each energy bin. Averaging over the results of all energy bins results in a single normalisation value for each observation. The dependency of the normalisation on the zenith angle ϑ is corrected by an interpolation. Otherwise, the selection of the initial model based on the zenith angle bin leads to jumps at the boundaries of the bins.
There are two more corrections necessary: for the atmospheric transparency and the optical phase. The former is quantified by the transparency coefficient computed based on the trigger rate of the telescopes. The larger the value the more transparent the atmosphere and therefore less absorption of the Cherenkov light resulting in a larger background rate. Since the dependency of the background normalisation to the coefficient is linear it can easily be accounted for. The optical efficiency of the telescopes varies within specific periods, for example, due to mirror degradation, defining optical phases. Biases in the background normalisations for some phases are eliminated by applying the average fitted background normalisation as a correction factor.
The background template has two fit parameters: the normalisation and the tilt δ. The latter modifies the predicted background rate R at energy E as

$$\bar{R} = R \cdot (E/E_0)^{-\delta}, \tag{5.1.1}$$

where $E_0 = 1\,\text{TeV}$ is the fixed reference energy.

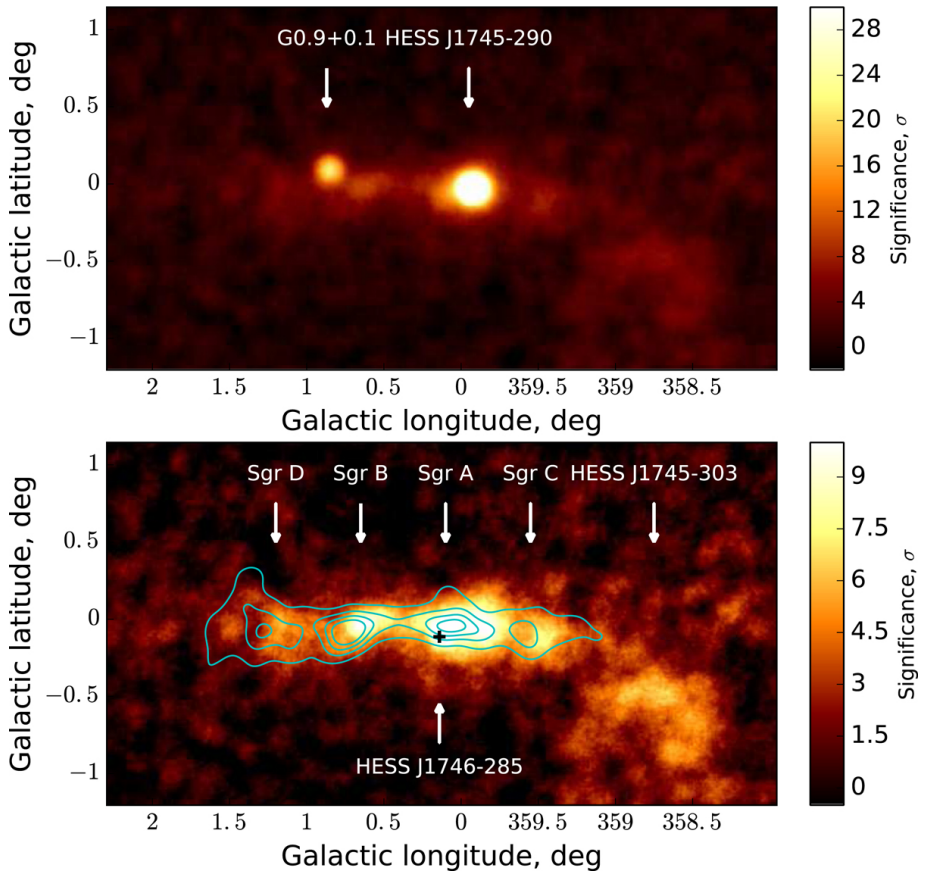

Figure 5.2: γ-ray significance map of the Galactic Centre region, smoothed with the H.E.S.S. PSF. Top panel: position of the sources G09+0.1 and HESS J1745-290. Bottom panel: residual significance map after subtracting the two point sources G09+0.1 and HESS J1745-290. The contours indicate the density of the molecular clouds. Figure taken from [33].

5.1.2 Astrophysical Sources

Figure 5.2 shows the γ-ray image of the inner 200 pc of the Galactic Centre region taken by H.E.S.S. It is displayed in Galactic coordinates and smoothed with the H.E.S.S. PSF. In the upper panel the two very significant sources HESS J1745-290 and G09+0.1 are visible. The former is very close to Srg A*, the supermassive black hole in the centre of the Galaxy. Since it is a point source its morphology is described by the position in Galactic longitude (l) and latitude (b) only. The spectrum is a power law with an exponential cutoff:

$$\phi(E) = \phi_0 \left(\frac{E}{E_0}\right)^{-\Gamma} \exp(-\lambda E), \tag{5.1.2}$$

where ϕ_0 is the amplitude in units of $1/\mathrm{cm}^2\,\mathrm{s}\,\mathrm{TeV}$, E_0 the reference energy, Γ the spectral index and λ the inverse of the cutoff energy. E_0 is fixed to a value of 1 TeV. All the other parameters are obtained by a likelihood fit to the data. HESS J1745-290 can, therefore, be described by five parameters.

The pulsar wind nebula G09+0.1 is coincident with the HESS J1747-281. The morphology is also only described by the position since it is not extended. The

spectrum of G09+0.1 can be described by a simple power law:

$$\phi(E) = \phi_0 \left(\frac{E}{E_0} \right)^{-\Gamma}, \tag{5.1.3}$$

with the same notation as in equation 5.1.2. Hence, four fit parameters correspond to the source G09+0.1.
In the lower right corner of the bottom panel of Figure 5.2 an extended excess is visible. It is the γ-ray source HESS J1745-303 which is not in the Galactic Plane but in the line of sight. In some analysis the region is excluded. Here, however, it is included in the fit. Its complex morphology is approximated with a two-dimensional, symmetric Gaussian:

$$\phi(b) = \frac{1}{2\pi\sigma^2} \exp\left(-\frac{1}{2} \frac{\theta^2}{\sigma^2} \right), \tag{5.1.4}$$

where θ is the sky separation to the model centre (in l and b) and σ is the extension in degrees. The power law defined in equation 5.1.3 is used as the spectrum of HESS J1745-303.

5.1.3 Diffuse Emission Model

After subtracting the excess due to the two point sources G09+0.1 and HESS J1745-290 the most significant component is a large-scale γ-ray emission (Figure 5.2 bottom panel). Its origin is explained in the following.

The galaxy produces cosmic rays up to approximately 100 TeVs [34]. Since these high-energy particles are charged, they get deflected by interstellar magnetic fields and their original direction cannot be reproduced. However, they interact with light and gas in the neighbourhood of their sources. A very strong proton source was suggested to be in the Galactic Centre. The protons propagate diffusively and interact with the Central Molecular Zone gas. Thereby, neutral pions are getting produced which decay into γ-rays or other sub-products. The spectrum of the γ-rays produced by these proton-proton interactions follows a power law.
Based on this physics, a three-dimensional emission template can be created. One artificially injects impulsive protons (100 GeV - 100 PeV) at the Galactic Centre with a spectrum of $E^{-\Gamma}$. The protons diffuse isotropically:

$$\frac{\partial n(E_p, r, t)}{\partial t} = D(E_p) \nabla^2 n(E_p, r, t), \tag{5.1.5}$$

where $n(E_p, r, t)$ is the density of the protons and $D(E_p)$ the diffusion coefficient in cm^2/s

$$D(E_p) = D_0 \left(\frac{E_p}{10\,\mathrm{GeV}} \right)^{\delta} \tag{5.1.6}$$

The parameters of the emission model were found by performing a three-dimensional likelihood fit of the combined data sets HESS I+IU+II: Diffusion time $t = 1.4 \cdot 10^4$ yrs, proton index $\Gamma = 1.921$, $D_0 = 8.72 \cdot 10^{27}\,\mathrm{cm}^2/\mathrm{s}$ and $\delta = 0.4$. This results in a γ-ray diffusion index of 2.26.

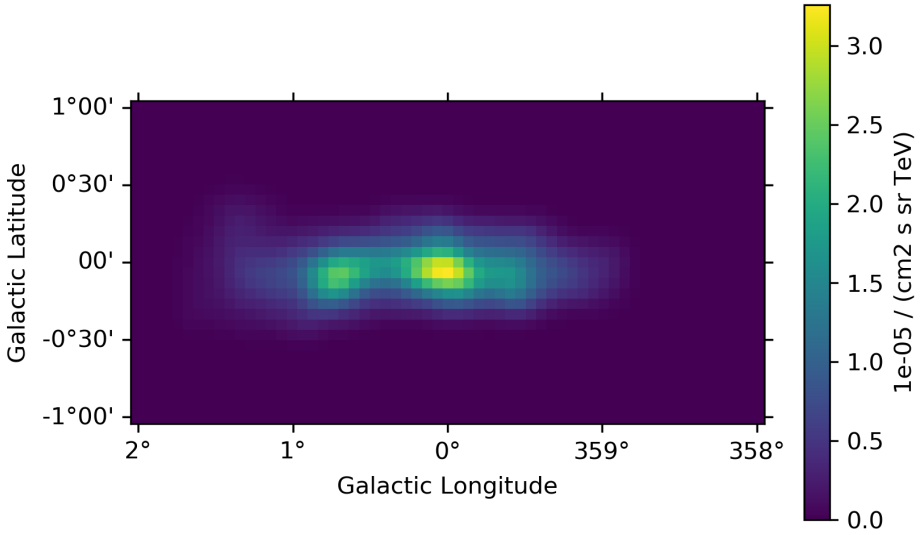

Figure 5.3: Model template of the diffuse emission summed up over all energies.

The diffuse emission template used in the analysis is shown in Figure 5.3 in the unit of flux per solid angle and per energy interval $1/\mathrm{cm}^2\,\mathrm{s}\,\mathrm{sr}\,\mathrm{TeV}$ [35]. The normalisation of the template is the only fit parameter.

5.1.4 Combined Model Cube

By adding the three introduced model components, background, astrophysical sources, and diffuse emission, the three-dimensional model cube is created. It is displayed in Figure 5.4 together with the data cube (taken in the HESS I phase). Note the energy dependency of the morphology and amplitude of both the model and the data cube.

5.2 Fit Results

The best-fit parameters of the astrophysical sources are shown in Table 5.1. The results published in [33] are used as reference values. The best-fit parameters of the two point sources HESS J1745-290 and G09+0.1 are in very good agreement with the reference. As expected the obtained parameters for the extended source HESS J1745-303 show deviations to the results from [33]. Also, the errors on the position in l and b of HESS J1745-303 are one magnitude greater compared to the two point sources. This is due to the fact that HESS J1745-303 is hard to model and its complexity was approximated. The extension of its Gaussian morphology was found to be $0.44° \pm 0.02°$. The normalisation of the background model is 0.995 ± 0.002 and the tilt $\delta = (-6.2 \pm 0.19) \cdot 10^{-4}$. The best-fit normalisation of the diffuse template is 1.13 ± 0.03.

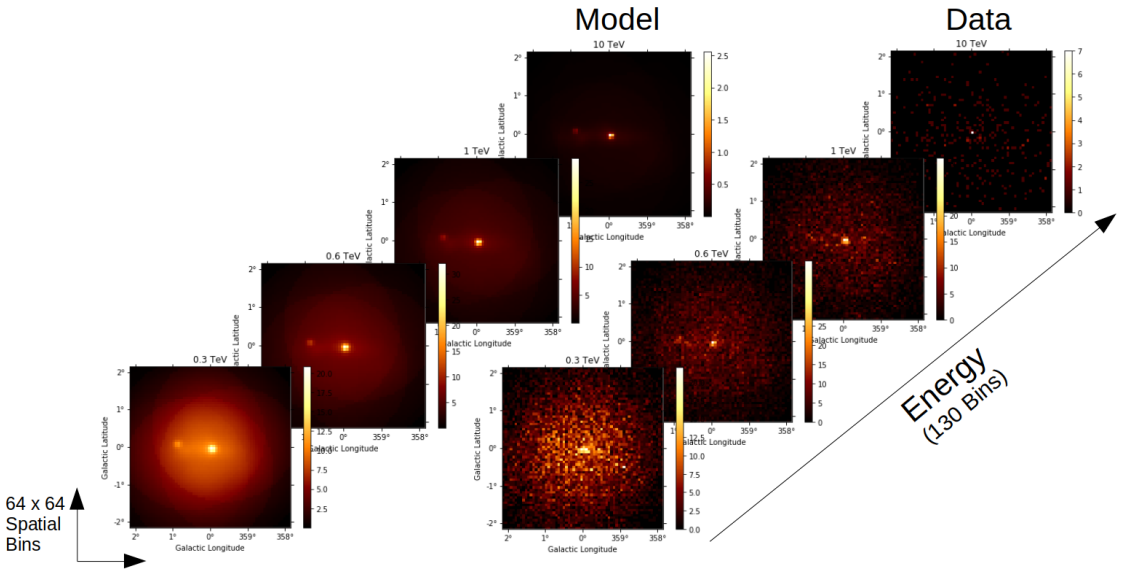

Figure 5.4: Illustration of the three-dimensional model and data cube. Sky-maps showing the morphology of the region and the background are displayed for different energies.

The power-law spectra of the three astrophysical sources are plotted for the obtained parameters in Figure 5.5 within an energy range of [0.2 TeV : 84 TeV]. Also, the flux-points calculated are shown. The flux-points deviate more for smaller energies but overall match the spectrum. Note that for very large energies only the upper limits on the flux were calculated due to low statistics.

The model components with the best-fit parameters can be visually compared with the data by looking at the profiles. Thereby, the counts get summed up along either the Galactic Longitude or Latitude within a 4° x 0.5° or 0.5° x 4° box, respectively, with the Galactic Centre in its centre covering up the entire energy range (Figure 5.6). The single model components are shown in different colours. Overall, the background accounts for the most events showing how important a good description is for the analysis. Since the very strong HESS J1745-290 is located almost exactly at the Galactic Centre it is dominant in both profiles. Its spatial distribution is widened since the modelled point source is convoluted with the PSF. The same holds for G09+0.1. With its longitudinal position being almost 0.9° off the Galactic Centre it does not contribute in the profile along the Galactic Longitude (Figure 5.6 (a)). The smaller excess of the extended HESS J1745-303 is only visible in the profile along the Galactic Latitude. Since the diffuse emission is strongly influenced by the gas distribution along the Galactic Centre it varies with respect to the Galactic Longitude but is almost symmetric for the Galactic Latitude. The combined model is shown in both plots and matches the HESS I data very well. The errors on the counts are the root-mean-square errors. To test the goodness of the fit the reduced χ^2 value was calculated:

$$red.\chi^2 = \frac{1}{N}\sum_{N}\frac{(counts - expected)^2}{expected}, \tag{5.2.1}$$

where $N = 60$ is the number of bins.

this work (HESS I) (reference)	J1745-290	G09+0.1	J1745-303
Flux norm ϕ_0 [10^{12}/**TeV cm^2 s**]	2.81 ±0.079 (2.55 ±0.04)	0.661 ±0.03 (0.88 ±0.04)	6.85 ±0.46 (2.84 ±0.23)
Spectral index Γ	2.02 ±0.04 (2.14 ±0.02)	2.389 ±0.05 (2.40 ±0.11)	2.523 ±0.036 (2.71 ±0.11)
$\mathbf{E_{Cutoff}}$ **[TeV]**	9.89 ±1.36 (10.7 ±2.0)		
Longitude l [°]	359.953 ±0.001 (359.94)	0.867 ±0.003 (0.86)	358.686 ±0.02 (358.71)
Latitude b [°]	-0.047 ±0.001 (- 0.05)	0.076 ±0.003 (0.07)	-0.607 ±0.02 (-0.64)

Table 5.1: Obtained best-fit parameters for the three astrophysical sources. Reference values taken from [33].

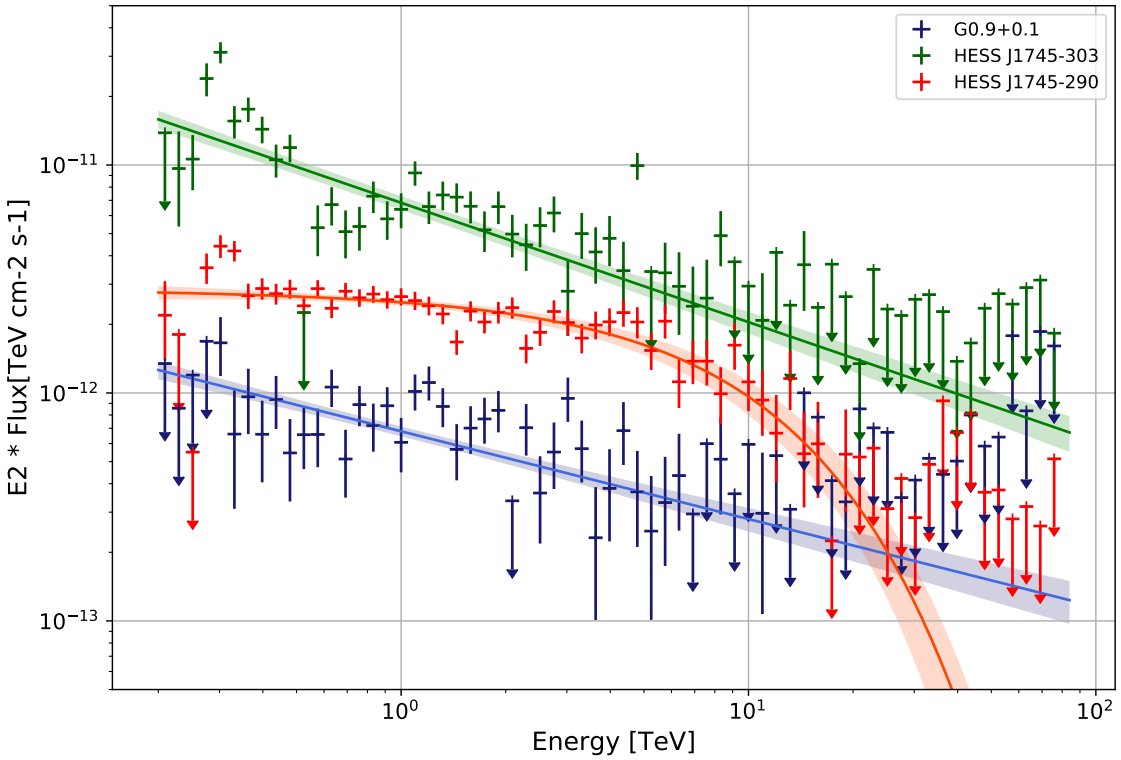

Figure 5.5: E^2·γ-ray flux of the three astrophysical sources, G09+0.1, HESS J1745-290, and HESS J1747-281. Spectrum plotted with the best-fit parameters and error bands and flux-points.

For the profile along the Galactic Latitude one gets red.$\chi^2 = 1.32$ and for the Galactic Longitude red.$\chi^2 = 1.33$ indicating a good agreement of the model with the data even though not fully capturing it. Expressing the obtained χ^2 values in a p-value resulted in $p \ll 0.05$ for both profiles indicating a significant result.

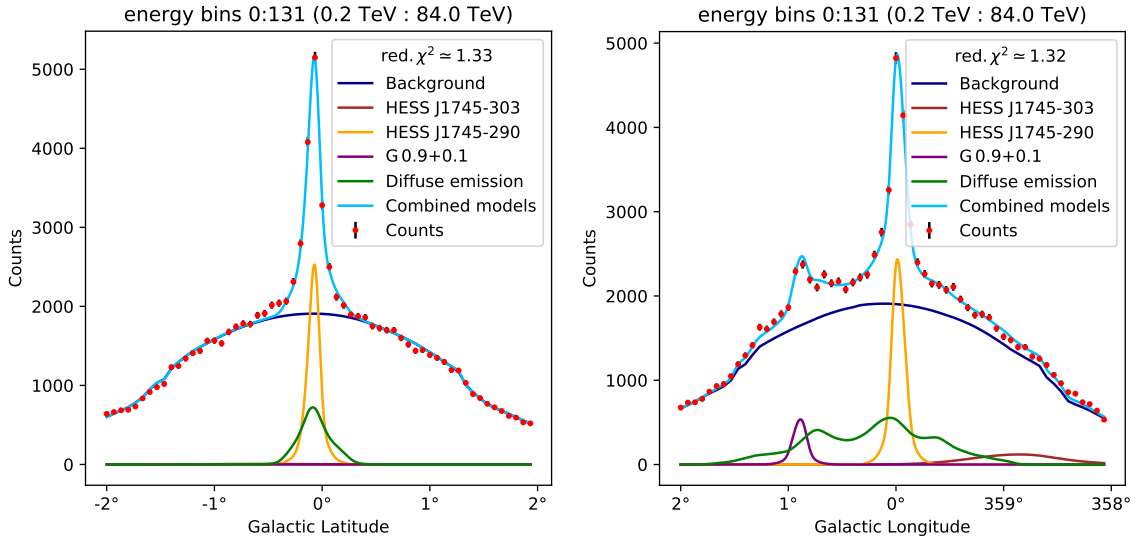

(a) (b)

Figure 5.6: Profiles of the data and model sky-map with its single components along (a) the Galactic Longitude and (b) the Galactic Latitude within a 4° x 0.5° box and a 0.5° x 4° box, respectively. The observed and expected counts are summed up over all energies.

Another way of quantifying the goodness of the fit is to evaluate the significance of the residual sky-maps. Based on Li & Ma the significance of the counts n_{on} with respect to μ is calculated with [36]:

$$S_{lima} = \left[2n_{\text{on}} \log\left(\frac{n_{\text{on}}}{\mu}\right) - n_{\text{on}} + \mu \right]^{1/2} \tag{5.2.2}$$

Figure 5.7 (a) shows the Li & Ma significance with μ being the counts predicted by the model summed up over all energies. To make the large-scale fluctuations visible the map was smoothed with a Gaussian with a width of 0.08°. The map is reasonably flat indicating a good fit.
A more quantified verification of the goodness of the fit can be obtained by looking at the distribution of the unsmoothed significance over all energies (Figure B.1). The distribution is shown in Figure 5.7 (b). Ideally, it is a Standard Gaussian ($\mu = 0$, $\sigma = 1$). There is no excess in the data that is not or too much accounted for indicated by the observed mean of -0.023 being very close to zero. The standard deviation was found to be 1.037. The sum of the squared systematic and the squared statistical error of the fit is, therefore, equivalent to $\sigma^2 = 1.075$ ensuring a good quality of the fit.
The distribution was also investigated for different energies individually (Figure B.2). For smaller energies, a sufficient description of the Galactic Centre region was found.

However, for energies greater than approximately 12 TeV the mean of the distribution shifts to greater values. When looking at the smoothed significance residuals in these energy ranges an over-prediction of the diffuse emission is visible (Figure B.3). The background template, on the other hand, does not seem to account for the counts. This excess results in a shifting of the Gaussian distribution to higher values. The standard deviation dropping below the ideal value of 1 does not indicate a good description of the data in this energy range. This is due to the decreasing sensitivity of H.E.S.S. at these high energies resulting in low statistics making a good description more difficult.

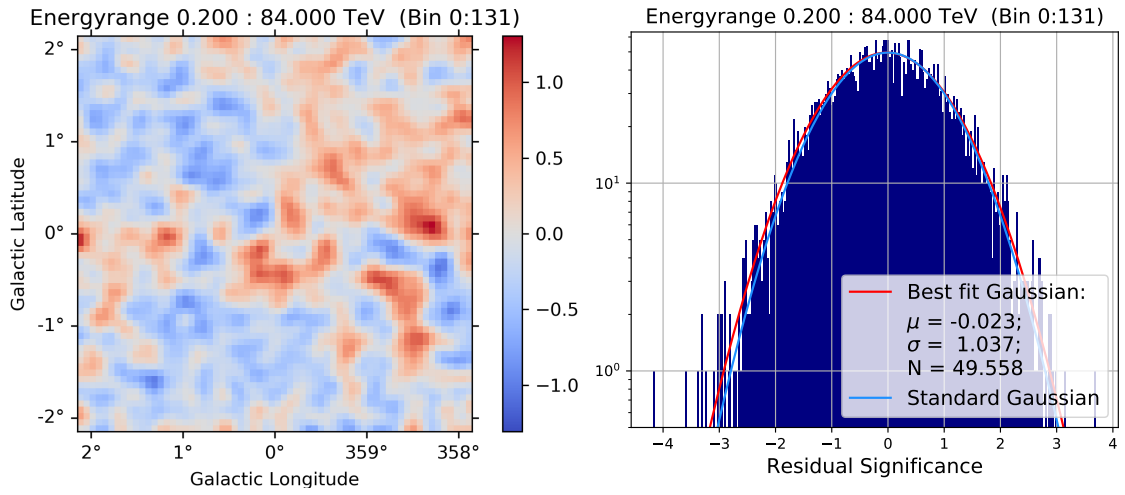

(a) (b)

Figure 5.7: (a) Significance of the residual smoothed with a two-dimensional Gaussian with a width of 0.08° (b) Distribution of the unsmoothed significance of the residual. A one-dimensional Gaussian was fitted to the data with its best-fit parameters being in the legend together with the Standard Gaussian

Since later in the analysis the combined data from the HESS I and the HESS II (and the HESS IU) phase (in the following called HESS I+II (HESS I+IU+II)) is used, the same goodness of fit checks were performed for the combined data sets. The obtained fit results (table B.1) are comparable with the results from the HESS I data. They are within the errors of the reference values except for the hard to model source HESS J1745-303. The reduced χ^2 values obtained in the profile along Galactic Longitude and Galactic Latitude are 1.40 (1.69) and 1.69 (2.16), respectively, for the HESS I+II (HESS I+IU+II) data set. For all cases, the computed p-value is $\ll 0.05$. This indicates a good description of the data by the model components. The profiles are shown in Figure B.4 and B.7.
The smoothed residual significance maps summed over all energies (Figure B.5 (a) and Figure B.8 (a)) are reasonably flat. The unsmoothed significance is Gaussian distributed with its mean at -0.060 (-0.063) for the HESS I+II (HESS I+IU+II) data. The obtained standard deviation is 1.043 (1.039) for the HESS I+II (HESS I+IU+II) data. The results indicate a good fit although the excess at higher energies is not accounted for analogously to the HESS I data.
In Figure B.6 and B.9 the flux-points together with the best-fit spectra of the astrophysical sources obtained from the HESS I+II and the HESS I+IU+II data set

are shown. They are consistent with the HESS I spectra and show a slightly better description at higher energies due to more statistics. The improvements at low energies are not as dominant since the additional counts are observed under the 4 telescope criteria which do not lower the energy threshold.

One can conclude that the overall description of the Galactic Centre region of the HESS I, the HESS I+II and the HESS I+IU+II data sets in three dimensions is good enough to perform further analysis. However, the residuals give rise to the assumption that some of the γ-ray sources are not fully understood and have to be investigated in future analysis of the Galactic Centre region. Additionally, one should take the lower statistics for the very high energy range into account which are expected to influence the computed upper limit on the DM cross-section.

Chapter 6

Results of the Dark Matter Analysis of the Galactic Centre Region

After a good description of the Galactic Centre region was ensured in the previous chapter the DM analysis can be performed. Therefore, a DM three-dimensional model is added to the other model components and the fit is repeated. The three-dimensional model components are discussed in the first part of this chapter. Afterwards, both the results of the DM constraints obtained by the log-likelihood scan and the DM sensitivity are presented and compared to the results from a H.E.S.S. publication. In addition, the upper limit on the annihilation cross-section obtained by a different spatial DM component computed with the open-source tool CLUMPY are discussed.

6.1 Three Dimensional Dark Matter Model Component

In Chapter 2.3.3 the flux of photons produced by DM particle annihilation is divided into a particle physics and an astrophysics part. The former depending on the energy, the assumed DM particle mass m_{DM} and the annihilation channel is interpreted as the spectrum. In Figure 6.1 it is shown for different DM masses and the $b\bar{b}$ channel which is always used in the following analysis unless stated otherwise. The DM particle is assumed to be a Majorana particle ($k = 2$).

Since the astrophysical part of the flux, the J-Factor, only depends on the assumed DM distribution and the region of interest it is used as the spatial component in the three-dimensional DM model. The sky-map for the NFW Profile obtained by calculating the differential J-Factor (equation 2.3.2) in every spatial bin is shown in Figure 6.2 (a). Hereby, the integral limits of the line of sight were chosen to be $[0, 4 \cdot r_{\odot}]$. Contributions to the differential J-Factor beyond $4 \cdot r_{\odot}$ are neglectable. The DM model cube containing the counts per bin (energy bin times solid angle) is obtained by the multiplication of the differential J-Factor with the annihilation spectrum. This model component is parameterized by the velocity averaged annihilation cross-section $\langle \sigma v \rangle$. Expressing $\langle \sigma v \rangle$ in terms of the thermal relic cross-section $\langle \sigma v \rangle = N \cdot \langle \sigma v \rangle_{\text{thermal relic}} = N \cdot 3 \cdot 10^{-26} \mathrm{cm}^3/\mathrm{s}$ makes the normalisation N the only fitting parameter.

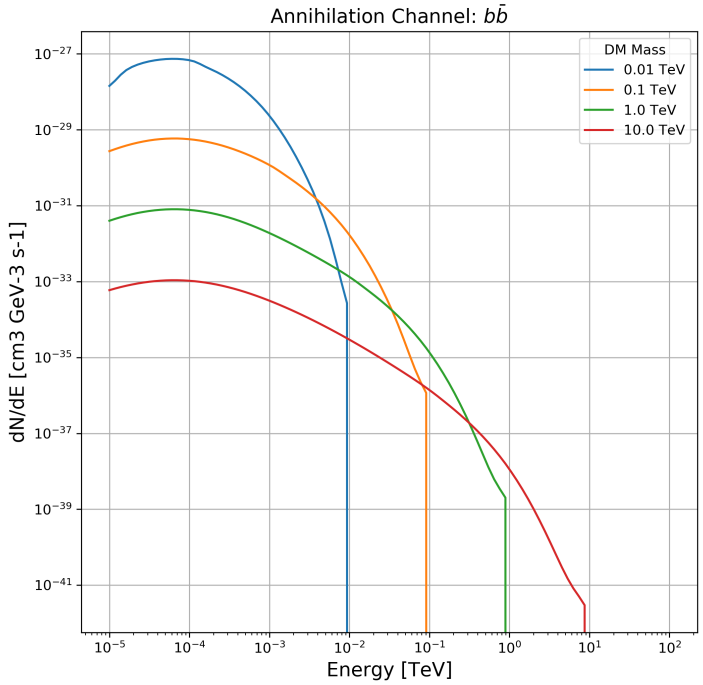

Figure 6.1: $b\bar{b}$ annihilation spectrum computed by equation 2.3.2 (particle physics part) for different assumed DM particle masses $[0.01 : 10.0]$ TeV.

The calculation of the J-Factor was verified by comparing the results with the one published by the H.E.S.S. Collaboration [12]. They calculated the summed-up integrated J-Factor in a circular region of 1° radius excluding a ±0.3° band in Galactic Longitude. The excluded region is to avoid the astrophysical emission. For the Einasto and the NFW profile $J_{\mathrm{E}} = 4.92 \cdot 10^{21}\,\mathrm{GeV}^2\,\mathrm{cm}^{-5}$ and $J_{\mathrm{NFW}} = 2.67 \cdot 10^{21}\,\mathrm{GeV}^2\,\mathrm{cm}^{-5}$ were computed, respectively. In this work, the integrated J-Factors in the corresponding region are $J_{\mathrm{E}} = 4.56 \cdot 10^{21}\,\mathrm{GeV}^2\,\mathrm{cm}^{-5}$ and $J_{\mathrm{NFW}} = 2.41 \cdot 10^{21}\,\mathrm{GeV}^2\,\mathrm{cm}^{-5}$. They are in the same order of magnitude but slightly smaller. This results in a lower DM induced γ-ray flux and, therefore, more conservative limits on the annihilation cross-section. The integrated J-Factor for the NFW profile is shown in Figure 6.2 (b). Also the 1° circle and ±0.3° band used to calculate J_{NFW} are sketched.

6.2 Results

The three-dimensional DM template with a certain m_{DM} is added to the astrophysical sources, the diffuse emission and the background model and fitted to the HESS I data. Afterwards, the likelihood profile gets scanned to obtain the upper limit on the DM normalisation as described in Chapter 4.3. All other fit parameters are getting re-optimised. This is repeated for different DM masses ($m_{\mathrm{DM}} = [0.5 : 30]$ TeV). The calculation was performed with the J-Factor based on the NFW and the Einasto profile. The results are displayed in Figure 6.3 in terms of the DM annihilation cross-

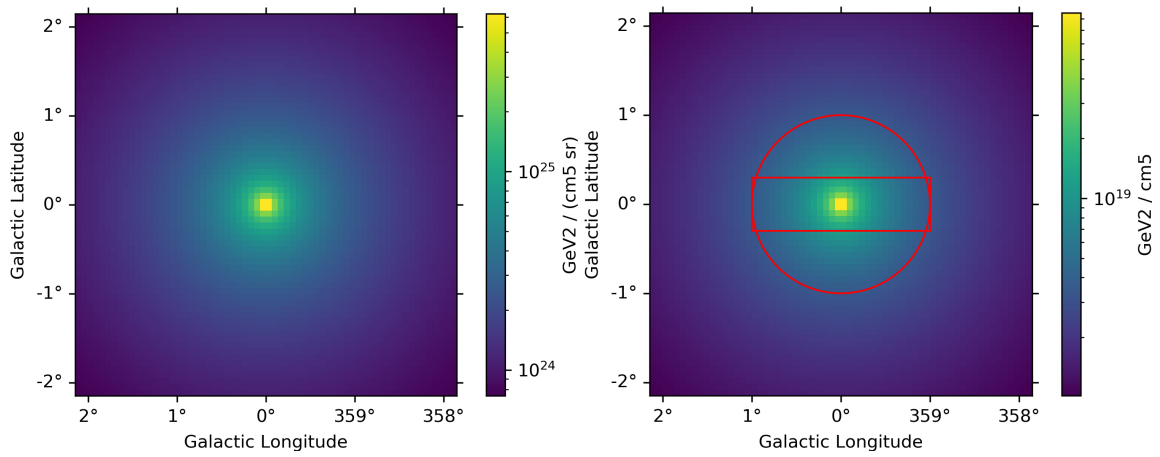

(a) (b)

Figure 6.2: Sky-map of the (a) differential and (b) integrated J-Factors computed for the NFW profile. In (b) the 1° circle and ±0.3° band are shown.

section. The 68 % and 95 % confinement bands shown are calculated from 100 Poisson draws of the real data. The mean constraints of the Poisson draws align with the observed ones. The strongest constraints on the cross-section are $1.43 \cdot 10^{-26}\text{cm}^3/\text{s}$ ($8.00 \cdot 10^{-27}\text{cm}^3/\text{s}$) for a mass of 5 TeV (4 TeV) for the NFW (Einasto) profile. They are below the thermal relic cross-section.
The telescopes DM sensitivity was computed with the help of the Asimov data set. Hereby, the model (including the DM component) was fitted to the predicted counts of the best-fit model (without a DM signal). The obtained upper limits are for both profiles and for the majority of the masses about one magnitude of order larger than the results from the real data. For both profiles, the strongest constraints are at $m_{\text{DM}} = 4\,\text{TeV}$: $1.88 \cdot 10^{-25}\text{cm}^3/\text{s}$ (NFW) and $1.34 \cdot 10^{-25}\text{cm}^3/\text{s}$ (Einasto) and, therefore, above the thermal relic cross-section.
The results published in [12] for the $b\bar{b}$ channel and the Einasto profile are shown in Figure 6.3 (b). The constraints are in the same order of magnitude like the DM sensitivity but a lot weaker than the results obtained by the data. In [12] the Galactic Plane was excluded from the field of view. Therefore, the expected DM annihilation flux drops significantly since in the Galactic Centre the DM density is the greatest. The analysis was not performed in three dimensions. One can therefore expect an overall weaker constraint on the DM cross-section compared to this work. However, the H.E.S.S. publication made use of 254 hours of live time instead of the 197 hours of the HESS I data set used here. The effect of the amount of data used to compute the DM upper limits will be discussed in a subsequent chapter.

The unexpected strong constraints obtained from the real data are due to systematics in the fitting process. The Asimov data set is not affected by them since it was constructed based on the fit of the Galactic Centre region without a DM component. Therefore the DM sensitivity is comparable to the results published in [12].

For both for the DM sensitivity and the actual HESS I data, the constraints computed for the Einasto profile are consistently stronger than the ones for the NFW profile. This was expected since the summed-up Einasto-based J-Factor is greater

than the NFW-based one (as shown in the previous section).

DM constraints are typically weaker at the smallest and highest assumed DM masses. At small masses, this is due to the early cutoff in the γ-ray spectrum. The decreasing sensitivity of the telescope at high energies affects the constraints for large DM masses. The broad distribution of the computed DM sensitivity aligns with the reference. However, the constraints obtained with the real data have a steeper distribution. One can therefore assume that the systematics affecting the upper limit calculation are energy-dependent. Since the spectra of the single model components are taken into account during the fit this is very likely. It is possible that the description of the field of view is not good enough. The DM template could account for an excess of counts which were not sufficiently described by the other model components and vice versa.

The following analysis is an attempt to understand the origin of the systematics and the effects it has on the upper limit calculation. This involves the exclusion of certain areas in the sky-map like the Galactic Centre and the Galactic Plane and the analysis of the combined data sets HESS I+II and HESS I+IU+II. However, the first step to ensure a correct analysis is the verification of the used DM template. The spectrum is directly adapted from [13]. The J-Factor sky-maps for now only validated through a comparison in the magnitude with [12] are the focus of the next section.

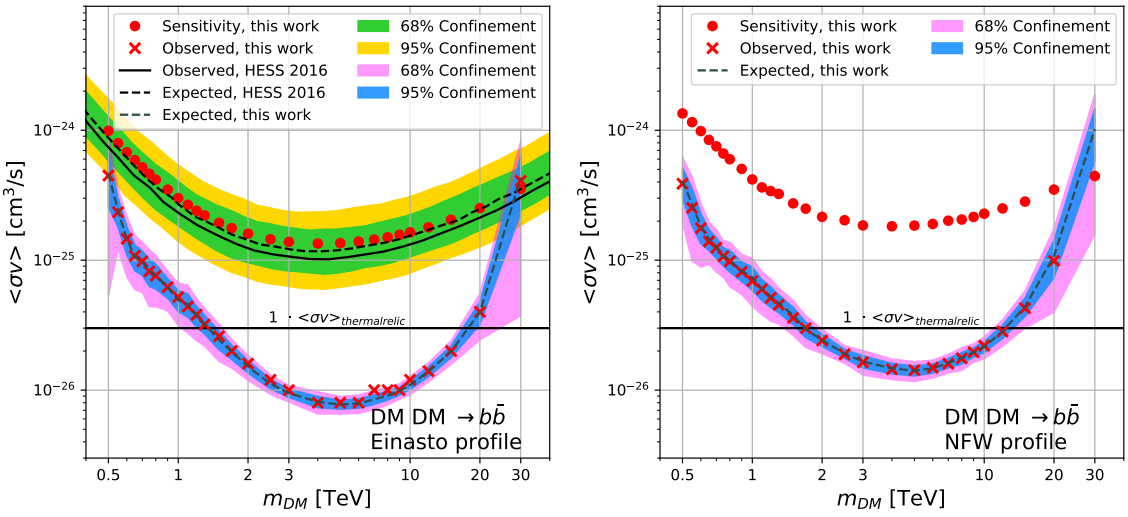

(a) (b)

Figure 6.3: Computed upper limits on the DM annihilation cross-section, DM sensitivity of the HESS I data obtained from the Asimov data set and the results published in [12] for the (a) Einasto and the (b) NFW profile

6.3 Comparison with the J-Factors Computed by CLUMPY

The J-Factors were compared with the ones obtained by the commonly used open-source tool CLUMPY [37, 38, 39]. The sky-maps computed with the parameters listed in Table C.1 are shown in Figure C.1 for the (a) Einasto and (b) NFW profile. Figure 6.4 shows the differential J-Factor as a function of the angular distance in degrees to the Galactic Centre obtained by CLUMPY and the calculation in this work. There are deviations for very large and very small angular distances where they differ by at least a factor of 2. They are likely due to geometrical approximations in the calculation in this work. Since the NFW profile is steeper at small distances (Figure 2.9) the deviations are greater compared to the Einasto profile. For larger distances, on the other hand, the two profiles are more alike resulting in deviations from the CLUMPY differential J-Factors in the same order of magnitude. Even though the deviations in the ON region are small, it results in a slightly different amplitude and morphology in the J-Factor sky-maps. Figure C.2 shows the relative error of the CLUMPY differential J-Factor maps and the maps computed here. The relative error is maximal at the Galactic Centre with a value of approximately 10 %. The calculation of the upper limits on the DM cross-section with the use of the HESS I data set was repeated with the CLUMPY sky-maps. The results are shown together with the ones computed with the J-Factor maps from this work in Figure 6.5. There is a slight shift of the constraints visible. For the NFW (Einasto) profile, the results differ by a mean factor of 1.07 (1.01). The maximal deviation is for $m_{\mathrm{DM}} = 0.5\,\mathrm{TeV}$ by a factor of 1.22 (1.09) for the NFW (Einasto) profile.

The origin of the deviations of the J-Factor sky-maps computed here from the CLUMPY results could not be determined in the scope of this work. This requires further investigation. As expected, they do not account for the deviations of about one magnitude of order from the results published in [12]. Otherwise, this would also be observable in the DM sensitivity. The systematic effects affecting the results obtained by the real data are the focus of the next chapter. The features appear independent of the used J-Factor and it is, therefore, irrelevant which one is used for the evaluation of the systematic effects. Here it was chosen to perform the studies with the J-Factor computed in this work. However, in the final upper limits for other annihilation channels the CLUMPY map is used as the spatial component. This allows a better comparison to the published results.

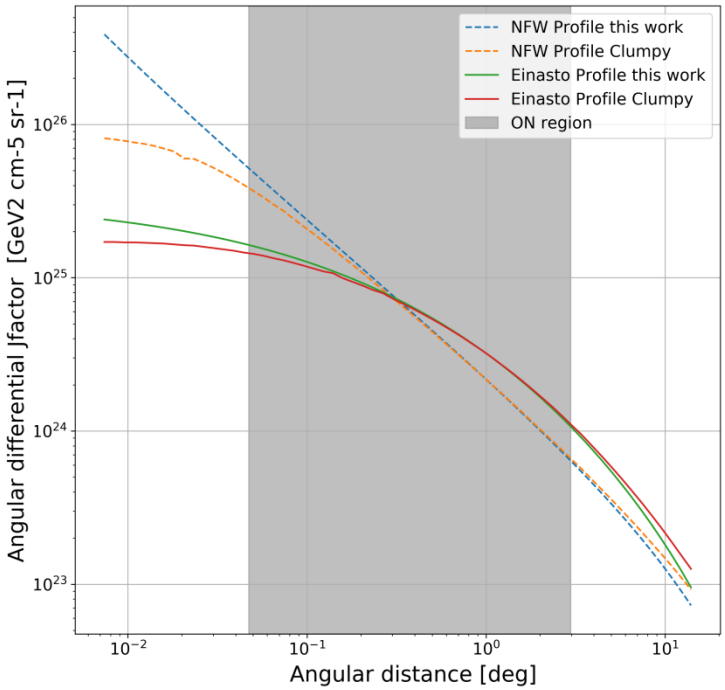

Figure 6.4: Angular differential J-Factor as a function of the angular distance to the Galactic Centre in degrees calculated in this work and obtained by CLUMPY for the NFW and the Einasto profile. The ON region shows the angular distances evaluated to obtain the sky-map of the J-Factor in the analysed field of view.

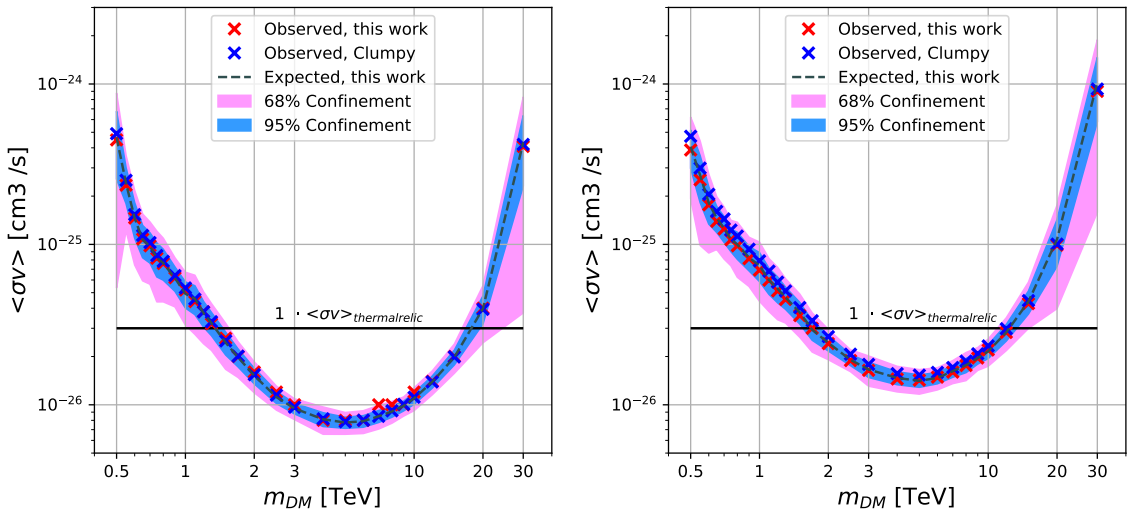

(a) (b)

Figure 6.5: Upper limits on the DM annihilation cross-section with the J-Factor computed in this work and by CLUMPY with the (a) Einasto and the (b) NFW profile.

Chapter 7

Evaluation of the Systematic Uncertainties in the DM Limits

This chapter focuses on different analysis tests in order to gain information about the systematics affecting the upper limit computation as mentioned in the previous chapter. First, an 'injection and recovery' test is performed with the Asimov data set to ensure that a DM signal would be detected if present in the data. Afterwards, certain critical regions are excluded from the region of interest like in the classical DM studies of the Galactic Centre region. The effect on the upper limit in comparison to the effects on the sensitivity are discussed. In the last part of this chapter, the analysis is performed with additional data from the HESS II and HESS IU phase to investigate the statistical behaviour of the upper limits.

7.1 Injection and Recovery Test with the Asimov Data Set

To check whether a DM signal would be detected as such and not be absorbed by any of the other model components an injection and recovery test was performed. Hereby artificial DM signals with different normalisations ($N = [0 : 100]$) are added. To minimise computational effort this was performed with an Asimov data set instead of with multiple MC simulation-based data sets. The Asimov data sets consist of the astrophysical components, the background, the diffuse emission, and the artificial DM components. The established γ-ray sources models are chosen such that the best-fit parameters are the ones obtained in Chapter 5.2. The latter is a cube filled with the predicted counts of the artificial DM signal. The test was only performed exemplary for the $b\bar{b}$ channel and the J-Factor calculated in this work with the NFW profile.
The results are plotted in Figure 7.1 and 7.2. Since the best-fit DM normalisation is equivalent to the induced one the injection and recovery test is successful. The upper limits on the DM normalisation computed from the likelihood profile of the Asimov data set fit are, as expected, above the best-fit values. Note that the upper limits for $N = 1$ and $N = 0$ are in the same order of magnitude indicating how faint a DM signal is even if $\langle \sigma v \rangle = \langle \sigma v \rangle_{\text{thermal relic}}$. To verify that the Asimov results are representable, the fitting process was repeated with 100 MC simulations. The obtained mean best-fit cross-section and the 68% and the 95% confinement bands

are shown. The Asimov best-fit parameters being within the error bands indicates that they are the median and that therefore also the upper limits are representable. As expected the upper limits are higher and the confinement bands are wider at the very low and very high DM masses. At the larger masses, this is due to lower statistics at high energies. For small masses, the DM induced γ-ray flux is lower due to the early cutoff in the spectrum resulting in larger uncertainties. For the same reason, the deviations are greater for induced DM signals with a smaller normalisation.

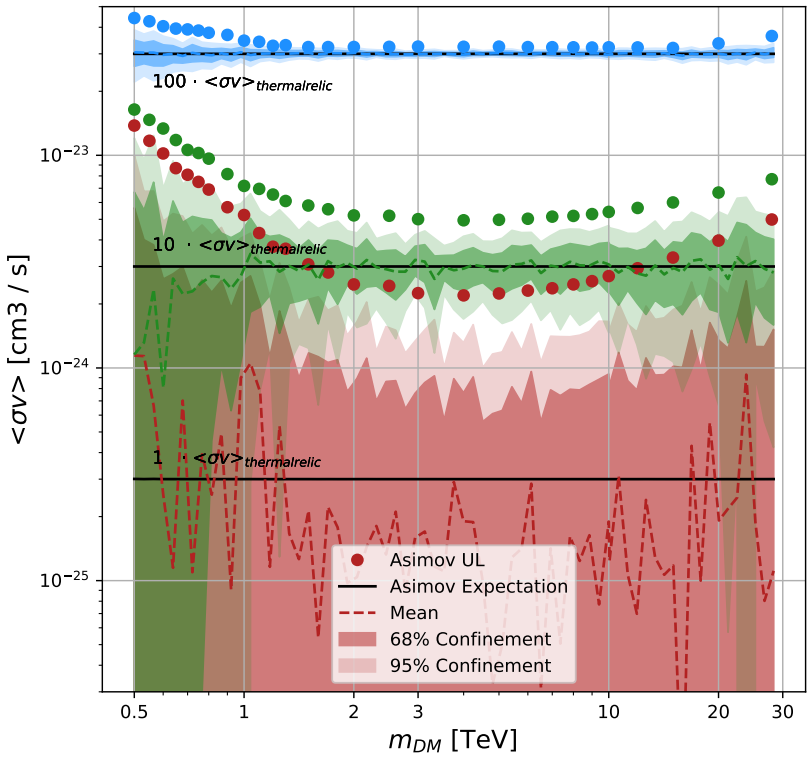

Figure 7.1: Results of the injection and recovery test. Each colour represents a injected normalisation (blue: N = 100, green: N = 10, red: N = 1). The solid black lines are the Asimov best-fit results which are equivalent to the injected signal. The dashed coloured lines correspond to the mean of all the best-fit parameters of the MC simulations. In addition, the 68% and the 95% confinement bands are shown. The dots are the upper limits on the annihilation cross-section computed from the Asimov data set likelihood profile with the other fit parameters re-optimised. The DM annihilation cross-section is shown on a logarithmic scale.

Figure 7.3 shows the different induced DM fluxes fit with the 95% upper limits on the flux obtained from the Asimov data set. The majority of the upper limits is above the artificial signal again indicating a successful recovery.

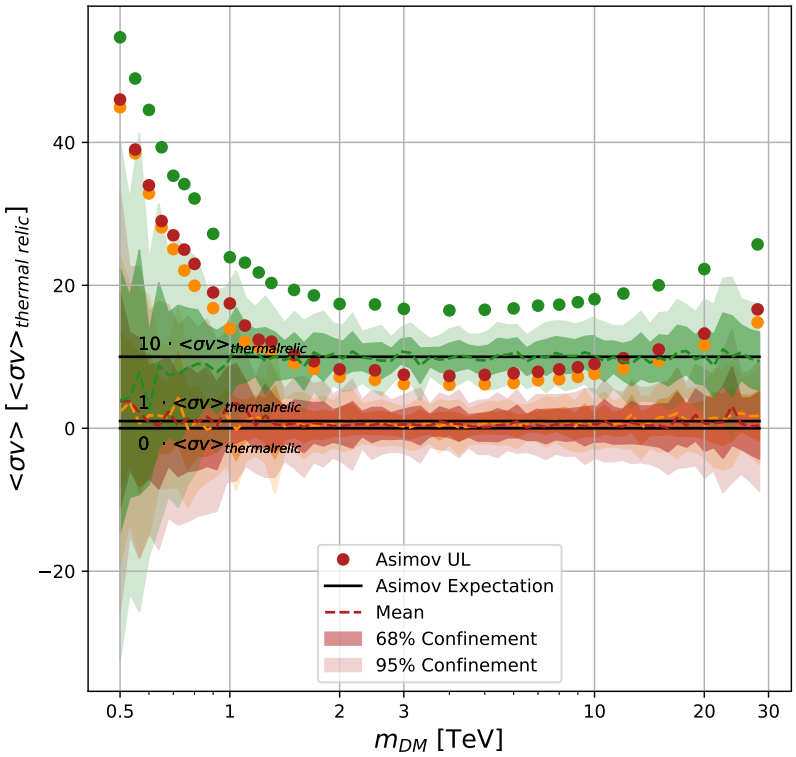

Figure 7.2: Results of the injection and recovery test. Each colour represents a injected normalisation (green: N = 10, red: N = 1 and orange: N = 0). The solid black lines, coloured dashed lines and coloured dots are the injected signal, the best-fit parameters of the MC simulations and the upper limits on the annihilation cross-section computed from the Asimov data set, respectively. The DM normalisation on a linear scale as a function of the DM mass.

It can be concluded that if there were to be a DM signal in the real data the fitting procedure would recognise it as such. However, one should consider different behaviours of the simulated Asimov data set and the real one. Possible systematic effects in the fitting of the astrophysical, the background and the diffuse emission components are not taken into account in the Asimov data set. For the same reason, the obtained upper limits from the Asimov data set are not necessarily comparable to the one from the real data.
One can conclude that the faint DM signal could be identified as such in the case of a data set free of systematic effects like the Asimov data set.

7.2 Upper Limits Obtained in a Masked Field of View

Commonly in DM constraints studies, regions in the FoV with a large γ-ray emission are excluded (i.e. in [12]). In the case of the Galactic Centre region, this is the Galactic Plane. In this work, on the other hand, the γ-ray emitting sources are modelled and included in the DM fit. This gives rise to systematic uncertainties in the fitting process. In this section, it is discussed whether these are the same uncertainties that cause the upper limits in this study to be so low. Therefore, the fitting process is repeated for masked FoVs. The most significant γ-ray source is the HESS J1745-290 positioned almost at the Galactic Centre with its spectrum being an exponential cut-off power law. Since the DM density peaks at this point, the signals may be too similar to be distinguished. This region is excluded from the FoV by the application of a mask in the form of a circle with a radius of 0.5° located at the Galactic Centre. The significance sky-map with this mask applied is shown in Figure C.3 (a). Most significant in the remaining FoV is the source G09+0.1 and the diffuse emission along the Galactic Plane. Since especially the latter is hard to model it is excluded by a rectangle mask along the Galactic Plane. The mask has a height of 1° in the complete FoV. It is shown in Figure C.3 (b). The sizes of the masks were chosen such that the excess of the sources is almost completely excluded.
In the first part of this chapter the injection and recovery test is repeated analogously to the previous section but with the two masks applied. It is investigated whether the fitting process can still recover the artificial DM signal even if a large part of the induced flux is excluded. Afterwards, the effects on the upper limits of both the Asimov data set with no induced DM signal and the real data are discussed and compared.

7.2.1 Injection and Recovery Test

In this section, an artificial DM signal with different normalisations ($N = [0 : 100]$) was added to the counts cube of the Asimov data set. Afterwards, the model components were fitted to the cube masked with either the 0.5° circle mask or the 1° band mask. The best-fit DM normalisation and the upper limit on the normalisation are compared with the ones where no mask was applied in Figure 7.4. The DM signal is always recovered. The other fitting parameters are not affected by the exclusion of

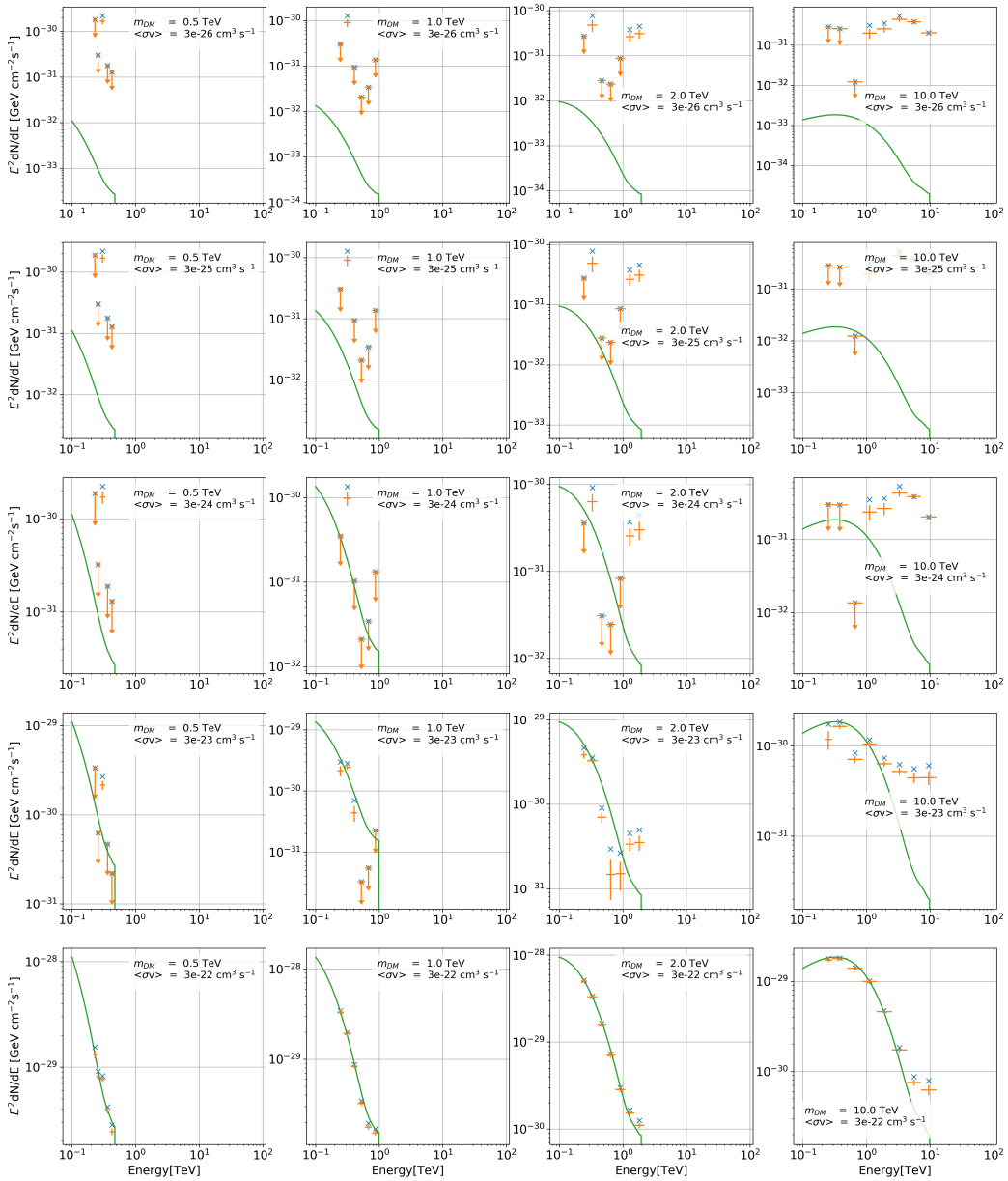

Figure 7.3: Comparison between the artificial injected DM flux and the bin wise recovered flux points. Each panel corresponds to a DM normalisation and mass.

the two regions. Both the background and the diffuse emission normalisation were recovered up to the order of 10^{-9}. As expected, the upper limits shift to greater values according to the excluded regions.

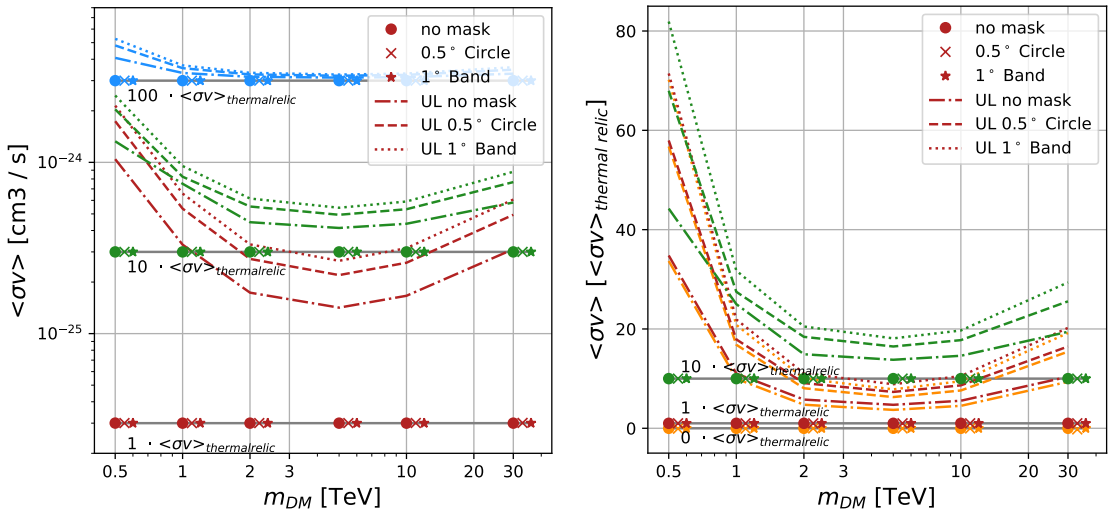

(a) (b)

Figure 7.4: Results of the injection and recovery test with masked FoVs. Each colour represents a injected normalisation (blue: N = 100, green: N = 10, red: N = 1 and orange: N = 0). The dots, crosses and stars denote the recovered best-fit DM normalisation with no mask, the 0.5° circle mask and the 1° band mask applied. Note that they all are referring to the same m_{DM} value, respectively. The dashed, dotted and dash-dotted line are the obtained upper limits with the according excluded region. (a) shows the DM annihilation cross-section on a logarithmic scale and (b) the DM normalisation on a linear scale as a function of the DM mass.

7.2.2 Real Data and Sensitivity

The constraints on the DM cross-section were computed from the HESS I data set with the two exclusion masks applied. The results are shown in Figure 7.5. Also plotted is the sensitivity (Asimov data set with $N = 0$) with no mask, the 0.5° circle mask and the 1° band mask applied. The sensitivity decreases very consistently for all masses with respect to the one computed with the complete FoV. The same behaviour is expected from the constraints on the real data (dotted lines). However, the observed upper limits do not align with the expectation. They show a different distribution and especially at small masses the deviations are in the order of one magnitude.

One can conclude that the region around the Galactic Centre and along the Galactic Plane have a very strong influence on the DM constraints. Especially the source HESS J1745-290 and the diffuse emission could account for a hypothetical DM signal and vice versa. The three-dimensional description does not seem to be adequate enough for an accurate DM constraint computation. How the single components affect the upper limits needs to be investigated in more detail. By excluding the wrongly described regions, the constraints ought to approximate the magnitude and distribution of the sensitivity. Since this is not the case but the distribution gets

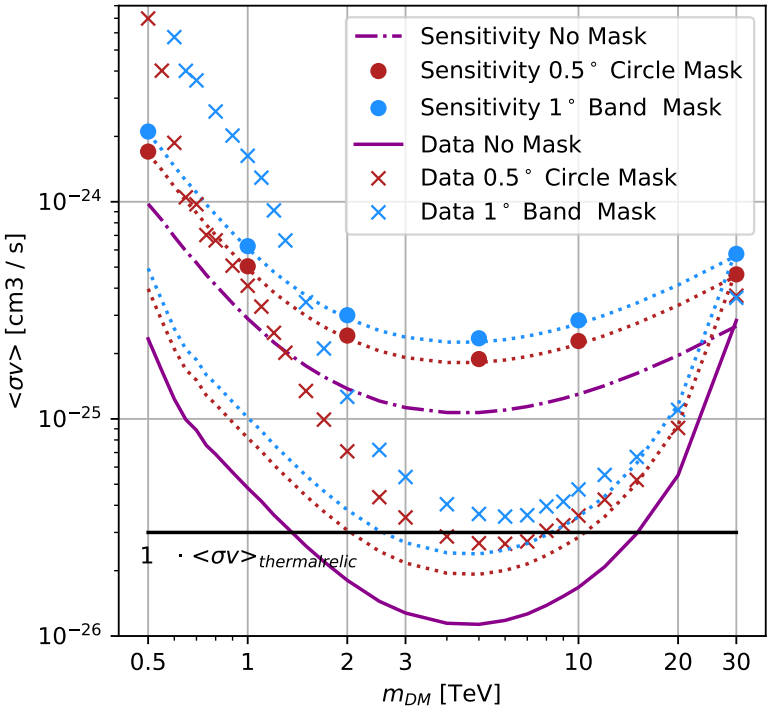

Figure 7.5: Upper limits on the DM annihilation cross - obtained from the data and the sensitivity with no mask, the 0.5° circle mask and the 1° band mask applied. The dashed lines represent the expected improvement with respect to the upper limits with no mask applied based on the improvement observed in the sensitivity.

even narrower there might be another underlying problem. Further evaluations including testing the effect of different diffuse emission and background templates are necessary.
In the following, the basic statistical behaviour of the constraints for additional data is investigated.

7.3 Analysis with Additional Data Sets

The use of more data results in better statistics and therefore a stronger constrain on the DM cross-section. If n times more data is taken into account one expects an improvement of $\sqrt{n}$. To test whether the upper limits obtained in this work show the same behaviour, the calculation was repeated with additional data sets included. They were taken during the HESS II and HESS IU phase and were discussed in Section 4.1. As shown in Chapter 5.2, the data is sufficiently described by the different model components to make a further DM analysis reasonable. The upper limit computation was performed with the HESS I and HESS II data set (HESS I+II) and all three data sets (HESS I+IU+II).
The constraints and the sensitivity are plotted for the NFW profile and the $b\bar{b}$ channel in Figure 7.6. The HESS I+II data set consists of 1.3 times more counts than the HESS I data set. The data taken in all three H.E.S.S. phases is 1.6 times larger. One therefore expects an improvement on the constraints by a factor of $\sqrt{1.3}$ ($\sqrt{1.6}$) for the HESS I+II (HESS I+IU+II) data set. The expected improved constraints are

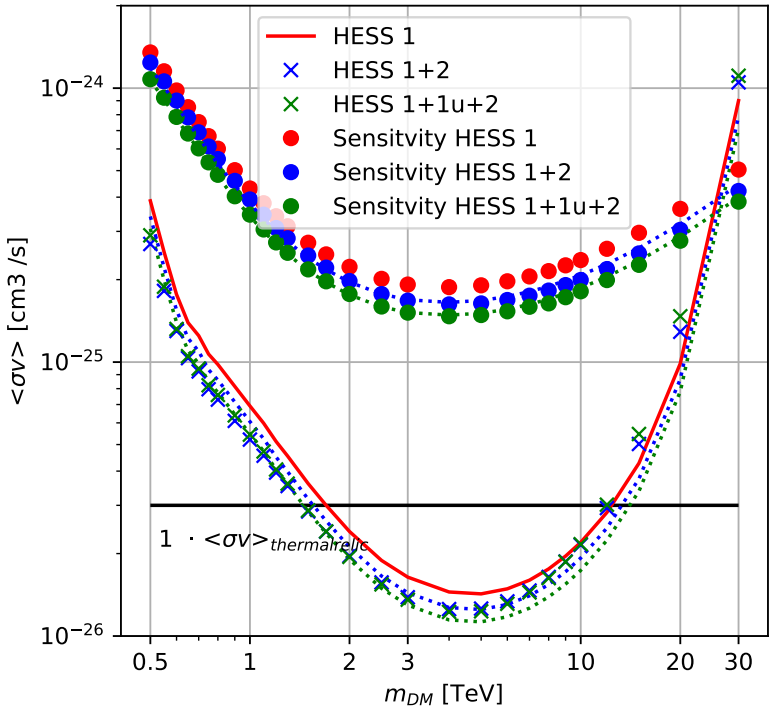

Figure 7.6: Upper limits on the DM annihilation cross-section obtained from the HESS I data only, the HESS I+II and the HESS I+IU+II data set.

plotted (dashed lines). The improved sensitivity aligns very well with the prediction. The constraints computed with the real data also improved for the majority of the masses. However, the magnitude of the improvement deviates from the expectation. The results from HESS I+II and HESS I+IU+II are not as distinguishable as for the sensitivity. Reasons for that may be an insufficient description of the HESS IU data. For very large DM masses, the upper limits increase with additional data. As already mentioned, in this energy range, the data is difficult to describe by the model components due to low statistics affecting the upper limit calculation.
The analysis with additional data has shown that the sensitivity behaves exactly as expected. The DM constraints improved, however, not for all masses by the predicted factor.

The unexpected strong constraints obtained from the data are most likely due to systematic uncertainties. This chapter tried to evaluate these uncertainties. The first step was to ensure that the fitting process can reproduce a DM signal if there were to be one present. Here this was only tested for the Asimov data set where the test was positive. However, since the systematic uncertainties only affect the analysis with the real data the next step would be an injection and recovery test of MCs of the real data.
It was assumed that the fitting of the other γ-ray emitting sources cause systematic uncertainties. A faint DM signal could be mistaken for diffuse emission, background or even the source in the Galactic Centre. This was investigated by the application of masks in the critical regions. The sensitivity shifted consistently for all masses according to available counts in the FoV. The constraints computed with the HESS I data, on the other hand, did not. The distribution changed and the magnitude of

the increased constraints was very large compared to the changes in the sensitivity. One can conclude that the γ-ray emitting sources are sufficiently described by the model for a sensitivity study. However, the sensitivity computation is not affected by the same systematic uncertainties as to the constraints. The main causes of these systematic uncertainties were not found. It is thought to be due to an insufficient description of the data for all energies. The effect of the different model components on the upper limit has to be investigated further. This would include testing of different background and diffuse emission models or the exclusion of the hard to model source HESS J1745-303.
It was tested whether the upper limits behave as statistically expected by including more data. This was the case for the sensitivity study improving the confidence in the results. The DM constraints also got improved by the additional data. However, the improvement was not as consistently in the distribution and magnitude as for the sensitivity.

There are more tests and investigations necessary for the systematic uncertainties to be understood. Otherwise, they could be included in the log-likelihood function as an additional parameter resulting in weaker constraints. This was out of the scope of this work.

Chapter 8

Dark Matter Limits for Other Annihilation Channels

For now, the upper limits were only computed for an annihilation into a $b\bar{b}$ pair. In this chapter, the results for other channels are presented. The assumed branching ratio was always 100%. The results for the $t\bar{t}$, W^+W^-, $\mu^+\mu^-$, and $\tau^+\tau^-$ are shown in Figure 8.1 for the Einasto profile based on CLUMPY. The confinement bands are computed from 100 Poisson draws of the data. The corresponding constraints and confinements bands based on CLUMPY's NFW profile are plotted in Figure D.1. For both profiles, the constraints for the leptonic channels, $\mu^+\mu^-$, and $\tau^+\tau^-$, have an unexpected distribution. Towards higher masses, the constraints are relatively large which results in the distribution to be not parabolic. The reason for this could not be determined within the scope of this work and has to be investigated further. It may be caused by errors in the upper limit computation due to a not fine enough binning of the log-likelihood profile or the annihilation spectrum. The same problems may account for the unexpected behaviour of the constraints for the W^+W^- channel within the mass-range $[3 : 10]$ TeV.

The upper limits of all annihilation channels are assumed to be affected by the systematic uncertainties. This is confirmed by a comparison with the sensitivity computed for the corresponding channels. The sensitivity is shown in Figure 8.2 (D.2) for the Einasto (NFW) profile and the $t\bar{t}$, W^+W^-, $\mu^+\mu^-$, and $\tau^+\tau^-$ channel. The DM constraints are consistently about one magnitude of order too weak and differ in their distribution from the sensitivity. However, the sensitivity based on the Einasto profile for the $t\bar{t}$ and the W^+W^- channel is comparable both in magnitude and distribution to the results published in [12] also included in Figure 8.2. The two leptonic channels differ from the expectation. The results for the $\tau^+\tau^-$ channel are within the error-bands for the smaller masses but are about one magnitude of order to strong in the higher energy range. The same behaviour is observable for the $\mu^+\mu^-$ channel expect for the deviations to be slightly larger for the smaller masses. The same distribution is observable for the NFW-based J-factor. It is probably due to the same reason causing the leptonic constraints to have a non-parabolic distribution and has to be investigated further.

One can conclude that the computed sensitivity for the different channels is in good agreement with the results from the H.E.S.S. collaboration except for the higher masses for the leptonic channels where the constaints also show an unexpected distribution. The reason for that has to be investigated in future analysis. However, the systematic uncertainties resulting in deviations between the computed constraints and the sensitivity are consistent for all annihilation channels. Therefore, the exemplary evaluation of the systematic uncertainties of the constraints with the $b\bar{b}$ channel was legitimate.

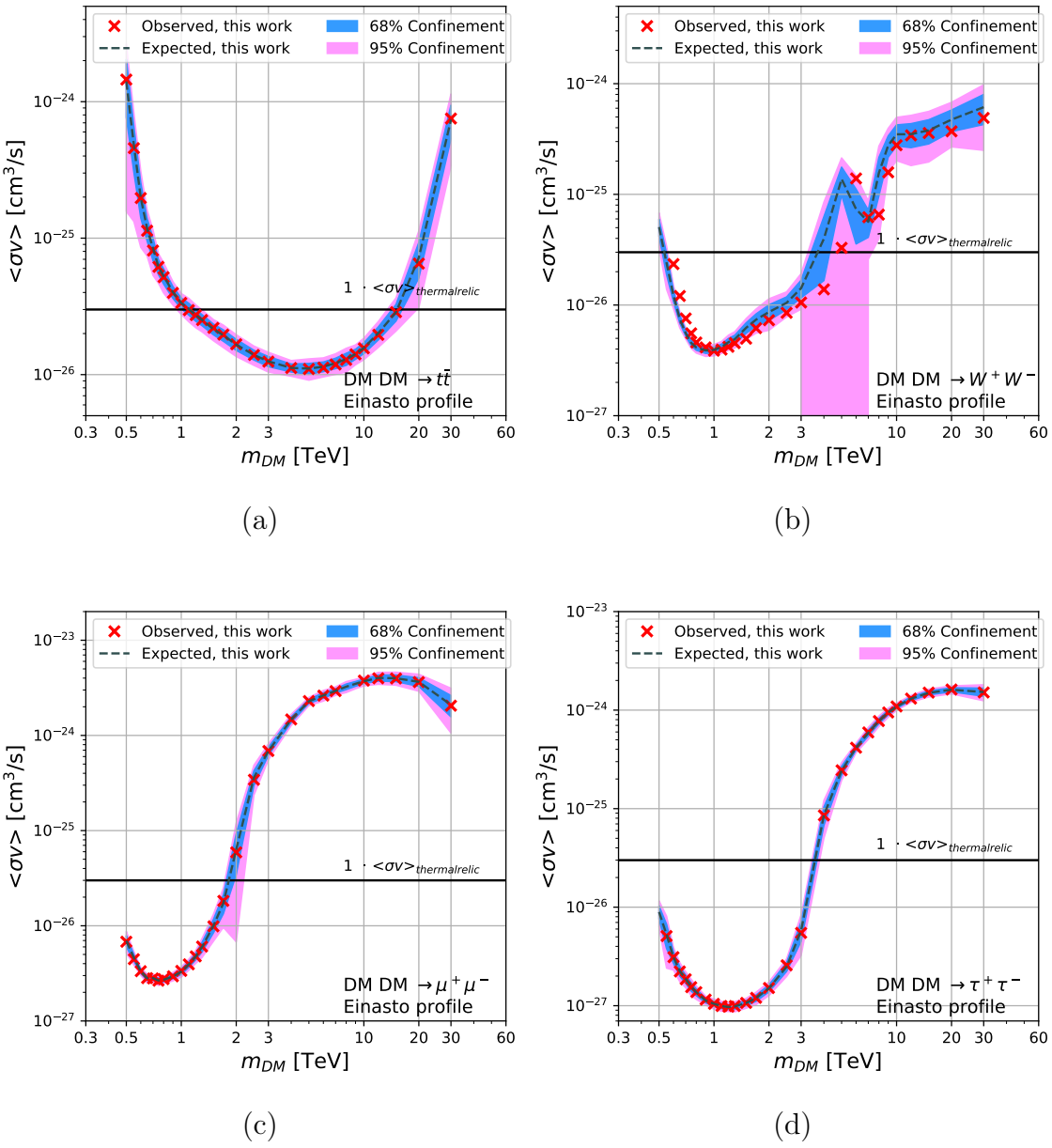

Figure 8.1: DM constraints for an annihilation into the (a) $t\bar{t}$, (b) W^+W^-, (c) $\mu^+\mu^-$, and (d) $\tau^+\tau^-$ channel computed with the Einasto profile. The 68% and the 95% confinement computed from 100 MC simulations are shown. The data of the combined data set HESS I+IU+II was used.

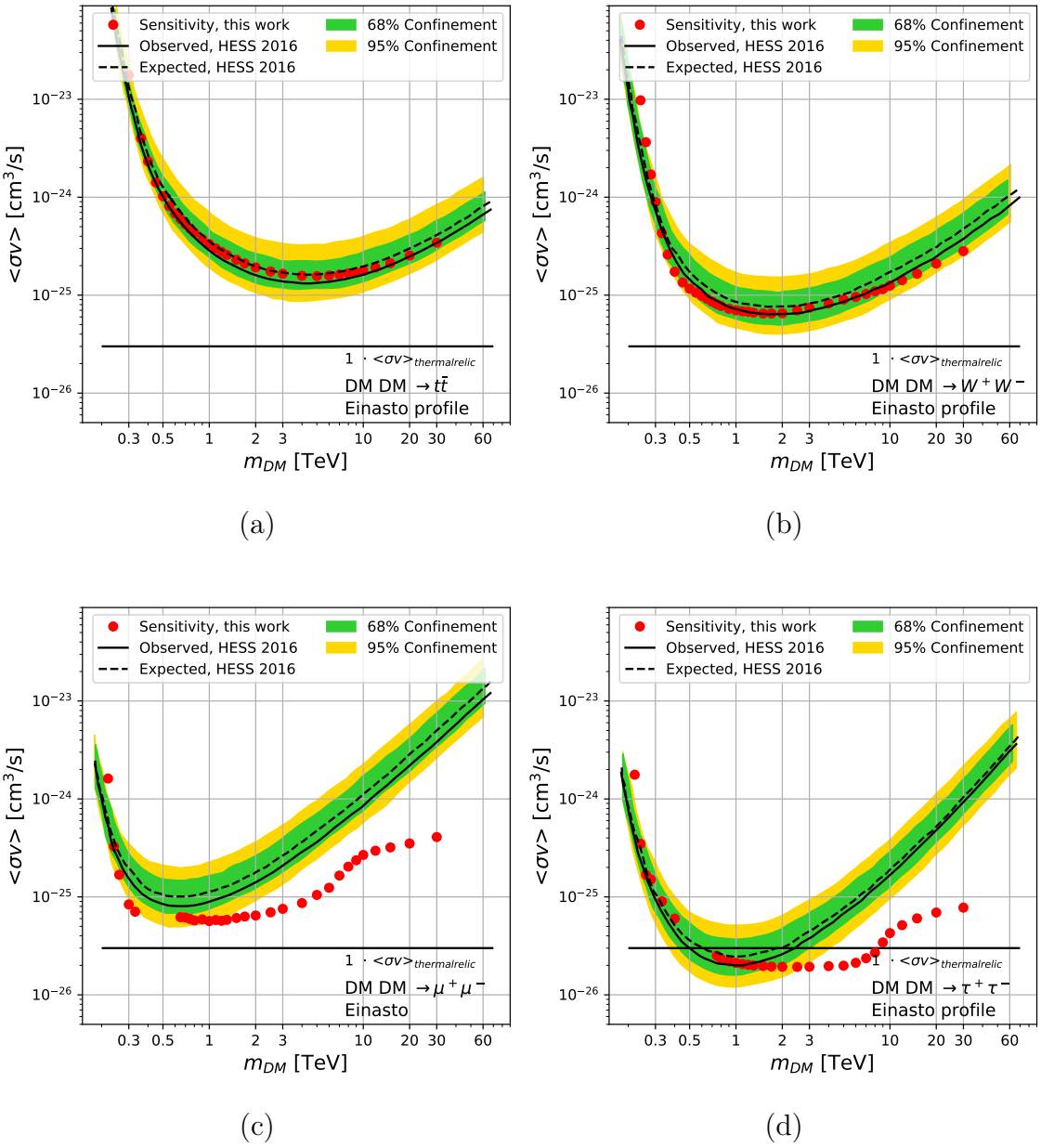

Figure 8.2: DM sensitivity of H.E.S.S. for an annihilation into the (a) $t\bar{t}$, (b) W^+W^-, (c) $\mu^+\mu^-$, and (d) $\tau^+\tau^-$ channel computed with the Einasto profile. The observed and expected results together with the 68% and the 95% confinement bands published in [12] are shown.

Chapter 9

Summary and Outlook

In this work, the DM annihilation constraints in the Galactic Centre region were computed. Instead of excluding regions that contain strong γ-ray emission, the sources were modelled and included in the three-dimensional maximum likelihood fit. Thereby, the expected DM flux is larger since the DM density peaks in the usually excluded Galactic Centre. However, this makes a good description of the region of interest crucial for the DM analysis. It was found that the developed background and diffuse emission templates in addition to the astrophysical source models meet the requirements for a sensitivity study. The results computed with an Asimov data set are in very good agreement with the published DM constraints for H.E.S.S. However, the large number of fitting parameters and complex region give rise to systematic uncertainties affecting the upper limits on the DM normalisation. This results in the constraints to be about one order of magnitude too strong. Different analysis tests were performed in an attempt to understand the origin of these systematic uncertainties. The constraints get stronger when more data is taken into account, although there are deviations from the expected shifts for some of the DM masses. Excluding the critical regions of the Galactic Centre and the Galactic Plane changed the distribution and the magnitude of the constraints. The latter was expected and also observed in the sensitivity when the masks were applied. The energy dependence of the shift of the constraints indicates an insufficient description of the data by the models at some energies.
The complex region of the Galactic Centre has to be understood and modelled more accurately, especially in the high energy range. The effect of different background and diffuse models on the upper limits has to be investigated.
Otherwise, the uncertainties have to be included in the upper limit computation. By including the uncertainty of the diffuse emission or background normalisation in the likelihood, the profile would widen resulting in larger upper limits.

One can expect a more detailed description of the Galactic Centre in the future since the interesting region is in the focus of many studies, e.g. the diffuse emission along the Galactic Plane. Hence a three-dimensional study would be improved by the new information. This may also reduce the systematic uncertainties affecting the results of this work. Since the regions where the most γ-rays due to DM annihilation are emitted do not have to be excluded, an improvement of the cross-section constraints can be expected compared to the classical approaches.

The deviations between the J-Factor computed here and the ones obtained from CLUMPY have to be investigated further. Since the effects on the upper limits are neglectable compared to the systematic uncertainties, this was not the focus of this work.

Future generations of telescopes will have improved sensitivity, energy and angular resolution in comparison to H.E.S.S., e.g. the Cherenkov Telescope Array (CTA). This will improve the upper limits on the DM annihilation cross-section and will, hopefully, result in a better understanding of the DM and the composition of the Universe.

Bibliography

[1] F. Zwicky. "Die Rotverschiebung von extragalaktischen Nebeln". In: *Helvetica Physica Acta* 6 (Jan. 1933), pp. 110–127.

[2] G. Bertone, D. Hooper, and J. Silk. "Particle dark matter: evidence, candidates and constraints". In: *Physics Reports* 405.5-6 (Jan. 2005), pp. 279–390. DOI: 10.1016/j.physrep.2004.08.031. arXiv: hep-ph/0404175 [hep-ph].

[3] K. G. Begeman, A. H. Broeils, and R. H. Sanders. "Extended rotation curves of spiral galaxies : dark haloes and modified dynamics." In: *Monthly Notices of the Royal Astronomical Society* 249 (Apr. 1991), p. 523. DOI: 10.1093/mnras/249.3.523.

[4] P. Muirhead. "Using gravitational lensing to measure stellar properties". In: *SPIE Newsroom* (Nov. 2013). DOI: 10.1117/2.1201311.005213.

[5] D. Clowe et al. "A Direct Empirical Proof of the Existence of Dark Matter". In: *The Astrophysical Journal* 648.2 (Aug. 2006), pp. L109–L113. DOI: 10.1086/508162. URL: https://doi.org/10.1086%2F508162.

[6] J. L. Feng. "Dark Matter Candidates from Particle Physics and Methods of Detection". In: *Annual Review of Astronomy and Astrophysics* 48 (Sept. 2010), pp. 495–545. DOI: 10.1146/annurev-astro-082708-101659. arXiv: 1003.0904 [astro-ph.CO].

[7] R. Scarpa. "Modified Newtonian Dynamics, an Introductory Review". In: *First Crisis in Cosmology Conference*. Ed. by Eric J. Lerner and José B. Almeida. Vol. 822. American Institute of Physics Conference Series. Mar. 2006, pp. 253–265. DOI: 10.1063/1.2189141. arXiv: astro-ph/0601478 [astro-ph].

[8] B. Famaey and S. S. McGaugh. "Modified Newtonian Dynamics (MOND): Observational Phenomenology and Relativistic Extensions". In: *Living Reviews in Relativity* 15.10 (2012). DOI: 10.12942/lrr-2012-10.

[9] I. G. Irastorza and J. Redondo. "New experimental approaches in the search for axion-like particles". In: *Progress in Particle and Nuclear Physics* 102 (Sept. 2018), pp. 89–159. DOI: 10.1016/j.ppnp.2018.05.003. arXiv: 1801.08127 [hep-ph].

[10] J. Liu, X. Chen, and X. Ji. "Current status of direct dark matter detection experiments". In: *Nature Physics* 13.3 (Mar. 2017), pp. 212–216. DOI: 10.1038/nphys4039. arXiv: 1709.00688 [astro-ph.CO].

[11] T. R. Slatyer. "TASI Lectures on Indirect Detection of Dark Matter". In: *arXiv e-prints*, arXiv:1710.05137 (Oct. 2017), arXiv:1710.05137. arXiv: 1710.05137 [hep-ph].

[12] V. Lefranc and E. Moulin. "Dark matter search in the inner galactic center halo with H.E.S.S". In: *arXiv e-prints*, arXiv:1608.08453 (Aug. 2016), arXiv:1608.08453. arXiv: 1608.08453 [astro-ph.HE].

[13] M. Cirelli et al. "PPPC 4 DM ID: a poor particle physicist cookbook for dark matter indirect detection". In: *Journal of Cosmology and Astroparticle Physics* 2011.3, 051 (Mar. 2011), p. 051. DOI: 10.1088/1475-7516/2011/03/051. arXiv: 1012.4515 [hep-ph].

[14] J. F. Navarro, C. S. Frenk, and S. D. M. White. "The Structure of Cold Dark Matter Halos". In: *The Astrophysical Journal* 462 (May 1996), p. 563. DOI: 10.1086/177173. arXiv: astro-ph/9508025 [astro-ph].

[15] D. Merritt et al. "Empirical Models for Dark Matter Halos. I. Nonparametric Construction of Density Profiles and Comparison with Parametric Models". In: *The Astrophysical Journal* 132.6 (Dec. 2006), pp. 2685–2700. DOI: 10.1086/508988. arXiv: astro-ph/0509417 [astro-ph].

[16] J. F. Navarro et al. "The diversity and similarity of simulated cold dark matter haloes". In: *Monthly Notices of the Royal Astronomical Society* 402.1 (Feb. 2010), pp. 21–34. DOI: 10.1111/j.1365-2966.2009.15878.x. arXiv: 0810.1522 [astro-ph].

[17] J. Diemand, B. Moore, and J. Stadel. "Convergence and scatter of cluster density profiles". In: *Monthly Notices of the Royal Astronomical Society* 353.2 (Sept. 2004), pp. 624–632. DOI: 10.1111/j.1365-2966.2004.08094.x. arXiv: astro-ph/0402267 [astro-ph].

[18] P. D. Sackett and L. S. Sparke. "The Dark Halo of the Polar-Ring Galaxy NGC 4650A". In: *The Astrophysical Journal* 361 (Oct. 1990), p. 408. DOI: 10.1086/169206.

[19] A. Burkert. "The Structure of Dark Matter Halos in Dwarf Galaxies". In: *The Astrophysical Journal Letters* 447 (July 1995), pp. L25–L28. DOI: 10.1086/309560. arXiv: astro-ph/9504041 [astro-ph].

[20] W. Heitler. *The quantum theory of radiation*. Vol. 5. International Series of Monographs on Physics. Oxford: Oxford University Press, 1936.

[21] J. Matthews. "A Heitler model of extensive air showers". In: *Astroparticle Physics* 22.5-6 (Jan. 2005), pp. 387–397. DOI: 10.1016/j.astropartphys.2004.09.003.

[22] M. Barrantes et al. "Atmospheric corrections of the cosmic ray fluxes detected by the Solar Neutron Telescope at the Summit of the Sierra Negra Volcano in Mexico". In: *Geofísica Internacional* 57 (Oct. 2018), pp. 253–275.

[23] J. Hinton and W. Hofmann. "Teraelectronvolt Astronomy". In: *Annual Review of Astronomy and Astrophysics* 47 (June 2010). DOI: 10.1146/annurev-astro-082708-101816.

[24] *H.E.S.S. collaboration H.E.S.S. High Energy Stereoscopic System*. https://www.mpi-hd.mpg.de/hfm/HESS/. Accessed: 2020-08-15.

[25] F. Aharonian et al. "Observations of the Crab nebula with HESS". In: *Astronomy & Astrophysics* 457.3 (Oct. 2006), pp. 899–915. DOI: 10.1051/0004-6361:20065351. arXiv: astro-ph/0607333 [astro-ph].

[26] S. Heinz. "A Detailed Study of the Supernova Remnant RCW 86 in TeV -Ray". https://ecap.nat.fau.de/wp-content/uploads/2017/05/2012_Heinz_Dissertation.pdf. PhD thesis. Friedrich-Alexander-Universität Erlangen-Nürnberg, 2012.

[27] S. Ohm, C. van Eldik, and K. Egberts. "Gamma-hadron separation in very-high-energy -ray astronomy using a multivariate analysis method". In: *Astroparticle Physics* 31.5 (June 2009), pp. 383–391. ISSN: 0927-6505. DOI: 10.1016/j.astropartphys.2009.04.001. URL: http://dx.doi.org/10.1016/j.astropartphys.2009.04.001.

[28] D. Berge, S. Funk, and J. Hinton. "Background modelling in very-high-energy γ-ray astronomy". In: *Astronomy & Astrophysics* 466.3 (May 2007), pp. 1219–1229. DOI: 10.1051/0004-6361:20066674. arXiv: astro-ph/0610959 [astro-ph].

[29] C. Deil et al. "Gammapy - A prototype for the CTA science tools". In: *35th International Cosmic Ray Conference (ICRC2017)*. Vol. 301. International Cosmic Ray Conference. Jan. 2017, p. 766. arXiv: 1709.01751 [astro-ph.IM].

[30] L. Mohrmann et al. "Validation of open-source science tools and background model construction in γ-ray astronomy". In: *Astronomy & Astrophysics* 632, A72 (Dec. 2019), A72. DOI: 10.1051/0004-6361/201936452. arXiv: 1910.08088 [astro-ph.IM].

[31] G. Cowan et al. "Asymptotic formulae for likelihood-based tests of new physics". In: *European Physical Journal C* 71, 1554 (Feb. 2011), p. 1554. DOI: 10.1140/epjc/s10052-011-1554-0. arXiv: 1007.1727 [physics.data-an].

[32] A. Wald. "Tests of Statistical Hypotheses Concerning Several Parameters When the Number of Observations is Large". In: *Transactions of the American Mathematical Society* 54 (Nov. 1943), pp. 426–482.

[33] H. E. S. S. Collaboration, H. Abdalla, et al. "Characterising the VHE diffuse emission in the central 200 parsecs of our Galaxy with H.E.S.S." In: *Astronomy & Astrophysics* 612, A9 (Apr. 2018), A9. DOI: 10.1051/0004-6361/201730824. arXiv: 1706.04535 [astro-ph.HE].

[34] *H.E.S.S. collaboration 11 years later: Discovery of a Cosmic PeVatron in the Galactic Center*. https://www.mpi-hd.mpg.de/hfm/HESS/pages/home/som/2016/04/. Accessed: 2020-08-20.

[35] Y. W. Wong. personal communication. 2020.

[36] T. -P. Li and Y. -Q. Ma. "Analysis methods for results in gamma-ray astronomy." In: *The Astrophysical Journal* 272 (Sept. 1983), pp. 317–324. DOI: 10.1086/161295.

[37] M. Hütten, C. Combet, and D. Maurin. "CLUMPY v3: γ-ray and ν signals from dark matter at all scales". In: *Computer Physics Communications* 235 (Feb. 2019), pp. 336–345. DOI: 10.1016/j.cpc.2018.10.001. arXiv: 1806.08639 [astro-ph.CO].

[38] A. Charbonnier, C. Combet, and D. Maurin. "CLUMPY: A code for γ-ray signals from dark matter structures". In: *Computer Physics Communications* 183.3 (Mar. 2012), pp. 656–668. DOI: 10.1016/j.cpc.2011.10.017. arXiv: 1201.4728 [astro-ph.HE].

[39] V. Bonnivard et al. “CLUMPY: Jeans analysis, γ-ray and ν fluxes from dark matter (sub-)structures”. In: *Computer Physics Communications* 200 (Mar. 2016), pp. 336–349. DOI: 10.1016/j.cpc.2015.11.012. arXiv: 1506.07628 [astro-ph.CO].

Appendix A

Exposure Maps

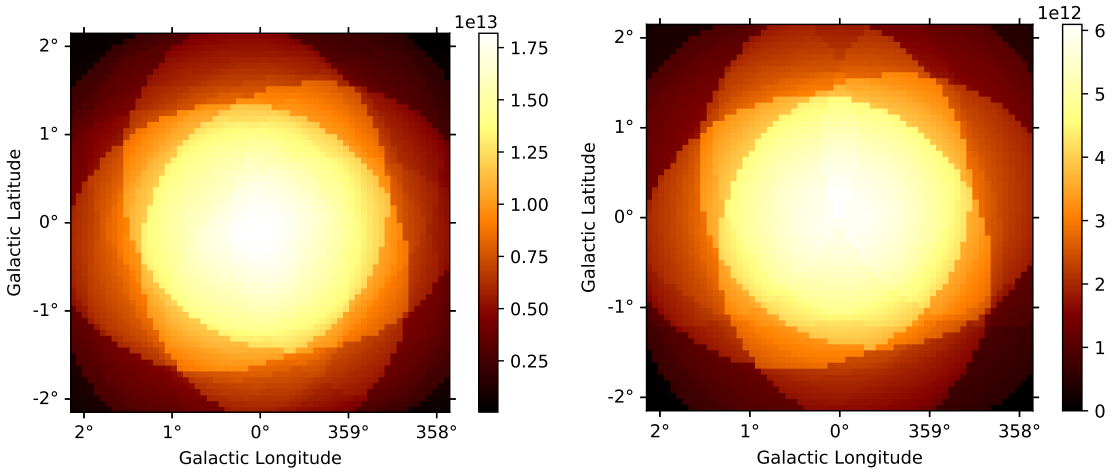

(a) (b)

Figure A.1: Exposure map of the Galactic Centre region in the (a) HESS I and the (b) HESS IU phase

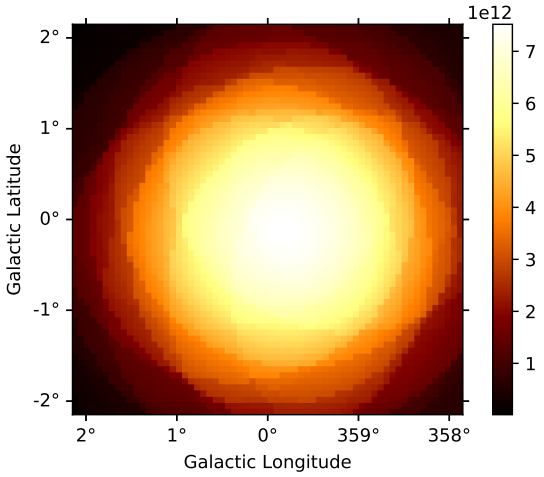

Figure A.2: Exposure map of the Galactic Centre region in the HESS II phase

Appendix B

Fit Results of the Galactic Centre Region

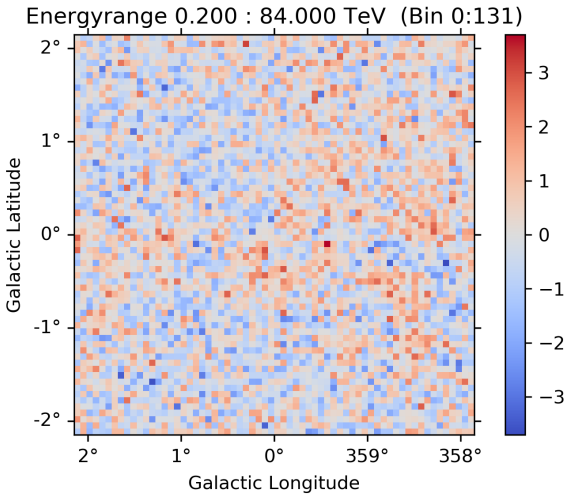

Figure B.1: Unsmoothed significance of the residual of the Galactic Centre fit based on 5.2.2 (HESS I data).

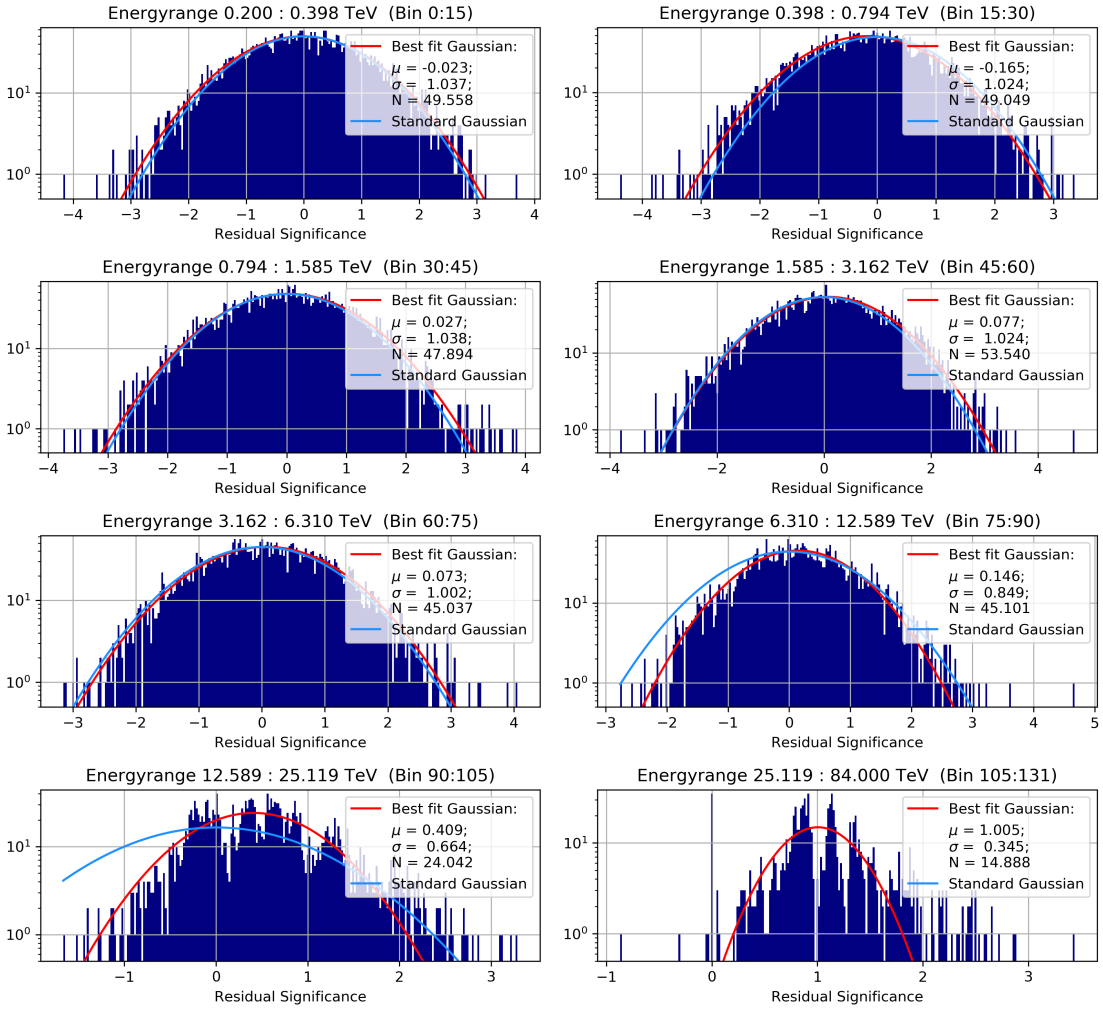

Figure B.2: Distribution of the unsmoothed significance for different energies (HESS I data).

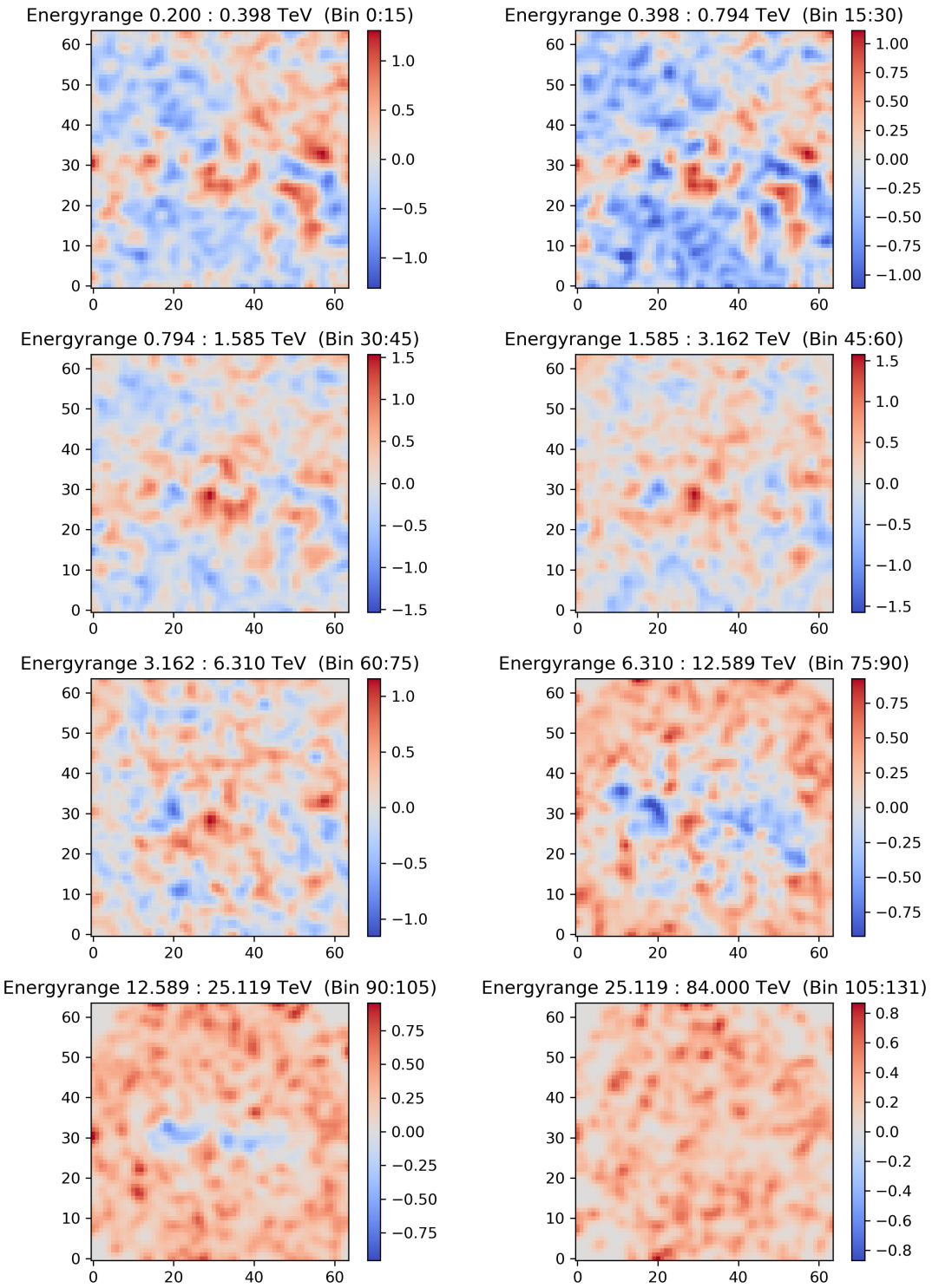

Figure B.3: Gaussian smoothed significance of the residuals for different energies (HESS I data).

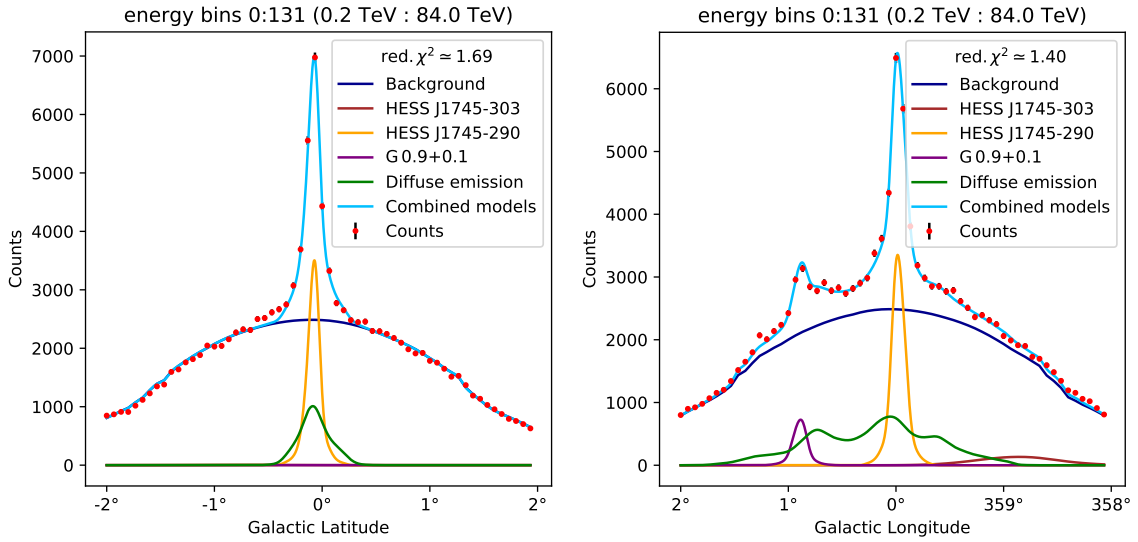

(a) (b)

Figure B.4: Profiles of the combined HESS I+II data and model sky-map with its single components along (a) the Galactic Longitude and (b) the Galactic Latitude within a 4° x 0.5° box and a 0.5° x 4° box, respectively. The observed and expected counts are summed up over all energies.

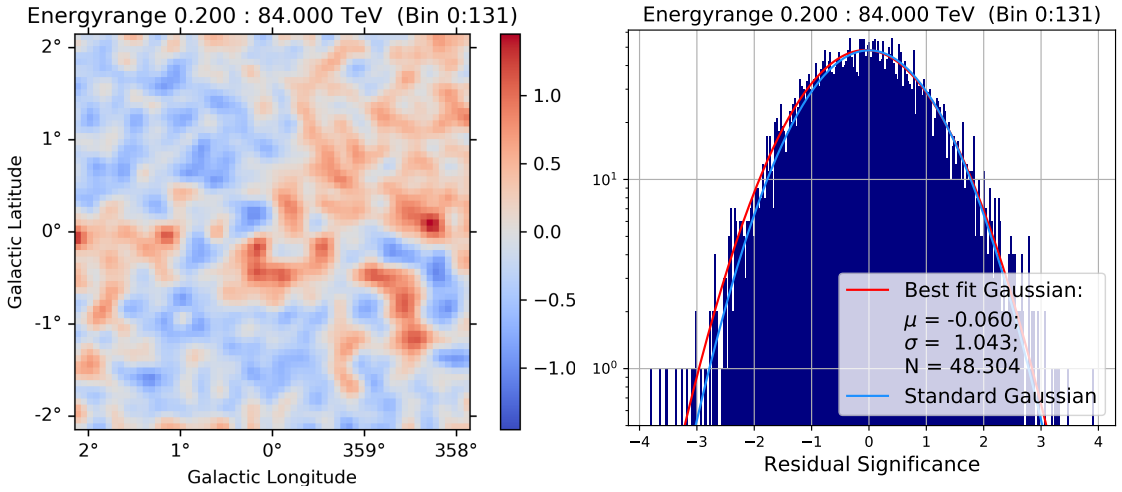

(a) (b)

Figure B.5: (a) Significance of the residual of the combined data HESS I+II smoothed with a two-dimensional Gaussian with width 0.08° (b) Distribution of the unsmoothed significance of the residual. A one-dimensional Gaussian was fitted to the data, with its best-fit parameters being in the legend, together with the Standard Gaussian (HESS I+II data)

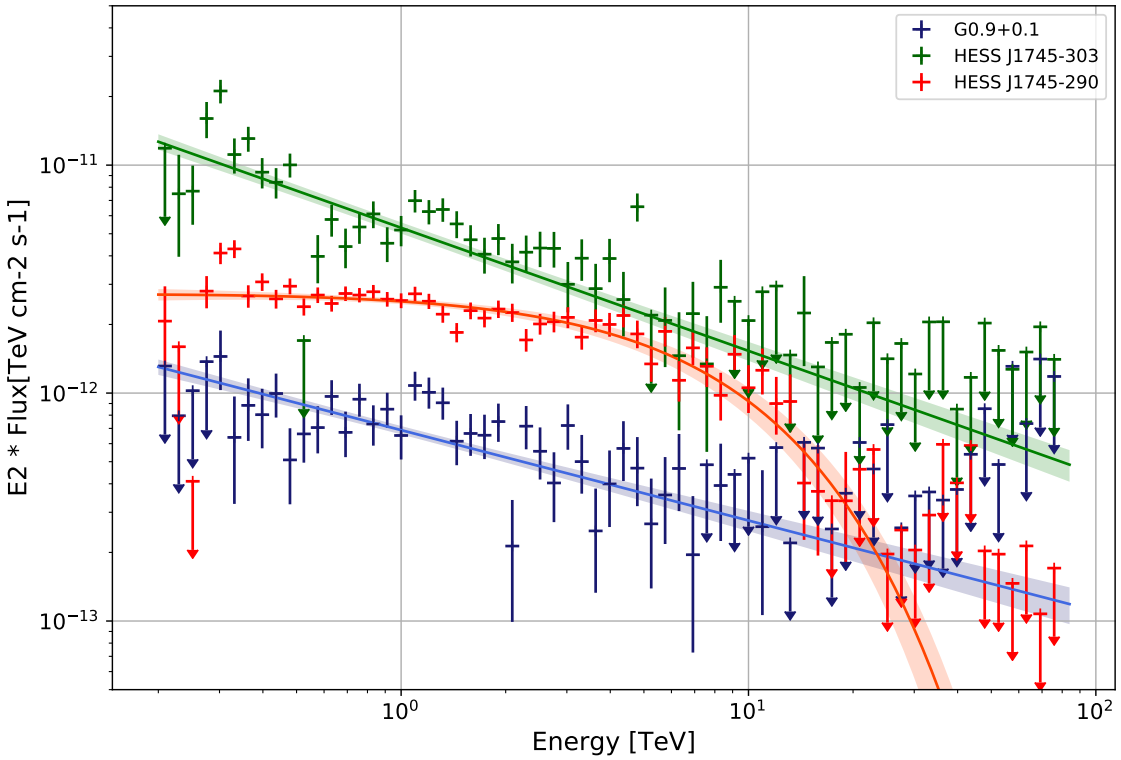

Figure B.6: $E^2 \cdot \gamma$-ray flux of the three astrophysical sources, G09+0.1, HESS J1745-290, and HESS J1747-281. Spectrum plotted with the best-fit parameters and error bands and flux-points (HESS I+II data)

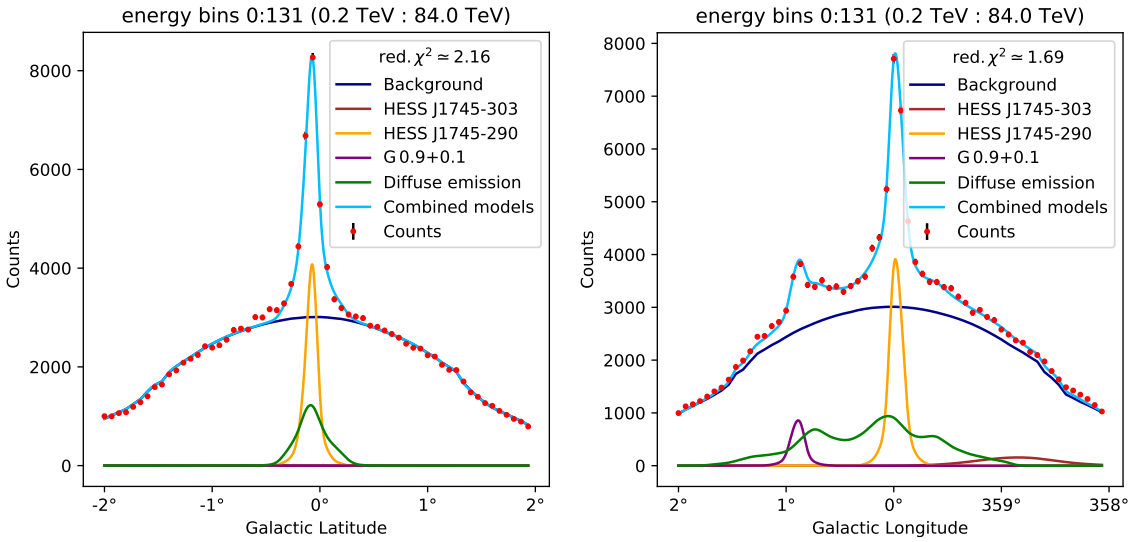

(a) (b)

Figure B.7: Profiles of the combined HESS I+IU+II data and model sky-map with its single components along (a) the Galactic Longitude and (b) the Galactic Latitude within a 4° x 0.5° box and a 0.5° x 4° box, respectively. The observed and expected counts are summed up over all energies.

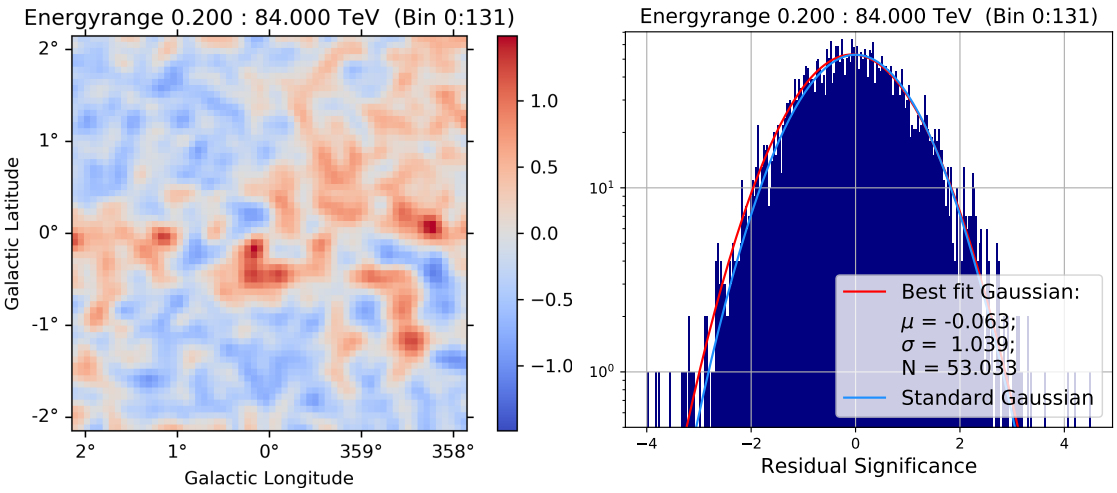

(a) (b)

Figure B.8: (a) Significance of the residual of the combined data HESS I+IU+II smoothed with a two-dimensional Gaussian with width 0.08° (b) Distribution of the unsmoothed significance of the residual. A one-dimensional Gaussian was fitted to the data, with its best-fit parameters being in the legend, together with the Standard Gaussian (HESS I+IU+II data)

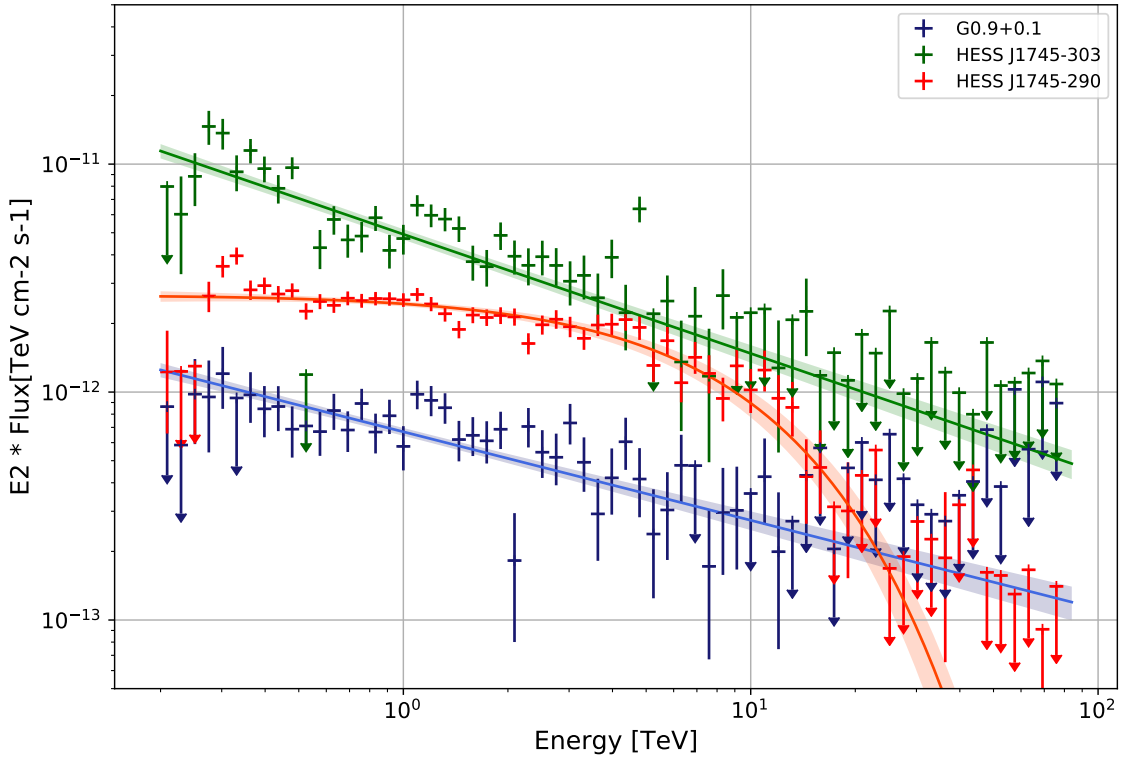

Figure B.9: $E^2 \cdot \gamma$-ray flux of the three astrophysical sources, G09+0.1, HESS J1745-290, and HESS J1747-281. Spectrum plotted with the best-fit parameters and error bands and flux-points (HESS I+IU+II data)

this work (HESS I+II) **this work (HESS I+IU+II)** **(reference)**	**J1745-290**	**G09+0.1**	**J1745-303**
Flux norm ϕ_0 **[**10^{12}/**TeV cm**^{2} **s**]	2.694 ±0.058 2.73 ±0.0615 (2.55 ±0.04)	0.657 ±0.03 0.669 ±0.03 (0.88 ±0.04)	5.373 ±0.299 4.923 ±0.262 (2.84 ±0.23)
Spectral index Γ	2.01 ±0.03 1.99 ±0.03 (2.14 ±0.02)	2.374 ±0.04 2.388 ±0.04 (2.40 ±0.11)	2.502 ±0.032 2.523 ±0.031 (2.71 ±0.11)
$\mathbf{E_{Cutoff}}$ **[TeV]**	9.67 ±0.93 8.78 ±0.86 (10.7 ±2.0)		
Longitude l **[**°**]**	359.95 ±0.001 359.95 ±0.01 (359.94)	0.86 ±0.003 0.87 ±0.002 (0.86)	358.711 ±0.0160 358.692 ±0.0197 (358.71)
Latitude b **[**°**]**	-0.06 ±0.001 -0.06 ±0.01 (- 0.05)	0.08 ±0.003 0.08 ±0.003 (0.07)	-0.593 ±0.021 -0.611 ±0.017 (-0.64)

Table B.1: Best-fit parameters for the three astrophysical sources obtained from the combined HESS I+II and HESS I+IU+II data. Reference values taken from [33].

Appendix C

CLUMPY J-Factor Sky-maps

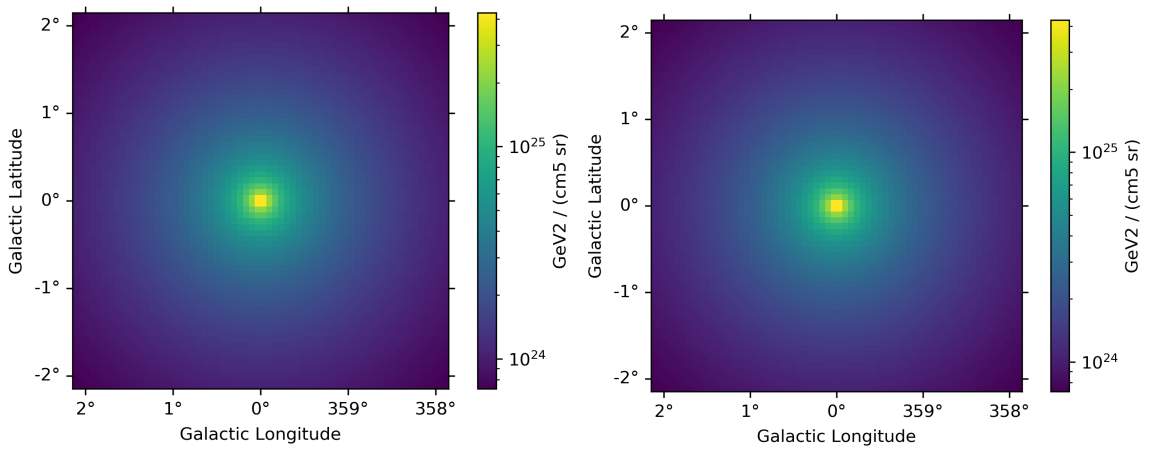

(a) (b)

Figure C.1: CLUMPY differential J-Factor maps (a) for the Einasto and (b) for the NFW profile

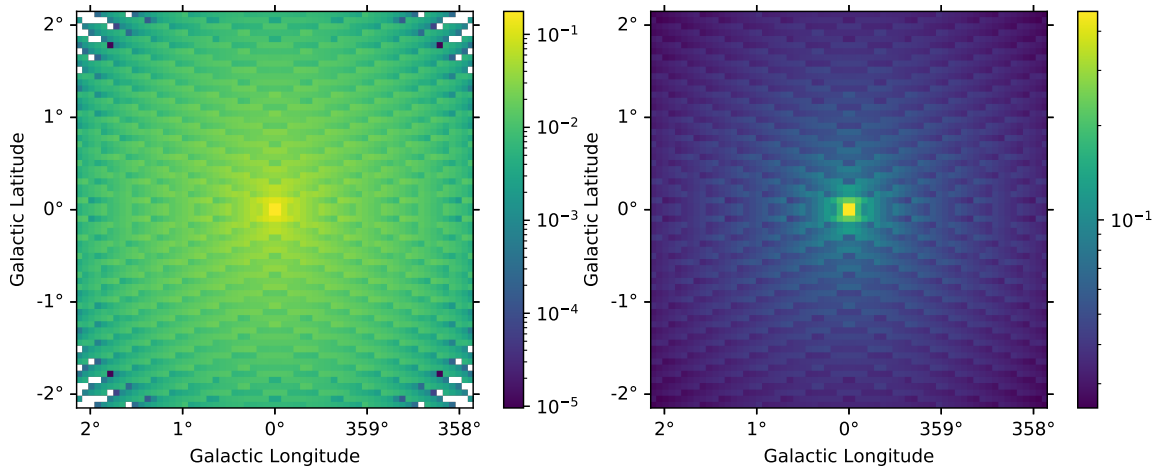

(a) (b)

Figure C.2: Relative error of the Clumpy differential J-Factor maps and the maps calculated in this work (a) for the Einasto and (b) for the NFW profile

Density profile	**kEINASTO**	**kZHAO**
Shape parameter	0.17	(1,3,1)
scale radius [kpc]	20	21
Outer bound [kpc]	260	260
Sun's distance [kpc]	8.5	8.5
$\rho_\odot$ **[GeV/cm^3]**	0.39	0.39

Table C.1: CLUMPY parameters used to compute the J-Factor sky-maps

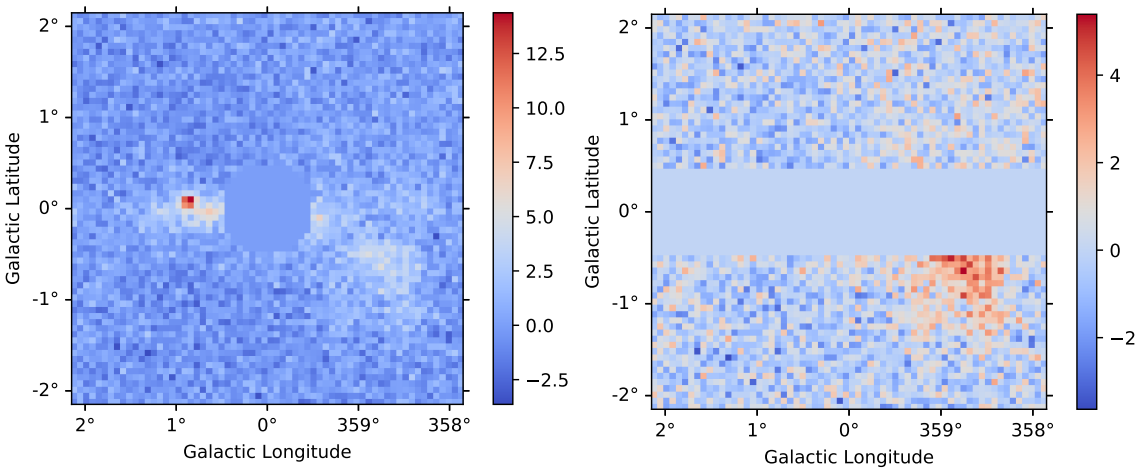

(a) (b)

Figure C.3: Li & Ma significance of the HESS I data with masks applied: (a) 0.5° circle with the Galactic Centre at the centre and (b) 1° band along the Galactic Plane.

Appendix D

Dark Matter Limits for Other Annihilation Channels

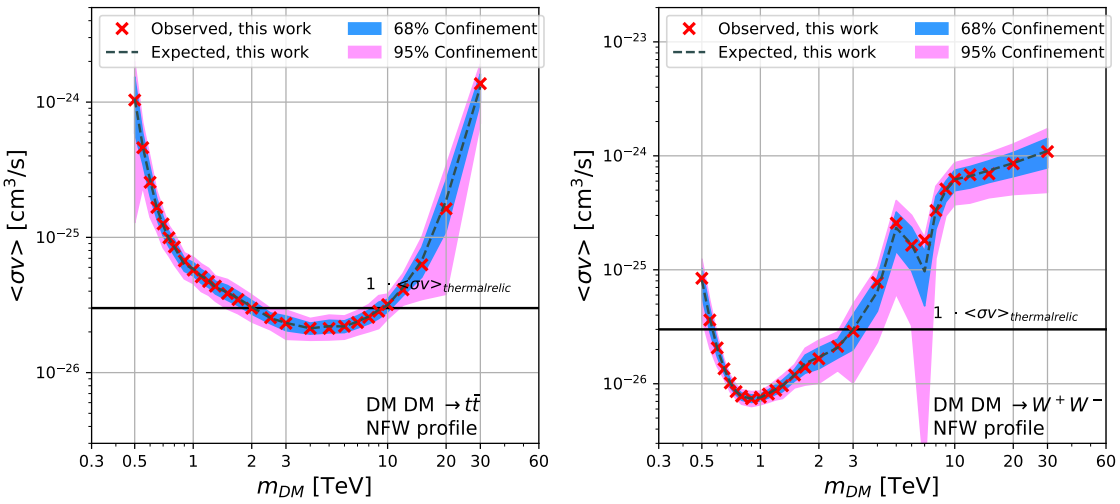

(a)

(b)

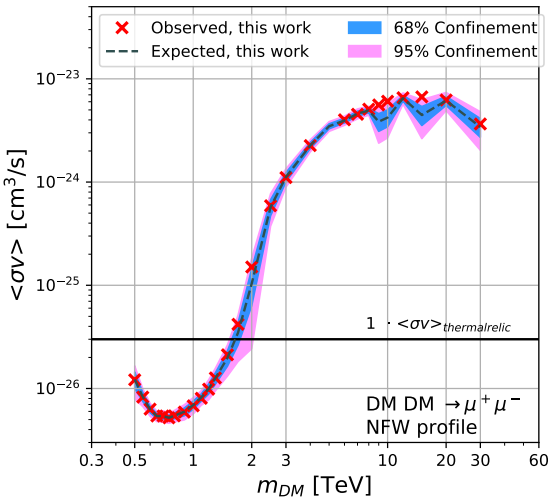

(c)

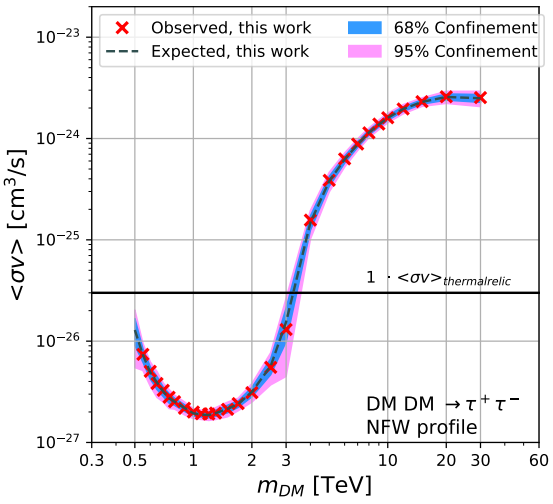

(d)

Figure D.1: DM constraints for an annihilation into the (a) $t\bar{t}$, (b) W^+W^-, (c) $\mu^+\mu^-$, and (d) $\tau^+\tau^-$ channel computed with the NFW profile. The confinement bands are computed from 100 MC simulations.

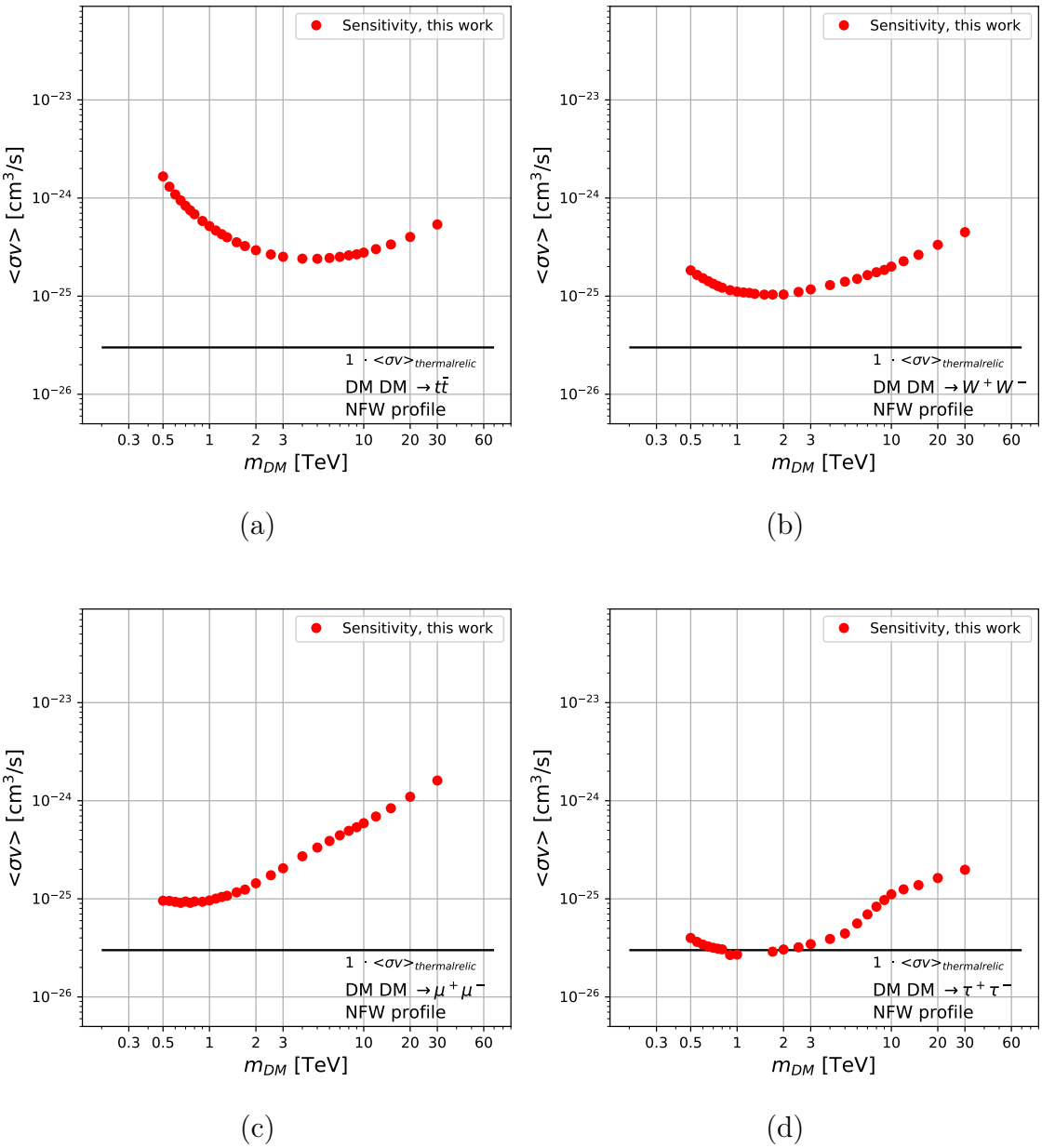

Figure D.2: DM sensitivity for an annihilation into the (a) $t\bar{t}$, (b) W^+W^-, (c) $\mu^+\mu^-$, and (d) $\tau^+\tau^-$ channel computed with the NFW profile.

Acknowledgements

I want to thank Christopher van Eldik for the opportunity to work on this subject I was really interested in, his helpfulness, the proofreading, and for always having time for a discussion when I got stuck.

Thanks to the whole Gamma-ray group for the nice and friendly work environment. The weekly meetings of the 3D analysis group always gave me great input which helped and motivated me a lot. Especially, Wun, thanks for always helping me with any problems I had and for reading my draft.

I want to thank my family for supporting me for as long as I can remember.
To my sisters by choice, the mystery-solving group, Walter, and the rest of my friends, thanks for all the fun and for always being there for me!

Erklärung

Ich erkläre hiermit an Eides statt, dass ich die vorliegende Arbeit selbständig verfasst und dabei keine anderen als die angegebenen Hilfsmittel benutzt habe. Sämtliche Stellen der Arbeit, die im Wortlaut oder dem Sinn nach Publikationen oder Vorträgen anderer Autoren entnommen sind, habe ich als solche kenntlich gemacht.

Erlangen, den 20.10.2020